

Driven Magnetic Flux Lines in Type-II Superconductors: Nonequilibrium Steady States and Relaxation Properties

Thananart Klongcheongsan

Dissertation submitted to the Faculty of the
Virginia Polytechnic Institute and State University
in partial fulfillment of the requirements for the degree of

Doctor of Philosophy
in
Physics

Uwe C. Täuber, Chair
Giti A. Khodaparast
Rahul V. Kulkarni
Kyungwha Park

March 31, 2009
Blacksburg, Virginia

Keywords: Type-II Superconductors, Nonequilibrium Steady States, Aging Dynamics
Copyright 2009, Thananart Klongcheongsan

Driven Magnetic Flux Lines in Type-II Superconductors: Nonequilibrium Steady States and Relaxation Properties

Thananart Klongcheongsan

(ABSTRACT)

We investigate the nonequilibrium steady state of driven magnetic flux lines in type-II superconductors subject to strong point or columnar pinning centers and the aging dynamics of nonequilibrium relaxation process in the presence of weak point pinning centers. We employ a three-dimensional elastic line model and Metropolis Monte Carlo simulations. For the first part, we characterize the system by means of the force-velocity / current-voltage curve, static structure factor, mean vortex radius of gyration, number of double-kink and half-loop excitations, and velocity / voltage noise features. We compare the results for the above quantities for randomly distributed point and columnar defects. Most of both numerical works have been done in two-dimensional systems such as thin film in which the structure of flux lines is treated as a point-like particle. Our main point of investigation in this paper is to demonstrate that the vortex structure and its other transport properties may exhibit a remarkable variety of complex phenomena in three-dimensional or bulk superconductors. The second part devotes to the study of aging phenomena in the absence of a driving force in disordered superconductors with much weaker point disorder. By investigating the density autocorrelation function, we observe all three crucial properties of the aging phenomena; slow power-law relaxation, breaking of time-translation invariance, and the presence of the dynamical scaling. We measure the dynamical exponents b and λ_c/z and compare to other work. We find exponent values increase for increasing pinning strength, smaller interaction range, lower temperature, and denser defect density while the exponents measured in other approach tend to decrease.

Acknowledgments

I first would like to thank my advisor, Prof. Uwe Täuber. Without his encouragement over the past four years, especially during my first year, this work could have never been accomplished. My scientific abilities, precision, perspective in life, English language skills, and other talents have been gradually refined due to his patience and care. It still sticks deeply in my mind that he noticed it took me two years to stop calling him ‘Sir’ after I graduated from VMI. During periods when my work progressed slower than expected, he always maintained a positive attitude while motivating me to finish the job. At the time of this writing, I am still learning from him and hopes that I can use as many of his valuable lessons as possible for both my work and life when I leave this place. Again, I really appreciate all you have done for me.

I would also like to thank my committee for the knowledge you passed onto me during the first few years. I will always remember the smiles on the faces of Prof. Khodoparast and Kulkarni whenever we meet. Thank you Prof. Park for teaching me how to conduct simulations during her course.

Special thanks to Prof. Michel Pliemling for his advice and useful discussions we had about aging dynamics. I would have really wanted to do more work with you if I had been here longer.

Thank you to all of my professors who provided me with the knowledge of physics during my first two years. In particular, I would like to thank Prof. Mizutani for your help, generosity, and the chance you gave me. Your help allowed me to barely complete my graduate course work and earn my M.S.

Sincere thanks to Chris Thomas for her administrative support to me and everyone else in the department. Her advice always made my life easier during the time I was here.

Many thanks for Jayajit Das, Thomas Bullard, and George Daquila for your help and discussions during the beginning of my work. Special thanks go to George for his expertise and tips on the Linux machine. He is one of the people I respect the most around here.

I would also like to thank Sayak Mukherjee, Sven Dorosz, and the crew in Robeson 104 for the joy and friendship you gave me. Thank you for teaching me physics during the time of my research. Sayak’s friendship is too rare and genuine to ever forget. Without him during the first two years, I would have never been able to enter the Ph.D. program. I would like to thank you a billion times. Hope you and Sven become good research partners in the near future.

All members of the Thai Student Association during the time I have been here deserve my appreciation. All the fun and events we had together made this place my home away from home. Glad to see baby Don as our new member during the time I was writing my thesis. Hope you all learn as much as you can, and as our government expects. Our country needs students like us for a brighter future.

I would like to thank LTC Deniela and Gregory Topasna, Col. Stacia Vargas, and Mr. David Allen at the Virginia Military Institute for the support and recommendations they provided me so that I could come to Virginia Tech. Each of my '04 brother rats, especially Echo company, deserve a big hug. Chen, Ropp, Hamilton, Glasnovich, Dennis, and Lincoln, thank you for introducing me to the interesting American culture as well as those of other countries.

I must not forget to thank the Royal Thai Army for its financial support during my four years at VMI. I truly believe that I have learnt what the Army expected. I will dedicate my life and apply all the knowledge I have learnt from here in order to develop a better and stronger Army.

Finally, I would like to thank my family members. All they have done for me cannot be described here since it would be more than the thesis itself. Hope all I have done has made you proud, and has made you the happiest mom and dad on earth.

To all others who helped me along the way, thank you. I will never forget those who helped me along the journey.

Thank you.

Contents

1	Introduction	1
1.1	History of Superconductivity	1
1.2	Applications of HTS Materials	4
1.3	Theoretical and Experimental Survey	4
1.4	Objective and Motivation of Study	6
2	Theoretical Approach	7
2.1	Superconducting Phenomena	7
2.2	London Theory	9
2.3	Ginzburg-Landau Theory	11
2.4	Disorder and Flux Pinning	13
2.5	Equilibrium States	14
2.6	Non-equilibrium Steady States	16
2.7	Non-equilibrium Relaxation: Aging Dynamics	18
2.8	Stochastic Model	21
3	Numerical Method/ Algorithm	24
3.1	The Model	24
3.2	Quantities of Interest	27
3.2.1	Characterization of Non-Equilibrium Steady States	27
3.2.2	Aging Dynamics	30
4	Characterization of Nonequilibrium Steady States	32
4.1	Current-Voltage (I-V) Characteristics	34
4.2	Radius of Gyration	41

4.2.1	Columnar Defects	41
4.2.2	Point Defects	43
4.3	Half-Loop and Double-Kink Excitations	57
4.4	Diffraction Plot/Structure Factor	61
4.5	Voltage Noise Spectrum	62
4.5.1	Randomly Placed Point Defects	62
4.5.2	Randomly Placed Columnar Defects	66
5	Aging Dynamics	73
5.1	Preparation of the System	73
5.2	Dynamical Scaling Behavior	76
5.2.1	A Single Flux Line	76
5.2.2	Varying Pinning Strength	78
5.2.3	Varying Interaction Range	85
5.2.4	Varying Temperature	89
5.2.5	Varying Defect Density	92
5.2.6	Conclusions	100
6	Discussion and Conclusion	101

List of Figures

2.1	Meissner effect	8
2.2	Magnetization curves	8
2.3	Temperature dependence of the critical field	9
2.4	Magnetic flux penetration near the surface of superconductor	11
2.5	Behavior of characteristic lengths scales	13
2.6	Lorentz force on the flux lines	14
2.7	Abrikosov vortex lattice, Bragg glass, vortex glass, Bose glass, and liquid vortex phase	16
2.8	Free energy for the ferromagnetic system	21
3.1	Half-loop and Double-kink excitation	28
4.1	Metastable states at low driving forces	33
4.2	Time line for the simulation	33
4.3	Defects configurations	37
4.4	I-V curves for different types of defects	38
4.5	I-V curves for various vortex densities with columnar defects	39
4.6	Critical currents for various vortex densities with columnar defects	39
4.7	I-V curves for various vortex densities with point defects	40
4.8	Critical currents for various vortex densities with point defects	40
4.9	Radius of gyration along the x-axis for systems with columnar defects	46
4.10	Radius of gyration along the y-axis for systems with columnar defects	46
4.11	Radius of gyration for systems with columnar defects	47
4.12	Snapshots of moving vortices, columnar defects	48
4.13	Snapshots of Bose glass phase for various vortex density	49

4.14	Snapshots of vortex lines in the critical regime for various vortex density	50
4.15	Snapshots of vortex lines in the flowing regime for various vortex density	51
4.16	Radius of gyration along the x-axis for systems with point defects	52
4.17	Radius of gyration along the y-axis for systems with point defects	52
4.18	Radius of gyration for systems with point defects	53
4.19	Snapshots of moving vortices, point defects	54
4.20	Snapshots of moving vortex lines for various vortex density with point defect	55
4.21	Saddle point parameters	58
4.22	Number of half-loops for systems with columnar defects	60
4.23	Number of double-kinks for systems with columnar defects	60
4.24	Diffraction plot	61
4.25	Voltage noise for point defects, x-axis	64
4.26	Voltage noise for point defects, y-axis	65
4.27	Voltage noise, point defects	66
4.28	Voltage noise for columnar defects, x-axis	70
4.29	Voltage noise for columnar defects, y-axis	71
4.30	Voltage noise, columnar defects	72
5.1	Algorithm for the aging simulation	75
5.2	The decay of the density autocorrelation function	75
5.3	Aging for noninteracting vortices with no defects	77
5.4	Aging for noninteracting vortices with no defects	77
5.5	Aging for interacting vortices with no defects	80
5.6	Aging for interacting vortices with no defects as a function t/s	81
5.7	Aging for $T=10$, $\lambda = 35$, $dist = 9$, and $pin=0.01$ as a function of $t - s$	82
5.8	Aging for $T=10$, $\lambda = 35$, $dist = 9$, and $pin=0.01$ as a function of t/s	82
5.9	Aging for $T=10$, $\lambda = 35$, $dist = 9$, and $pin=0.02$ as a function of $t - s$	83
5.10	Aging for $T=10$, $\lambda = 35$, $dist = 9$, and $pin=0.02$ as a function of t/s	83
5.11	Aging for $T=10$, $\lambda = 35$, $dist = 9$, and $pin=0.05$ as a function of $t - s$	84
5.12	Aging for $T=10$, $\lambda = 35$, $dist = 9$, and $pin=0.05$ as a function of t/s	84
5.13	Aging for $T=10$, $\lambda = 25$, $dist = 9$, and $pin=0.02$ as a function of $t - s$	86

5.14	Aging for $T=10$, $\lambda = 25$, $dist = 9$, and $pin=0.02$ as a function of t/s	86
5.15	Aging for $T=10$, $\lambda = 20$, $dist = 9$, and $pin=0.02$ as a function of $t - s$	87
5.16	Aging for $T=10$, $\lambda = 20$, $dist = 9$, and $pin=0.02$ as a function of t/s	87
5.17	Aging for $T=10$, $\lambda = 10$, $dist = 9$, and $pin=0.02$ as a function of $t - s$	88
5.18	Aging for $T=10$, $\lambda = 10$, $dist = 9$, and $pin=0.02$ as a function of t/s	88
5.19	Aging for $T=20$, $\lambda = 35$, $dist = 9$, and $pin=0.02$ as a function of $t - s$	90
5.20	Aging for $T=20$, $\lambda = 35$, $dist = 9$, and $pin=0.02$ as a function of t/s	90
5.21	Aging for $T=50$, $\lambda = 10$, $dist = 9$, and $pin=0.02$ as a function of $t - s$	91
5.22	Aging for $T=50$, $\lambda = 10$, $dist = 9$, and $pin=0.02$ as a function of t/s	91
5.23	Aging for $T=10$, $\lambda = 35$, $dist = 12$, and $pin=0.02$ as a function of $t - s$	93
5.24	Aging for $T=10$, $\lambda = 35$, $dist = 12$, and $pin=0.02$ as a function of t/s	93
5.25	Aging for $T=10$, $\lambda = 35$, $dist = 15$, and $pin=0.02$ as a function of $t - s$	94
5.26	Aging for $T=10$, $\lambda = 35$, $dist = 12$, and $pin=0.02$ as a function of t/s	94
5.27	Aging for $T=10$, $\lambda = 35$, $dist = 20$, and $pin=0.02$ as a function of $t - s$	95
5.28	Aging for $T=10$, $\lambda = 35$, $dist = 20$, and $pin=0.02$ as a function of t/s	95
5.29	Aging for various pinning strengths	96
5.30	Aging for various vortex interaction ranges	96
5.31	Aging for various temperatures	97
5.32	Aging for various defect densities	97
5.33	Asymptotic behavior for different systems	98
5.34	Dynamics Exponents	99

List of Tables

1.1	Critical parameters of various superconductors:The original data are reported in Ref.[5]	3
4.1	Critical depinning threshold for various vortex density	36
4.2	Fluctuations in the radius of gyration: columnar and point defects	56
4.3	Maximal radius of gyration for the system with point defects	56
4.4	Predicted washboard frequency for columnar defects : x-component	69
4.5	Predicted length scale for columnar defects: x-component	69
5.1	Dynamical scaling exponents b and λ_c/z for various systems.	99

Chapter 1

Introduction

1.1 History of Superconductivity

The discovery of superconductivity [1] in 1911 by Kamerlingh-Onnes caused great enthusiasm and eagerness for scientists and engineers to search for practical applications for this class of materials, mainly because of its potential to conserve energy. One of the hallmarks of superconductivity is the sudden drop to zero of electrical resistance of a material, *perfect conductivity*, as the temperature and applied magnetic field are brought lower than the transition point, i.e., critical temperature and critical magnetic field above which superconductivity is destroyed. Superconductivity has been found early in various elements such as mercury, lead, and aluminum but, surprisingly, not for the best conductors at room temperature such as gold, silver, and copper.

Most of the early superconductors are superconducting at extremely low transition temperature and magnetic field. For example, superconductivity of mercury can be maintained up to a transition temperature of 4.15 K and a transition field of 41 mT. Superconductivity tends to disappear in most early superconductors due to self-generated magnetic fields when the current densities through them are increased to practical levels. Another concern was the high cost and complexity of operating refrigeration equipment near liquid helium temperatures (4 K, -269C). Such superconductors therefore have been limited to practical usefulness due to extremely small values of the transition temperature and initial magnetic field.

Until 1986 the record for highest critical temperature was 23 K for Nb₃Ge. At that time, two classes of superconductors were classified by their magnetic properties. Type-I superconductors, mostly pure metals, were classified as materials with a sharp transition from the superconducting to the normal state. Type-II superconductors are materials displaying a gradual transition and intermediate state. In this so-called “mixed state” or “vortex state”, quantized magnetic flux can penetrate into the superconductor in the form of “vortices”, i.e., a state when the coexistence between normal and superconducting regions is allowed. In chapter 2, the difference between type-I and type-II superconductors will be discussed in more detail.

In 1986 a new La-Ba-based copper-oxide superconductor, $(\text{La, Ba})_2\text{CuO}_4$, with transition temperature of 35 K was discovered by Bednorz and Müller [2]. It was subsequently established during the past decades that superconductivity in these “high temperature” superconductors (HTS) containing Y, Bi, Tl, and Hg instead of La can be maintained up to much higher magnetic field and temperature. Moreover, materials of this class of oxides have been discovered with transition temperature well above 100 K. Some of those copper-oxide materials that most of the work has been focused on are YBCO ($\text{YBa}_2\text{Cu}_3\text{O}_7$, $T_c \approx 93\text{K}$) and BSCCO ($\text{Bi}_2\text{Sr}_2\text{Ca}_2\text{Cu}_2\text{O}_8$, $T_c \approx 85\text{K}$, and $\text{Bi}_2\text{Sr}_2\text{Ca}_2\text{Cu}_3\text{O}_{10}$, $T_c \approx 110\text{K}$). The highest critical temperature record, 195 K, at this time of writing, September 2008, has recently been reported by superconductors.org for $(\text{Sn}_1\text{Pb}_{0.5}\text{In}_{0.5})\text{Ba}_4\text{Tm}_6\text{Cu}_8\text{O}_{22+}$. These high temperature superconductors can be classified as type-II superconductors. High temperature superconductors therefore can be maintained in the superconducting state by means of liquid nitrogen with boiling temperature of 77 K. Such superconductors are therefore suitable for a broader range of practical applications such as magnets, motors, and generators. The superconducting parameters of both type-I and type-II superconductors are listed in Table 1.1.

Until now, scientists and researchers still put great efforts in searching for new superconductors with the hope that they will be able to find room temperature superconductors. It is well known that copper oxide based superconductors are brittle and cause difficulties in practical applications. In 2001, the discovery of non-oxide based superconductor in MgB_2 by Nagamatsu and Akimitsu [3] has restored the huge interest in the field of superconductivity. MgB_2 has remarkable properties such as high transition temperature, high critical current density and magnetic field ($> 0.6\text{T}$), and especially for its simple hexagonal structure. This material becomes a binary compound with the highest critical temperature of approximately 40 K, almost three or four times lower than critical temperature for copper oxide-based high temperature superconductors. There is one important reason that makes this material so special for its applications, the cost for fabrication into useful forms, such as a wire or cable, using MgB_2 is much lower than the mercury-based cuprate wire.

In February 2008, Hideo Hosono (from the Tokyo Institute of Technology in Japan) [4] has discovered an iron-based superconducting material in LaOFFeAs . Despite the fact that the critical temperature for this iron-arsenide compound with lanthanum, oxygen and fluorine was only 26 K, it was surprising that there could be another material other than the cuprate which could become superconducting at such elevated temperatures. In addition, the discovery of this new iron-based superconductor is very important from a theoretical aspect. In general, a compound containing iron atoms usually forms ferromagnetic materials, which destroy superconductivity. The recent discovery of non-oxide superconductors in MgB_2 and iron-based compound LaOFFeAs would also assist theoretical physicists to be closer to a fundamental understanding in the basic mechanism behind high-temperature superconductivity.

Table 1.1: Critical parameters of various superconductors: The original data are reported in Ref.[5]

	Superconductor	T_c (K)	$\mu_0 H_c$ (mT)	$\mu_0 H_{c1}(0)$ (mT)	$\mu_0 H_{c2}(0)$ (T)
Type-I	Hg(α)	4.15	41	-	-
	In	3.41	28	-	-
	Pb	7.20	80	-	-
	Ta	4.47	83	-	-
Type-II	Nb	9.25	199	174	0.404
	Nb ₃₇ Ti ₆₃	9.08	253		15
	Nb ₃ Sn	18.3	530		29
	Nb ₃ Al	18.6			33
	Nb ₃ Ge	23.2			38
	V ₃ Ga	16.5	630		27
	V ₃ Si	16.9	610		25
	PbMo ₆ S ₈	15.3			60
	MgBr ₂	39	660		
	YBa ₂ Cu ₃ O ₇	93	1270		
	(Bi, Pb) ₂ Sr ₂ Ca ₂ Cu ₃ O _x	110			
	Tl ₂ Ba ₂ Ca ₂ Cu ₃ O _x	127			
	HgBa ₂ CaCu ₂ O _x	128	700		
	HgBa ₂ Ca ₂ Cu ₃ O _x	138	820		

1.2 Applications of HTS Materials

Some limitations in these HTS applications technically/technologically remain because these ceramic oxide materials are brittle and not easy to fabricate in useful forms, i.e., superconducting wires. Resistance-induced fluctuations in these ceramic oxide materials are much more prominent than those in classic superconductors mentioned above for several reasons. First, operation at higher temperatures inevitably causes thermal fluctuations to be more significant. Second, the high transition temperature and the low Fermi velocity due to the low electron density in copper oxide materials result in a short coherence length, which causes enhanced spatial fluctuation of vortices. These fluctuations result in energy losses and constitute resistance which account for most of the energy consumed in electrical devices. Regardless of these practical difficulties, our intellectual understanding of fundamental properties of superconductors has been increased due to an enormous volume of research.

Some of the successful applications for HTS materials include small-scale electronic components, superconducting wires, cables, and magnets [6, 7]. These applications make use of high-temperature superconductors to replace existing designs based on normal conductors. Compared to conventional devices, HTS components can be significantly reduced in size while their performance is improved. Because, in principle, there are no electrical losses, power consumption in the components is low. High-temperature superconducting microwave components including filters, antennas, resonators, and transmission lines have already been in the market [8, 9].

The most success has been achieved with HTS small-scale devices that rely on the special properties of superconductors, especially the Josephson quantum tunnelling effects. The best-known device is the SQUID, Superconducting Quantum Interference Device, magnetometer [10]. A SQUID contains a ring of superconductor with one or more Josephson junctions. When a current applied to the SQUID becomes larger than the critical current of the Josephson junctions, a voltage appears proportional to the magnetic flux through the SQUID ring. The SQUID is so extremely sensitive that it can detect magnetic fields 100 billion times smaller than the Earth's field.

Among the large scale applications, superconducting magnets are already crucial components of several technologies. Magnetic resonance imaging (MRI) is used in diagnostic medicine [11]. The intense magnetic fields that are needed for these instruments are a perfect application of superconductors. Similarly, particle accelerators used in high-energy physics studies are very dependent on high-field superconducting magnets.

1.3 Theoretical and Experimental Survey

From a theoretical and experimental point of view, vortex matter in disordered high-temperature superconductors has attracted much attention in the field of condensed matter physics during past decades. The possibility of practical applications of superconductivity depends on the maximum current density which superconductors can carry. This

is directly related to the flux pinning of quantized magnetic flux lines in type-II superconductors. Different experimental techniques such as magnetic decoration [12], scanning Hall probes [13], small angle neutron scattering [14], scanning tunneling microscope imaging [15], and Lorentz microscopy [16] are utilized to capture the static structure of these flux lines pinned by quenched disorder. These studies provide us only the image of static structure of flux lines on the top layer but not the internal structure of the moving flux lines in response to the external current. By using neutron diffraction [17] to image the flux lattice, we can study the motion of these flux lines, e.g., by compiling a sequence of these images of vortex positions into a movie.

Aside from the technological applications of superconductors, the statics and dynamics of vortices in the type-II superconductors in the presence of quenched disorder and external driving force has been much investigated recently. In the absence of quenched disorder, the Abrikosov vortex lattice is observed [18]. The presence of a small fraction of pinning centers can destroy the long-range order of the lattice and results in different spatial structures depending on the nature of the pinning centers. In systems with randomly distributed weak pinning centers, the vortex lattice deforms and transforms into a quasi-long-range order Bragg glass at low fields [19, 20, 21]. A vortex glass characterized by complete loss of translational order is observed if the pinning strength or fields are higher [22, 23]. If correlated defects such as parallel columnar defects are present in the system, the effective pinning force adds coherently and results in the Bose glass phase of localized flux lines [24]. This type of artificial defects can be produced by energetic heavy ion radiation.

The moving glass theory of driven lattices with disorder showing various moving lattice phases has been proposed [25]. In the presence of an external drive, flux lines encounter the Lorentz force and tend to move along the direction of the drive. Disorder tends to inhibit the flux line motion and leads to different characteristics of the flow. In the presence of randomly distributed point defects, the moving glass is characterized by the decay of translational long-range order, the presence of stationary channels of vortex motion, and highly correlated channel patterns along the direction transverse to the motion. If the disorder strength is weak, this would result in a topologically ordered moving Bragg glass, which is the flowing of static Bragg glass. For the intermediate pinning strength, the moving transverse glass with a smectic order in the direction transverse to the flow exists. A moving Bose glass is predicted in the case where correlated disorder is present in the system.

The system that we study, at low-temperature, is in a glassy state [26]. Vortex lines do not manage to equilibrate with its environments and evolve very slowly in time in an out of equilibrium manner. The experimental time window for the evolution is much larger in comparison to the numerical simulation time. The advantage of using numerical simulations is manifold. First, and more importantly, it allows us to identify the minimal ingredients needed to reproduce the experimental observations. Second, it allows us to explore the effect of the microscopic parameters in the model. Third, it allows us to grasp what vortices are actually doing by direct visualization [27, 28].

The relaxation of these flux lines strongly depends on the initial condition. Vortex

lines in a sample prepared by zero-field cooling (ZFC), in which the external magnetic field is applied after cooling down the sample to the temperature of study, are expected to be more ordered compared to a system prepared by field cooling (FC), in which the external magnetic field is applied above the transition temperature and then cooled down to the temperature of study [29]. The relaxation dynamics of flux lines in dirty high-temperature superconductors has been analyzed numerically [30, 31], and experimentally [32].

1.4 Objective and Motivation of Study

There are two main points of investigation in this work. The first one is to characterize properties of interacting vortices in the presence of an external driving force and subject to strong point and columnar pinning centers: characterization of the nonequilibrium steady states. Bullard [33] has investigated and fully characterized the effect of different pinning structures on the velocity noise spectrum of the moving vortices. The system is characterized by measuring physical observables including force-velocity/ current-voltage curve, vortex spatial arrangement and static structure factor, mean vortex radius of gyration, and voltage/ velocity noise features. In addition to the work by Bullard, one of our goals is to probe the effect of different configurations of strong pinning centers on the internal vortex structure. The internal structure of driven vortex lines is not easily accessible in experiment. It was predicted by Nelson and Vinokur [34] that, at the lowest drive, the transition of flux lines from one columnar defect to another can take place via thermally activated double-kink configuration and via half loops at intermediate drive. Better understanding of electrical and transport properties of type-II superconductors could give rise to new commercial innovations in our every day lives. The second part of this work will discuss the nonequilibrium relaxation in the glassy phase of interacting vortices. The two-time density-density correlation function will be used to study the aging dynamics. It will be investigated whether the “simple aging” or “subaging” scenarios apply to our system of interest.

Chapter 2

Theoretical Approach

2.1 Superconducting Phenomena

Since the discovery of superconductivity by Kamerlingh-Onnes in 1911, massive progress in fundamental understanding of electrical, magnetic, and transport properties of superconductors has been made [35, 36]. One of the hallmarks of superconductivity is the sudden drop of electrical resistance to zero below the critical temperature T_c : This is *perfect conductivity*. Advantage is taken of this property for most potential applications, such as high-current transmission lines or high-field magnets. Another hallmark of superconductivity is the *perfect diamagnetism* or the *Meissner effect*, the ability of the superconductor to completely expel the weak magnetic field as it is cooled through T_c . As the external magnetic field increases above the critical field H_c , superconductivity is destroyed. The phenomenological theory describing the fundamental electromagnetic properties of superconductors was first proposed by Fritz and Heitler London in 1935. A remarkably complete and satisfactory theoretical picture of the classic superconductors was established in the 1950s and 1960s through the Bardeen-Cooper-Schrieffer (BCS) [37] and Ginzburg-Landau (GL) theories [38]. The BCS theory proved that electrons near the Fermi level form so-called Cooper pairs due to a weak, phonon-mediated attraction between electrons. This condensation of electrons results in an energy gap which inhibits the kind of collision interactions leading to ordinary resistivity. Later in 1986, a new class of high-temperature or type-II superconductors was discovered by Bednorz and Müller. In these materials the superconductivity can be maintained up to a very high field, which is therefore suitable for application in high-field devices. However, BCS theory fails to account for the onset of superconductivity in new iron-based compounds and, hence, there is still no complete theory describing superconductivity. Two types of superconductors are classified according to their magnetic properties [35].

First, magnetization curves for type-I and type-II superconductors are different. The magnetization of a type-I superconductor, when the external magnetic field H_e is lower than the critical field H_c , is given by

$$M = -H_e \tag{2.1}$$

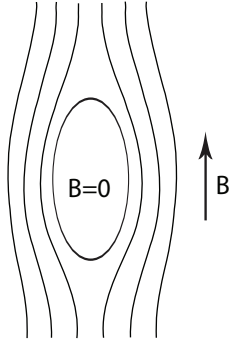


Figure 2.1: The Meissner effect: magnetic flux is totally excluded from interior of bulk superconductor as it is cooled through critical temperature T_c .

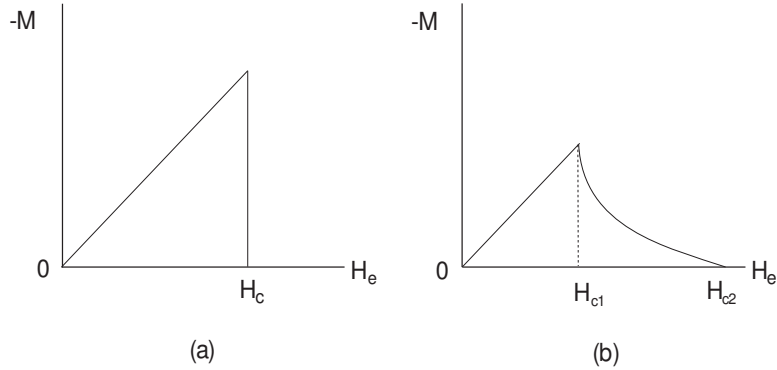


Figure 2.2: Magnetic field dependence of the magnetization for (a) a type-I superconductor with a sharp transition at the critical field, and (b) a type-II superconductor with a gradual transition.

and the superconductor is in the Meissner state ($M + H = 0$). Above the critical field H_c the transition from the superconducting state occurs with the discontinuity of the magnetization from $M = -H_c$ to $M = 0$. For type-II superconductors, the magnetization of $M = -H_e$ is maintained up to the lower critical field H_{c1} and decreases continuously to $M = 0$ at H_{c2} . This is shown in Fig. 2.2.

Secondly, the temperature dependence of the critical magnetic field is also different. For type-I superconductors, superconductivity is destroyed at the critical temperature H_c . Type-II superconductors remain in the Meissner state up to H_{c1} and enter the normal state above H_{c2} . The coexistence of the superconducting and normal state between H_{c1} and H_{c2} is called the *vortex state* or *mixed state*. In this state, the magnetic flux penetrates the superconductor in the form of quantized vortices. The dependence of the critical field on the temperature for type-I superconductors [35] is well known according to the relationship

$$H_c(T) = H_c(0) \left[1 - \left(\frac{T}{T_c} \right)^2 \right] \quad (2.2)$$

However, this relationship does not hold for type-II superconductors. The mean-field phase diagram, i.e., the magnetic field vs. temperature, in Fig. 2.3 shows the mixed state

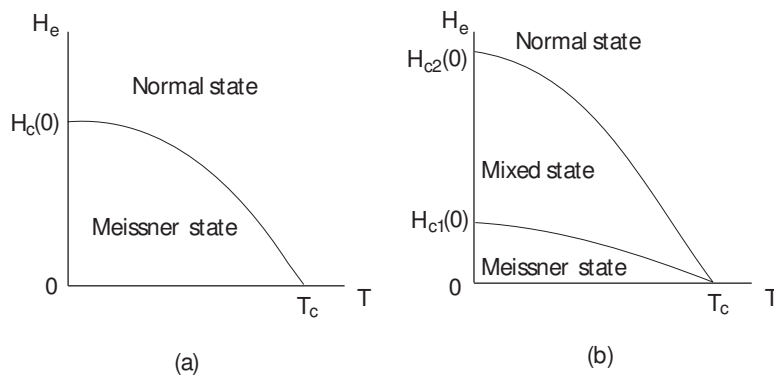


Figure 2.3: Temperature dependence of critical field for (a) type-I superconductor with a sharp transition at the critical field and (b) type-II superconductors with an existence of a mixed state between H_{c1} and H_{c2} .

for type-II superconductors. The lower and upper critical fields reduce to zero at the critical temperature T_c .

Another method to classify the types of superconductors is by determining the surface energy in the intermediate state. The Ginzburg-Landau theory will be explained in the next two sections.

2.2 London Theory

After the discovery of superconductivity, it was not until 1935 that the London theory was proposed in order to explain the fundamental electromagnetic properties of classic superconductors such as perfect conductivity and the Meissner effect. Following the discussions by Tinkham [35], it starts with the equation of motion for the Drude model for electrical conductivity, of (superconducting) electrons given by

$$m \frac{d\mathbf{v}}{dt} = -e\mathbf{e} - \frac{m\mathbf{v}}{\tau}, \quad (2.3)$$

where m , \mathbf{v} , $-e$, and \mathbf{e} are the mass, the average velocity, the electric charge of the electrons, and the electric field. τ is the phenomenological relaxation time of the electrons to scatter and bring the drift velocity to zero. In a normal metal, electrons scatter in random directions, which results in a steady state solution where the average velocity (drift velocity) is independent on time $d\mathbf{v}/dt = 0$. In order to explain the perfect conductivity in superconductors, we consider a perfect normal conductor with mean free path $l = \infty$. This would mean that the relaxation time is infinite, $\tau \approx \infty$, and leads Eq. 2.3 to

$$m^* \frac{d\mathbf{v}_s}{dt} = -e^*\mathbf{e}, \quad (2.4)$$

where m^* , \mathbf{v}_s , and e^* now represent the mass, average velocity, and the electric charge of the superconducting carriers. The superconducting current density is given by

$$\mathbf{j} = -n_s e^* \mathbf{v}_s, \quad (2.5)$$

where n_s is the number density of superconducting electrons. From Eq. 2.3 and Eq. 2.4 the first equation equivalent to the London equation explaining the perfect conductivity is written as

$$\mathbf{e} = \frac{m^*}{n_s e^{*2}} \cdot \frac{d\mathbf{j}}{dt}. \quad (2.6)$$

It is easy to see that superconducting electrons would flow freely with the superconducting current density \mathbf{j} if they are not accelerated by an external electric field, i.e., if there is no electric field applied to the system, the superconducting current density will not change.

To explain the perfect diamagnetism, we begin by taking the curl of both sides of the Maxwell equation $\nabla \times \mathbf{h} = 4\pi\mathbf{j}/c$ and Eq. 2.6, where \mathbf{h} is the magnetic field. We then substitute $\nabla \times \mathbf{j}$ obtained from the previous step to the term on the right hand side of Eq. 2.6 after taking the curl on both sides. Next eliminate the term on the left hand side by the use of the Maxwell equation $\nabla \times \mathbf{e} = -\frac{1}{c}\frac{\partial\mathbf{b}}{\partial t}$ and $\mathbf{b} = \mathbf{h}$, where \mathbf{b} is the magnetic flux density. The equation is rewritten as

$$\frac{\partial}{\partial t} \left(\frac{1}{c}\mathbf{b} + \frac{m^*c}{4\pi n_s e^{*2}} \nabla \times \nabla \times \mathbf{b} \right) = 0. \quad (2.7)$$

Thus, the quantity in the parenthesis in the above equation is independent of time. The Meissner effect can be explained if we set this quantity to zero

$$\mathbf{b} + \frac{m^*c^2}{4\pi n_s e^{*2}} \nabla \times \nabla \times \mathbf{b} = 0. \quad (2.8)$$

The second London equation is obtained if we rewrite Eq. 2.8 as

$$\nabla^2 \mathbf{b} - \frac{1}{\lambda^2} \mathbf{b} = 0 \quad (2.9)$$

with the replacement of $\nabla \times \nabla \times \mathbf{b}$ by $-\nabla^2 \mathbf{b}$ (since $\nabla \cdot \mathbf{b} = 0$) and the characteristic length

$$\lambda = \left(\frac{m^*c^2}{4\pi n_s e^{*2}} \right)^{1/2}. \quad (2.10)$$

The second London equation, therefore, explains the Meissner effect and gives a phenomenological approximation of the measurable penetration length λ in terms of the superconducting electron density n_s . If we apply the external magnetic field H_e along the the z -axis parallel to the surface of a thin slab of superconductor ($x=0$), we have

$$\frac{d^2b}{dx^2} - \frac{b}{\lambda^2} = 0. \quad (2.11)$$

The solution for this equation under the condition that $b = H_e$ at $x = 0$ and $b = 0$ at infinity is

$$b(x) = H_e \exp\left(-\frac{x}{\lambda}\right) \quad (2.12)$$

Thus, the magnetic flux can penetrate the superconductor within the order of the *penetration length* λ from the surface. This is shown in Fig. 2.4. With the electronic charge

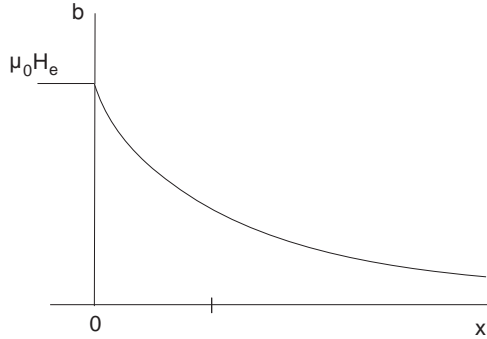


Figure 2.4: Magnetic flux can penetrate the superconductor within the order of the penetration length λ from the surface.

of the *Cooper pair* $e^* = 2e = 3.2 \times 10^{-19}$ C and the mass of a superconducting electron $m^* = 2m = 1.8 \times 10^{-30}$ kg, the range of the typical value of λ at temperature $T = 0$ varies from 100 Å to 2000 Å, which is small in comparison to the thickness x of the sample. Thus, this theory explains the Meissner effect such that the magnetic flux \mathbf{b} can penetrate into the sample only for a small distance from the surface and becomes zero at $x \gg \lambda$.

2.3 Ginzburg-Landau Theory

The London theory provides a good explanation for Meissner effect in type-I superconductors. However, it fails to explain the intermediate state of a type-I superconductor or vortex state of type-II superconductor when there exists coexistence between normal and superconducting regions inside the sample. Ginzburg-Landau theory, which is based on the theory of phase transitions, was proposed to explain the intermediate and the vortex state. All equations in this subsection follow the discussions by Tinkham [35]. The free energy density in the superconducting state can be written as

$$F_s = F_n(0) + \alpha|\Psi|^2 + \frac{\beta}{2}|\Psi|^4 + \frac{1}{8\pi}(\nabla \times \mathbf{A})^2 + \frac{1}{2m^*}|(-i\hbar\nabla + \frac{2e\mathbf{A}}{c})\Psi|^2, \quad (2.13)$$

where the last two terms are the free energy due to the magnetic field $\mathbf{B} = \nabla \times \mathbf{A}$ and the kinetic energy. An order parameter Ψ denotes the superconducting electron wave function with $|\Psi|^2$ to be identified with the number density of superconducting electrons n_s . The fourth term is the free energy density due to the external magnetic field, where \mathbf{A} is the vector potential. Clearly, if $\Psi = 0$, this reduces to the free energy density of the normal state $F_n(0) + \frac{1}{8\pi}(\nabla \times \mathbf{A})^2$. The important result of this theory is derived by minimizing the free energy $\int F_s dV$ with respect to $\Psi^*(\mathbf{r})$ and $\mathbf{A}(\mathbf{r})$. The ensuing Ginzburg-Landau differential equations are written as

$$\frac{1}{2m^*}(-i\hbar\nabla + \frac{2e\mathbf{A}}{c})^2\Psi + \alpha\Psi + \beta|\Psi|^2\Psi = 0, \quad (2.14)$$

$$\mathbf{j} = \frac{\hbar e}{m^*i}(\Psi^*\nabla\Psi - \Psi\nabla\Psi^*) - \frac{4e^2}{m^*c}|\Psi|^2\mathbf{A}. \quad (2.15)$$

The approximation $\Psi = \Psi_\infty$ is allowed in the superconducting state, i.e. the order parameter varies slowly in space. This would reduce Eq. (2.15) to

$$\mathbf{j} = -\frac{4e^2}{m^*c}|\Psi_\infty|^2\mathbf{A}. \quad (2.16)$$

This is similar to the result from the London theory if $|\Psi_\infty|^2 = n_s$ and $e^* = 2e$ are applied. The penetration depth can be derived in the same manner as in the London theory and is given by

$$\lambda = \left(\frac{m^*c^2}{4\pi e^{*2}|\Psi_\infty|^2} \right)^{1/2}. \quad (2.17)$$

If we assume that, in the absence of the external magnetic field or $\mathbf{A} = 0$, the order parameter varies slightly from its equilibrium value, $\Psi/|\Psi_\infty| = 1 - f$, then Eq.(2.14) reduces to

$$\xi^2 \frac{d^2 f}{dx^2} - 2f = 0 \quad (2.18)$$

such that its solution is

$$f \sim \exp\left(-\frac{\sqrt{2}|x|}{\xi}\right) \quad (2.19)$$

with

$$\xi = \frac{\hbar}{2\sqrt{2}eH_c\lambda}. \quad (2.20)$$

The characteristic length ξ is called coherence length. This shows that the order parameter Ψ exponentially decays in space of the order of the coherence length ξ . Fig. 2.5 shows the behavior of the penetration length and coherence length at an interface between the superconducting and normal domains. The typical value of the coherence length in classic superconductors is about 3000 Å. The ratio of these two characteristic lengths $\kappa = \lambda/\xi$ is called the GL parameter. This parameter plays a role in determining types of superconductors and the critical field of the type-II superconductors.

Abrikosov [39] analytically investigated fundamental properties of superconductors for different values of the GL parameter κ . By calculating the surface energy at the interface between the normal and superconducting regions, it can be shown that the surface energy can be approximated by $H_c^2(\xi - \lambda)/8\pi$. In the limit of small κ , $\xi > \lambda$, it was found qualitatively that there is a positive surface energy associated with an interface between the normal and superconducting state of thickness $\approx (\xi - \lambda)$. In this region, the system pays the energetic cost of excluding the magnetic field. For large κ , $\xi < \lambda$, the system would have a negative surface energy. In this limit, the system would undergo the process of subdivision into domains to maximize the negative surface energy. Abrikosov called materials with large κ type-II superconductors in order to distinguish them from type-I superconductors with small κ . Abrikosov showed that the superconducting state may exist in an external magnetic field higher than the critical field H_c if κ for such materials

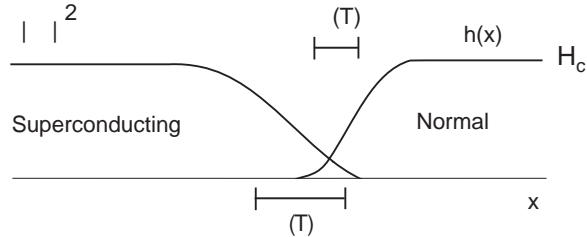


Figure 2.5: Behavior of the order parameter $|\Psi|^2$ and magnetic field \mathbf{h} at the interface between the superconducting and normal domains in classic superconductors. The order parameter $|\Psi|^2$ exponentially decays into the normal domain within an order of coherence length ξ .

is larger than $1/\sqrt{2}$. Therefore, in this context, type-I superconductors have κ less than $1/\sqrt{2}$ and type-II superconductors have κ greater than $1/\sqrt{2}$. He then showed that the upper limit of the critical field in type-II superconductors can be approximated by

$$H_{c2} = \sqrt{2}\kappa H_c \text{ and } H_{c1}H_{c2} = H_c^2. \quad (2.21)$$

2.4 Disorder and Flux Pinning

From a practical point of view, one of the most useful applications of type-II superconductivity is a superconducting magnet which can provide a large magnetic field without dissipation of energy due to the resistanceless current of the superconducting solenoid. At such a high magnetic field, a superconducting wire is in the vortex state with magnetic flux penetrating through it. Therefore, the superconducting material used to make such magnets must have a critical field much higher than the desired field and must be able to carry a high current without resistance. Such high fields can be found in most of oxide-based superconductors as shown in Table 1.1. Hence, the only problem left here is to find a material which can carry a high current in the presence of magnetic vortices without dissipation of energy. In the presence of an external current, a vortex will experience a Lorentz force [35]

$$\mathbf{f} = \mathbf{J} \times \frac{\Phi_0}{c} \quad (2.22)$$

where \mathbf{f} is the force per unit length on the vortex, \mathbf{J} is the current density, and Φ_0 is the quantized magnetic flux parallel to the applied field. As shown in Fig. 2.6, if the flux lines are driven by this Lorentz force, they tend to move transverse to the applied current with velocity \mathbf{v} , the electric field parallel to \mathbf{J} is induced

$$\mathbf{E} = \mathbf{B} \times \frac{\mathbf{v}}{c} \quad (2.23)$$

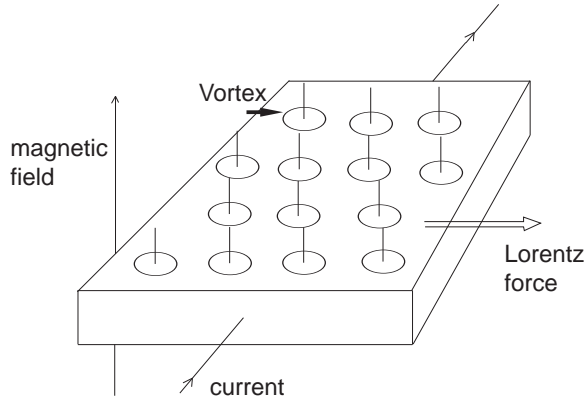


Figure 2.6: Type-II superconductors in the presence of applied current and magnetic field. The induced Lorentz force acts on the flux lines in the direction transverse to the applied current and magnetic field.

where \mathbf{B} is the macroscopic magnetic flux density. When this state is maintained steadily, an energy dissipation, and hence an electrical resistance, should appear as in a normal metal.

To solve this problem, it is necessary to stop the motion of flux lines by providing the system with inhomogeneities and various types of artificial defects such as dislocations, normal precipitates, columnar defects produced by heavy-ion irradiation, and grain boundaries so as to maintain large non-dissipative currents under high magnetic fields. Such a mechanism produces a pinning force density \mathbf{F}_p , which pins the vortices to fixed locations in the material until the Lorentz force exceeds the critical current density \mathbf{J}_c . If the pinning strength is sufficiently strong, it will result in the pinned vortex lines state so that the superconductor acts like a perfect conductor. Above the critical current density \mathbf{J}_c , the motion of flux lines and the resistance start to appear, the Lorentz force acting on the flux lines overcomes the pinning force density. Hence, the relation for their magnitudes can be written as

$$J_c = \frac{F_p c}{B}. \quad (2.24)$$

This critical current density inevitably depends on the density, strength, type of, and spatial arrangement of the pinning centers, which also play an important role in the static and dynamic properties of the vortex state in type-II superconductors. Some important experiments and numerical and analytical studies for the static and dynamic of vortices will be discussed in the following subsections.

2.5 Equilibrium States

In the absence of applied currents and disorder, it has long been recognized that weakly interacting flux lines in the vortex state form a perfect triangular lattice of flux lines known as Abrikosov vortex lattice [39]. This is shown in Fig. 2.7 (a). It was originally

approximated that a square lattice would yield a system with the lowest free energy. Kleiner, Roth, and Autler [18] found later that the triangular lattice of flux lines would have the lowest free energy and stability with respect to the energy of the system with the square lattice. The formation of the triangular array was experimentally confirmed by Essmann and Träuble [40]. In the absence of applied currents, this lowest free energy results from the competition of four energies: thermal energy, which favors a wandering of vortex lines; vortex repulsive interaction, which favors the Abrikosov vortex lattice; pinning energy, which favors disorder-dominated ground states known as the glassy states; and the elastic energy of the flux line. Some important equilibrium phases will be discussed here.

In the absence of disorder, thermal fluctuations also affect the equilibrium phase diagram [41]. The Abrikosov vortex lattice is melted with increasing temperature [42, 43]. At high temperature but below the melting transition temperature T_m , the long-range order of the vortex lattice is destroyed. Flux lines become flexible which results in flux line wandering due to the thermal activation against repulsive vortex-vortex interaction. The vortex solid phase transforms into the vortex-liquid phase described by the large fluctuations of the positions of the vortex lines, of the order of the lattice constant $a_0 \approx (\Phi/B)^{1/2}$. This transition also depends on the applied magnetic field [46]. It was proposed that thermal fluctuations would melt the Abrikosov vortex lattice if the intervortex spacing becomes larger than the range of the interactions, i.e., in the low field regime where the repulsive vortex interaction become less effective while the thermal fluctuations get larger.

The presence of even a small amount of weak pinning centers can lead to the destruction of the crystalline order of the Abrikosov vortex lattice. The formation of a static disordered lattice known as Bragg glass, which is a glass that is nearly as ordered as a perfect crystal, would occur [20, 25]. It is characterized by an algebraic decay of translational order and divergent Bragg peaks in the structure function. The lattice remains in quasi-long-range ordered phase within an order of the lattice spacing. This is shown in Fig. 2.7 (b). If the pinning strength of point defects is much stronger, the Bragg glass no longer exists. The vortex lattice is deformed and frozen in random positions, resulting in the well known vortex glass [22]. This is characterized by a complete loss of translational order at large distance. This is shown in Fig. 2.7 (c).

Another interesting phase of vortex lines can be observed if we introduce columnar defects by heavy ion irradiation, such as Sn, Pb, and Iodine ions, to the sample. The effective pinning force for these columnar defects is much larger than the effective pinning force for point defects since they add coherently over the length of the columnar defect. It has been experimentally confirmed that the critical current density \mathbf{J}_c and magnetization \mathbf{M} of high-temperature superconductors are considerably enhanced by the presence of these columnar defects [47, 48, 49]. In the absence of applied currents, vortex lines may be pinned along the entire length of these columnar defects, resulting in the Bose glass phase [24, 51]. This is shown in Fig. 2.7 (d). In the absence of the driving force, the Mott insulator phase is predicted to exist when the density of the vortices in the system exactly matches the density of the columnar defects, matching field B_Φ . The internal magnetic field B is locked or stays constant over a finite range of the applied magnetic field H .

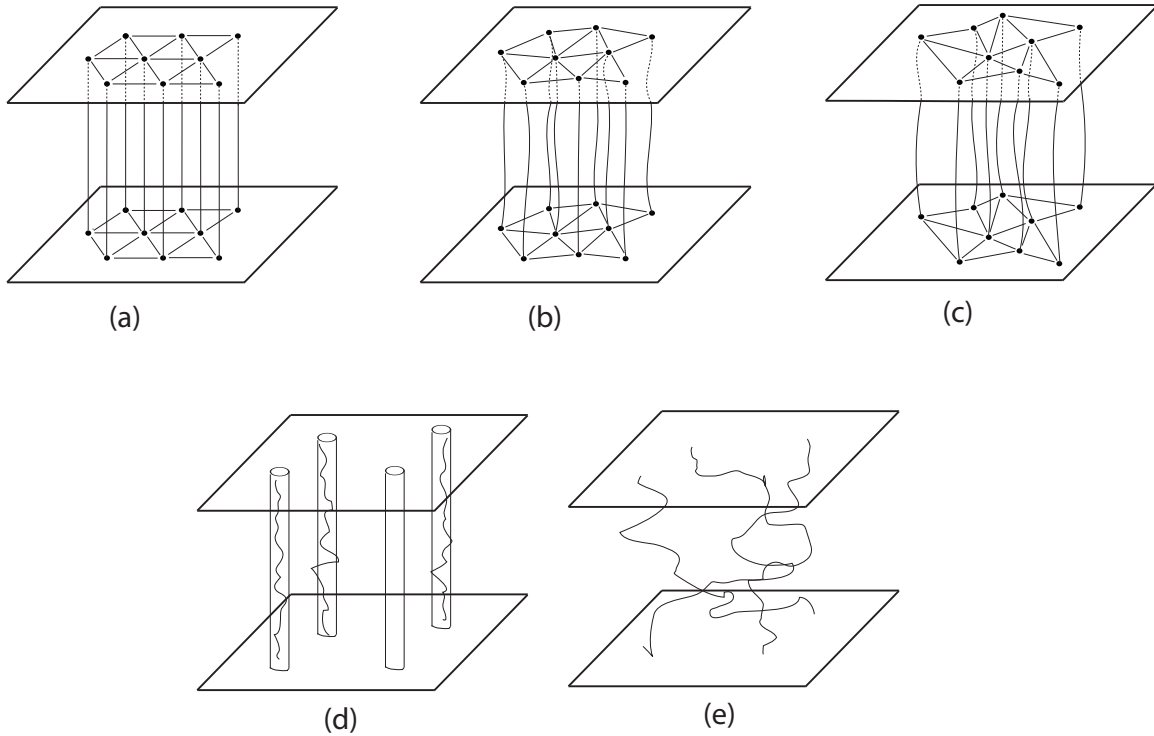


Figure 2.7: A schematic representation of vortex phases in type-II superconductors at low temperatures. (a) In the absence of pinning centers, an Abrikosov vortex lattice with translational long-range order. (b) In the presence of weak point defects, a Bragg glass phase with the loss of translational long-ranged order and no topological defects. (c) In the presence of strong point defects, a vortex glass phase with the complete loss of translational long-range order and the existence of topological defects. (d) In the presence of columnar defects, a Bose glass with translational long-range order. (e) At high temperatures, a vortex liquid phase with entangled flux lines, loss of topological order and Bragg peaks.

Near the critical temperature and field, the glassy states mentioned above are destroyed. Flux lines melt and result in the vortex liquid phase characterized by the absence of translational order and Bragg peaks. Similar to the system without disorder, the flux lines can be entangled due to the large thermal fluctuations, which causes disorder to become insignificant. Flux lines jumps over the pinning potential by thermal activation. This is shown in Fig. 2.7 (e). If the temperatures and fields are further increased, the system will make the transition to the normal metal state with the disappearance of magnetization. The presence of columnar defects tend to increase the melting temperature [52].

2.6 Non-equilibrium Steady States

Recently, considerable efforts have been made to study the dynamics of flux lines in high-temperature superconductors, including flux creep, flux flow, irreversible magnetization,

and the existence of the vortex glass phase [43, 44, 45]. As mentioned in the last section, interacting flux lines form an Abrikosov vortex lattice in clean superconductors when they reach thermal equilibrium. A number of interesting phases appear when these flux lines are driven through disorder. We are interested in the regime where an average value of an observable of these driven flux lines is independent of time, i.e., when these flux lines reach nonequilibrium steady states. Experimentally, two useful tools used to study the dynamics of this system are the I-V characteristics and x-ray diffraction patterns [53, 54]. The former one is directly related to the Lorentz force applied on the vortex line and average velocity of flux lines, respectively. The latter is an aid to visualize/characterize motions or patterns of the moving flux lines.

The emergence of interesting phenomena strongly depends on a variation of parameters, such as temperature, external field, external current, pinning strength, and configurations of pinning centers. Thermal fluctuations have a direct effect on the shape of I-V curves. At temperature $T = 0$, flux lines are mostly pinned and have zero average velocity when the applied drive is lower than the critical current. Near the critical current, the flux lines start to depin and move with non-zero average velocity when the applied drive is increased. At non-zero temperature, the I-V curves are generally divided into three regimes based on the average velocity of the moving flux lines [55].

At low drive, flux lines are in the creep regime where the average velocity is small, but non-zero. In the presence of correlated defects, such as randomly placed columnar defects, it was predicted that flux lines might activate and wander via thermal fluctuation in order to find lower energy configurations, in the form of the half-loop or double-kink excitations [34]. The investigation of these excitations is one of the main goals of this work.

A number of interesting phenomena happen in the vicinity of critical threshold: a competition of vortex-vortex interaction, pinning potential, work due to the driving force, elastic energy, and thermal fluctuation become prominent. In the presence of weak pinning centers such as randomly placed point defects, a topologically ordered Bragg glass [20, 25] deforms and drifts in bundles at high enough field, i.e., when flux lines are strongly interacting. Topological order is maintained in this moving flux line system known as a moving Bragg glass. However, when the applied field is very weak, flux lines are moving independently, with loss of topological order. This is known as a moving vortex glass [25]. If the pinning strength is stronger, some of the flux lines are temporarily trapped and cause the moving flux lines to traverse around them [55]. This is called plastic motion due to the incoherent motion of the flux lines [56, 57]. At this intermediate pinning strength, driven flux lines may form elastic channels along the direction of the driving force. If the translational or smectic order of these channels remains in the direction transverse to the drive, this moving flux line system is called a moving transverse glass. Bragg peaks in the direction transverse to the drive appear in the structure factor plot. The effect due to periodic pinning centers has also been studied [58, 59, 60].

Well below the critical temperature, the vortex glass phase forms if strong disorder is present in the system. It is characterized by a complete loss of topological order of the vortex lattice and algebraically divergent peaks in the structure factor at small reciprocal

lattice vectors. This vortex glass is predicted to exist as a crossover phase from a vortex solid to a vortex liquid phase. Evidence to support the existence of this vortex glass has been predicted and experimentally confirmed by the dynamic scaling behavior of I-V curves [61, 62, 63]. If the temperature is raised near, but still below, the critical temperature, thermal fluctuations become significant. It was proposed that the energy to stretch a flux lattice decreases to zero near the upper critical field more rapidly than the pinning energy. This allows the flux line to become more flexible in that region. It tends to be pinned at pinning centers and hence give rise to a higher critical current. This well-known peak effect can be observed as a dip in the I-V curve or a peak in the magnetic field vs. critical current curve [64, 65, 66].

At high drives, all flux lines flow freely and cause the shape of the I-V curves to be linear, following Ohm's law. In the presence of weak pinning centers and large applied fields or driving forces, these moving flux lines tend to reorder and form a moving Abrikosov lattice [17, 67]. They form elastic channels, which are straight or nearly one-dimensional straight paths along the direction of the flow [68, 69]. These channels are simultaneously coupled in the direction along and transverse to the flow. This is demonstrated by the existence of the periodic Bragg peaks at very large reciprocal lattice vectors.

If the pinning strength is very strong, the moving flux lines will not be able to reorder at any field strengths or driving forces, regardless of any defect configurations [70]. The elastic energy will be less effective and the flux lines will try to stretch in order to have the elastic energy overcoming the pinning force. They are either in the moving liquid or plastic phases, which are characterized by the existence of single Bragg peak and a complete loss of elastic channels [67, 71].

2.7 Non-equilibrium Relaxation: Aging Dynamics

The physics of systems in thermal equilibrium is well understood while the knowledge of the physics far from equilibrium is still incomplete. In general, one is interested in studying two fundamental classifications of systems out of equilibrium. The first one concerns non-equilibrium steady states with time independent probability distributions [72]. The system is driven out of equilibrium by an external force, field, or two different heat baths. Non-equilibrium steady states for systems of interacting vortices were discussed in detail in the last section and the results of our simulations will be interpreted in the next chapter. Another interesting subject is the study of the non-equilibrium relaxation which is the aim of this subsection. Understanding the properties and behavior of phenomena far from equilibrium may enable us to improve or invent better technologies and practical applications.

Many studies focus on the property of the microscopic structure and the response due to an external disturbance, such as magnetic field, temperature, and applied current. Above the melting temperature, the materials would be in thermal equilibrium and its structure would be liquid. In this phase, the structure of the material is inhomogeneous with high spatial symmetry. On the other hand, at low temperature the system forms

a crystalline structure with lower spatial symmetry. A number of experimental and theoretical investigations, which try to understand the phase transition between these two phases, have been performed. One type of the materials that shows liquid structure but is as hard as solid is obtained if one rapidly cools the system from the liquid phase at high temperature to below characteristic temperature, the glass transition ' T_g '. The liquid cannot equilibrate and crystallize over a short time and remains in a non-equilibrium metastable state, which is called the "glassy state". The dynamics of materials in the glassy state becomes extremely slow, by many orders of magnitude slower as their temperature is slightly reduced below the glass transition temperature [73]. When a material is brought out of equilibrium, it will try to relax over time in order to reach the equilibrium with its environment. The behavior or properties of the materials will change over time during the relaxation which takes extremely long, sometimes as long as the experimentalist can wait.

These non-equilibrium states are metastable, and the system attempts to reach equilibrium as time elapses. It was experimentally investigated by means of volume relaxation of glassy materials [74, 75, 76]. One can observe the transition from the liquid to the solid phase by monitoring the change of the specific volume as the temperature is reduced. The existence of the metastable state can be interpreted by the appearance of local minima of its free energy. For instance, above a critical temperature of a magnetic system, only a single minimum of the free energy can exist. If the system is rapidly quenched to below the critical temperature, the system is in the metastable state and tries to reach one of two equilibrium states. Fig. 2.8a and Fig. 2.8b show the plots of the free energy and the magnetization of the ferromagnetic system above and below the critical temperature, respectively. Here, the two new local minima represent two equivalent ordered states, i.e., all up spin or all down spin. If system is rapidly quenched to below critical temperature, the dynamics of the spin in the metastable state is extremely slow since there is a competition between these two states. The time that it will take the system to relax and be in one of these states can be extremely long, ranging from days to many years.

During the relaxation to the new equilibrium state, the property of the system such as the magnetization in the ferromagnet changes during an experimental observation time ' t ' after its preparation time ' s '. One may observe that the properties of the freshly prepared system, small waiting time ' s ', significantly change in comparison to the system which is prepared for longer time, i.e., the system displays aging property [77]. Aging is defined by the slow (non-exponential) relaxation from nonequilibrium to equilibrium such that $t_{micro} \ll s \ll t \ll t_{eq}$, where t_{micro} is a microscopic time scale and t_{eq} is the time to reach equilibrium. If the dynamics is too fast, one may observe the fast relaxation to equilibrium at small time, where t is of the order of t_{micro} . The aging property is found in many systems such as spin glasses, polymers, and colloids. In addition, aside from being theoretically interesting, aging phenomena are found to be technologically important. Some properties of glassy polymers, such as their small-strain mechanical properties, undergo remarkable changes which strongly depend on the waiting time ' s '. In the testing of such plastics, the aging time is as important as other parameters such as temperature, stress-level, and humidity. Better knowledge of the aging behavior of a material will help us to predict its long time behavior from short term tests. In general, the aging phenomena are well

characterized and investigated experimentally, theoretically, and numerically by means of two-time functions such as correlation and linear response

$$\begin{aligned} C(t, s) &= \langle \phi(t)\phi(s) \rangle \\ R(t, s) &= \left. \frac{\delta \langle \phi(t) \rangle}{\delta \langle h(s) \rangle} \right|_{h=0} \end{aligned}$$

where $\phi(t)$ denotes the time-dependent order-parameter, $h(s)$ is the time-dependent conjugate magnetic field, t is referred to as observation time and s as waiting time. The system undergoes aging if these correlation and response function depend on both t and s and not merely on the difference $\tau = t - s$. Hence, this breaking of time-translation invariance is the second important property of aging systems. This is crucial since the sample under study might be in the aging regime which depends strongly on its entire prehistory. This would be very extremely difficult if one wants to formulate a general theory for these systems. Due to this fact, the older system would respond slower and therefore remains highly correlated over the longer period of time $\tau \gg 0$. The last property of the aging is the presence of the dynamical scaling at long time limit. In the simple magnetic systems [78, 79], the two-time correlation functions are expected to display the dynamical scaling in the aging regime where $t, s \gg t_{micro}$ and $t - s \gg t_{micro}$, where t_{micro} is a microscopic time scale. One observes the dynamical scaling forms of

$$\begin{aligned} C(t, s) &= s^b f_C(t/s) \\ R(t, s) &= s^{-1-a} f_R(t/s) \end{aligned}$$

where a and b are non-equilibrium exponents. These dynamical scaling forms are found in systems at criticality [80, 81]. If $b = 0$, one obtains the simple or full aging. The ‘‘multiplicative aging’’ is obtained when $b \neq 0$. Sometimes, the scaling of these quantities slightly departs from a perfect t/s scaling, which is called ‘‘subaging’’ or ‘‘superaging’’. The t/s scaling is modified and can be approximated by τ/s^μ with $\mu < 1$ or $\mu > 1$, respectively. Furthermore, the behavior of the scaling functions f_C and f_R at long time regime can be approximated by

$$\begin{aligned} f_C(t/s) &\approx (t/s)^{-\lambda_C/z} \\ f_R(t/s) &\approx (t/s)^{-\lambda_R/z} \end{aligned}$$

where λ_C , λ_R , and z are the autocorrelation [82], autoresponse [83] and dynamic exponents [78], respectively. The values of b and λ_C/z will be determined in this work.

Since the dynamics of the glassy materials is extremely slow, the time window is long enough to allow one to investigate the aging property. The existence of glass phases of interacting magnetic flux lines in disordered type-II superconductors such as the Bragg glass, vortex glass, and Bose glass has been explained in the last section. There are few works reporting the investigation of aging dynamics in these systems. Recently, Du has experimentally demonstrated the existence of the aging phenomena by investigating the response of vortex lines to a current pulse [84]. The system with longer waiting time responds slower than the younger system, i.e., it takes longer time to reach the maximal voltage. Bustingorry *et al.* studied the relaxation dynamics using numerical simulation

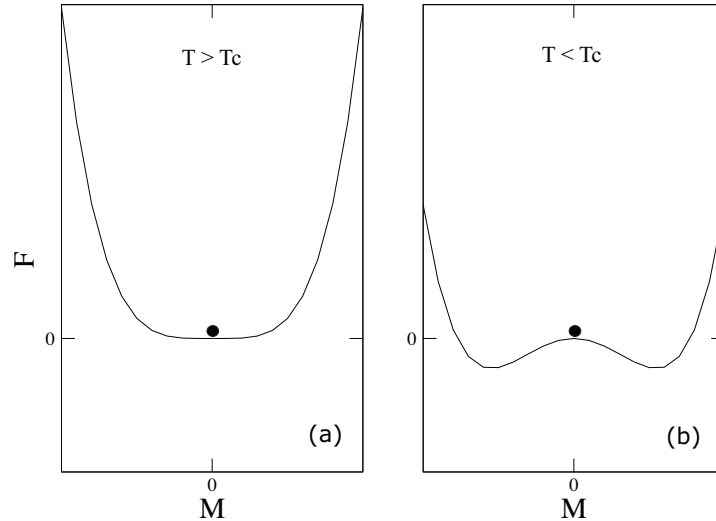


Figure 2.8: Free energy for a ferromagnetic system. The black dot represents an energy of a system (a) in thermal equilibrium $T > T_c$ and (b) in a metastable state after rapid quenching from above T_c . The system at high temperature (a) is in equilibrium and has the minimal free energy. (b) shows other two local minima corresponding to the two equivalent states. The system cannot relax rapidly to one of these due to the competition between these two equilibrium states. Its dynamics becomes extremely slow with infinite relaxation time.

of a London-Langevin model of interacting flux lines [31]. The aging property is found in quantities such as the two-time density-density correlation function, linear response, and mean-squared-displacement correlation function. This work will focus on the aging property of the correlation function for various temperature, defect density, vortex density, interaction range, and pinning strength. The method of investigation will be discussed in the next chapter.

2.8 Stochastic Model

Historically, physics or ‘natural philosophy’ research was carried out or described by means of theoretical, experimental, and philosophical investigations. Newton’s laws of motion are used to describe dynamical properties or temporal evolutions of a classical system, such as projectiles, oscillators, circuits, and charged particles. Fluctuations or uncertainty of interested observables in these classical systems are negligible or extremely small in comparison to their averages. When a system at small scale, atomic or molecular level, is of interest, the magnitude of these fluctuation and uncertainty are no longer negligible and can be comparable to the average of the observable. Newton’s equation of motion has to be revised in order to take into account the effect due to these uncertainties.

In a coarse-grained level, the temporal evolution of particle with the presence of these fluctuations is best described by a stochastic model such as Langevin equation which can explain Brownian motion.

A stochastic process is simply an 'ensemble' of a function of time and stochastic variable. Knowledge of both probability and stochastic methods are used to explain a physical description of natural phenomena. Some quantity of interest in many phenomena evolves in time in a very complex and irregular way such that it is impossible to compute this variation in detail. However, the average value of a composite system of such quantity may vary in a regular fashion, which can be explained by a simple rule. For example, the individual force exerted by each molecule of a gas on a piston is very rapid and is in unpredictable direction, but becomes smooth obeying Boyle's law, $p_i V_i = p_f V_f$, when integrated over a short period of time. Computing a temporal average of the quantity of interest is a very difficult task. Replacing it by an ensemble of functions or an ensemble average will turn it into a stochastic process which is much simpler.

In probability theory, the average value or the expectation value of the observable x is written as

$$\langle X \rangle = \sum_n x_n P(x_n)$$

where X is the random variable and $P(x_n)$ is the probability of finding the system with value x_n . In equilibrium statistical mechanics, this probability is based on the idea of a partition function which contains important information about the system. This partition is written as

$$Z = \sum_n e^{-E_n/k_b T}$$

where E_n is the Hamiltonian or energy of a system with configuration n , k_b the Boltzmann constant, and T the temperature. The probability of finding the system in any particular state is also determined by this partition function. Thus, the probability that the system is in equilibrium state n is given by

$$P_n^{eq} = e^{-E_n/k_b T} / Z.$$

In nature, equilibrium states are rarely possible to occur while non-equilibrium states are likely to occur in most observed phenomena. Generally, the probability distribution is time-independent and -dependent in equilibrium and non-equilibrium states, respectively. In the latter case, the stochastic process is utilized to define the temporal evolution of the probability distribution from specific configuration n to configuration m , as described by a master equation

$$\frac{\partial P_n(t)}{\partial t} = \sum_{n \neq m} [W_{m \rightarrow n} P_m(t) - W_{n \rightarrow m} P_n(t)]$$

where $P_n(t)$ is the probability of the system being in state n at time t , and $W_{n \rightarrow m}$ is the transition rate from configuration $n \rightarrow m$. In comparison to a continuity equation, the

master equation is a gain-loss equation for the probabilities of the separate states n . The first term is the gain of state n due to transitions from other states m , and the second term is the loss due to transitions from n into other states.

An equation explaining equilibrium states is a special case of this master equation. The probability distribution of the system in the infinite time limit must yield the equilibrium probability distribution, i.e., $P_n(t \rightarrow \infty) = P_n^{eq}$. The probability distribution of the system in thermal equilibrium is time-independent, $\frac{\partial P_n(t \rightarrow \infty)}{\partial t} = \frac{\partial P_n^{eq}}{\partial t} = 0$. Basically, this states the fact that in equilibrium the sum of all transitions per unit time into any state n must be balanced by the sum of all transition from n into other state m . Furthermore, the system in equilibrium satisfies the detailed balance condition where each pair of the sum in the master equation cancel out. The system out-of equilibrium can have a time-independent probability distribution if it is in a nonequilibrium steady state. However, it does not obey the detailed balance condition. Hence, for each pair n and m separately the transition for a system in equilibrium must balance:

$$W_{m \rightarrow n} P_m^{eq}(t) = W_{n \rightarrow m} P_n^{eq}(t)$$

From the detailed balance condition, we can choose any transition rate if it satisfies this condition. In the Metropolis Monte Carlo simulation, the transition rate for each attempt is chosen as

$$\begin{aligned} W_{m \rightarrow n} &= e^{-\Delta E/k_b T}, & \Delta E > 0 \\ &= 1, & \Delta E < 0. \end{aligned}$$

In the latter case, statistical mechanics teaches us that the system always seeks for lower energy configurations. For the first case, the system move with the transition rate proportional to the Gibbs factor in order to move to a higher energy configuration. The temperature also plays an important role in the transition rates, the transition rates become smaller as the temperature decreases and vice versa. In our system of interest, we update the system as following

- 1) Choose an initial vortex lattice site i
- 2) Choose a random site j
- 3) Calculate the change in energy $\Delta E = E_j - E_i$ and determine which transition rate is being used
- 4) Generate a random number r which is in the range $[0,1]$
- 5) If $r < e^{-\Delta E/k_b T}$, vortex lattice site j moves
- 6) Repeat step 1

In the non-equilibrium steady state there is an external driving force \mathbf{F} acting on vortex lines, which results in the net force acting on vortex lines in a direction of the driving force. This force does work of a magnitude $\Delta x F$ on the vortex line that move with a displacement of $\Delta x = x_j - x_i$. It biases the transition rates and favors the vortex line to move in such direction. The energy term in the third step above is modified to include the effect due to the driving force as $\Delta E' = \Delta E + \Delta x F$. In this work this Metropolis Monte Carlo simulation will be employed to simulate the driven vortex lines in the non-equilibrium steady states. In the next chapter, details of the simulation method (algorithm) will be discussed.

Chapter 3

Numerical Method/ Algorithm

3.1 The Model

As we have seen in the last section of the last chapter, in the Metropolis Monte Carlo algorithm the transition rates are proportional to the exponential of the difference in energy between the present and the new state $e^{-\Delta E'/k_b T}$, where $\Delta E' = \Delta E + \Delta x F$. In order to obtain the difference in energy and, hence, the transition rates, we consider a three-dimensional vortex system in the London limit in which the London penetration depth is much larger than the coherence length. We model the vortex motion by means of an elastic flux line free energy described in [34]. The system is composed of N flux lines in a sample of thickness L . This model free energy F_N , defined by their trajectories of the j th flux line and on the z th layer $\mathbf{r}_j(z)$, consists of three components, i.e., the elastic energy associated with the line tension, the repulsive vortex-vortex interaction potential, and a disorder-induced pinning potential

$$\begin{aligned} E &= \frac{1}{2} \tilde{\epsilon}_1 \sum_{j=1}^N \int_0^L dz \left| \frac{d\mathbf{r}_j(z)}{dz} \right|^2 \\ &+ \frac{1}{2} \sum_{i \neq j} \int_0^L V(|\mathbf{r}_i(z) - \mathbf{r}_j(z)|) dz \\ &+ \sum_{j=1}^{N_V} \int_0^L V_D(\mathbf{r}_j(z)) dz. \end{aligned}$$

The tilt modulus or line stiffness as a function of the energy scale $\epsilon_o = \left(\frac{\phi_0}{4\pi\lambda_{ab}}\right)^2$ is defined by $\tilde{\epsilon}_1 \approx \Gamma^{-2} \epsilon_o \ln\left(\frac{\lambda_{ab}}{\xi_{ab}}\right)$. The constant $\phi_0 = hc/2e$ is the magnetic flux quantum. The parameters $\lambda_{ab}, \xi_{ab}, \Gamma^{-2}$ are the in-plane London penetration depth, the coherence length, and the effective mass ratio M_{\perp}/M_z , respectively. This mass anisotropy is introduced in a layered superconductor model [50]. This expression for the elastic energy is valid in the limit where $\left|\frac{d\mathbf{r}_j(z)}{dz}\right|^2 \ll \Gamma^2$. The repulsive interaction energy between flux line elements in the same plane z is approximated as $V(|\mathbf{r}_i(z) - \mathbf{r}_j(z)|) = 2\epsilon_o K_0 \left(\frac{|\mathbf{r}_i(z) - \mathbf{r}_j(z)|}{\lambda_{ab}}\right)$, where K_0

is the modified Bessel function of zeroth order. This function diverges logarithmically as $r \rightarrow 0$ and decreases exponentially for $r \gg \lambda_{ab}$. These vortex interactions are cut off at the length of $L_y/2$ in all directions. We choose the system size in order that numerical artifacts due to this cut-off length are minimized. We model point and columnar pins through cylindrical square potential wells with $V_D(\mathbf{r}_j(z)) = \sum_{k=1}^{N_D} U_0 \Theta(b_o - |\mathbf{r}_j(z) - \mathbf{r}_k^{(p)}|)$ as our coarse-grained potential. Here, Θ denotes the Heaviside step function, $\mathbf{r}_k^{(p)}$ the spatial coordinates of the k th pinning center, and $U_o \approx \frac{\epsilon_0}{2} \ln \left| 1 + \left(\frac{b_o}{\sqrt{2}\xi_{ab}} \right)^2 \right|$ is the interpolated vortex binding energy per unit length with radius b_o . Finally, we add a work term due to the driving force $W = - \sum_{j=1}^N \int_0^L \mathbf{f}_L \cdot \mathbf{r}_j(z) dz$. We can now write this model free energy in the discrete form as

$$\begin{aligned}
E_i &= \frac{1}{2} \tilde{\epsilon}_1 \sum_{\langle j \rangle = i-1}^{i+1} \left| \frac{\mathbf{r}_\perp(i) - \mathbf{r}_\perp(j)}{b_0} \right|^2 \times b_0 \\
&+ \frac{1}{2} \sum_{j=1, i \neq j}^{N_V} V(|\mathbf{r}_i(z) - \mathbf{r}_j(z)|) \times b_0 \\
&+ \sum_{j=1}^{N_D} V_D(\mathbf{r}_j(z)) \times b_0 \\
&- \sum_{j=1}^{N_V} \mathbf{f}_L \cdot \mathbf{r}_j(z) \times b_0
\end{aligned}$$

where N_V is the number of flux lines within the radius of cut-off length and N_D is the number of effective defect elements. Simulation parameter values corresponding to typical parameters for YBCO shown in appendix D of [51] are calculated. The simulation length and energy are reported in units of the effective defect rod radius b_0 and interaction energy scale ϵ_0 in CGS units. Here the choice for parameters are temperature $T=10\text{K}$, pinning center radius and layer spacing $b_0 = \max\{c_0, \sqrt{2}\xi_{ab}\} = c_0 = 35\text{\AA}$, anisotropy $\Gamma^{-1} = 1/5$, average spacing between defects $d = 300\text{\AA} = 9.0b_0$, and since the temperature is very low, parameter values of in-plane penetration depth and coherence length are $\lambda_{ab} \approx \lambda_0 = 1200\text{\AA} = 35b_0$, the superconducting coherence length $\xi_{ab} \approx \xi_0 = 12.75\text{\AA} \approx 0.3b_0$. Then $\epsilon_0 = \left(\frac{\phi_0}{4\pi\lambda_{ab}} \right)^2 = \left(\frac{2.07 \times 10^{-7}}{4\pi \times 1200 \times 10^{-8}} \right)^2 \approx 1.9 \times 10^{-6}$. Notice that this parameter has the dimension of [Energy]/[Length] according to [51].

The energy scale in the first term is therefore $\tilde{\epsilon}_1 \approx \Gamma^{-2} \epsilon_0 \ln\left(\frac{\lambda_{ab}}{\xi_{ab}}\right) \approx \frac{M_\perp}{M_z} \epsilon_0 \ln\left(\frac{\lambda_{ab}}{\xi_{ab}}\right) \approx \frac{1}{25} \ln\left(\frac{1200 \times 10^{-8}}{12.75 \times 10^{-8}}\right) \epsilon_0 \approx 0.18\epsilon_0$. The interaction energy in the second term is in the form $V(|\mathbf{r}_i(z) - \mathbf{r}_j(z)|) = 2\epsilon_0 K_0 \left(\frac{|\mathbf{r}_i(z) - \mathbf{r}_j(z)|}{\lambda_{ab}} \right)$. The pinning potential in the last term is given by the interpolated equation $V_D = U_0 = \frac{\epsilon_0}{2} \ln \left| 1 + \left(\frac{c_0}{\sqrt{2}\xi_{ab}} \right)^2 \right| = \frac{\epsilon_0}{2} \ln \left| 1 + \left(\frac{35 \times 10^{-8}}{\sqrt{2} \times 12.75 \times 10^{-8}} \right)^2 \right| = 0.7809\epsilon_0$. It is clear that the model free energy has a unit of $\epsilon_0 b_0$. This discrete form of

the free energy can be further simplified in these units as

$$\begin{aligned}
E_i &= 0.09 \frac{\epsilon_0}{b_0} \sum_{\langle j \rangle = i-1}^{i+1} |\mathbf{r}_\perp(i) - \mathbf{r}_\perp(j)|^2 \\
&+ \epsilon_0 b_0 \sum_{j=1, i \neq j}^{N_V} K_0 \left(\frac{|\mathbf{r}_i(z) - \mathbf{r}_j(z)|}{35b_0} \right) \\
&+ N_D \times 0.78 \epsilon_0 b_0 \\
&- \sum_{j=1}^{N_V} \mathbf{f}_L \cdot \mathbf{r}_j(z) \times b_0.
\end{aligned}$$

Since $|\mathbf{r}_\perp(i) - \mathbf{r}_\perp(j)|^2$ in the first term has units of b_0^2 , therefore, the first term has the unit of $\epsilon_0 b_0$. The last quantity needed to be discussed here is the exponent parameter $\frac{\Delta E}{k_B T}$ using to update the state of the system via $e^{-\frac{\Delta E}{k_B T}}$. This value has to be dimensionless. Thus $\frac{\epsilon_0 b_0}{k_B T}$ gives a dimensionless ratio of $\frac{1.9 \times 10^{-6} \times 35 \times 10^{-8}}{1.38 \times 10^{-16}} \approx 4800$. This means $e^{-\frac{\Delta E}{k_B T}} \approx e^{-4800 \frac{\Delta E}{T}}$ where ΔE and T are the difference in free energy of the initial and final state and temperature in the simulation, respectively. The temperature of the sample can also be written in the unit of $\epsilon_0 b_0 = 6.59 \times 10^{-13}$. For example, at $T=10$ we have $\frac{k_B T}{\epsilon_0 b_0} = \frac{1.38 \times 10^{-16} \times 10}{6.59 \times 10^{-13}} = 0.002$ or $k_B T = 0.002 \epsilon_0 b_0$. It is clearly seen that the thermal energy is negligible in comparison to the elastic energy of the flux line and, therefore, in the absence of a drive the system is deep in the glassy regime.

Since this is a numerical simulation, each parameter value can be varied in order to study either the direct or indirect result due to the change of that parameter value. For example, when we increase the value of temperature or reduce the range of penetration length, this would indirectly reduce the stiffness of the flux lines, i.e. the lower the temperature, the stiffer the flux lines, or the shorter the penetration length, the softer the flux lines. We also can change values of each parameter at the same time and observe the difference in dynamical properties. This depends on our choices.

However, there is an artifact due to the limitation of each movement of the flux line in our simulation. This can be seen in the I-V curves in the form of the saturation of the curve at high driving force. For each move in the simulation, a displacement for the next step is randomly chosen from the interval between -0.5 and 0.5. The acceptance rate for each movement depends on the driving force. The larger the driving force, the larger the displacement that each step can take. However, the maximal displacement is reached when the driving force is increased to a finite value. It cannot be larger at higher driving force than this, which results in the saturation of the velocity in the I-V curve. We choose to present the data in the critical regime where the I-V curve is not yet saturated.

3.2 Quantities of Interest

3.2.1 Characterization of Non-Equilibrium Steady States

Velocity

In order to determine in which regime or non-equilibrium steady state this system of driven flux lines is, we can simply look at the I-V or the force-velocity curve. In experiments, flux lines are subjected to a Lorentz force in the direction transverse to the direction of an external current. In the simulation, flux lines tend to move in the direction of the driving force. The mean velocity of flux creep or flux flow is determined by the average of total displacement of each center of mass of flux lines over a certain number of Monte Carlo steps.

$$v_{cm} = \frac{1}{N_v} \sum_{i=1}^{N_v} \frac{r_{cm_i}(t + \tau) - r_{cm_i}(t)}{\tau},$$

where N_v is the number of vortex lines, r_{cm_i} is the center of mass of the i^{th} vortex line, and τ is set to 30 MCS. Experimentally, the average velocity of the moving vortices is directly related to the voltage drop across the sample from $E = (B \times v)/c$. The driving force arises from the fact that there is Lorentz force acting on the vortices when there is an external current applied to the sample, i.e., $f = (J \times \Phi_0)/c$.

After obtaining the velocity we can construct the force-velocity or the I-V curve and then determine the value of critical driving force in each system. As mentioned in the last chapter, the scaling behavior of the nonlinear I-V characteristics can be used to identify the transition of a vortex glass to vortex liquid in type-II superconductors. It is also used to identify the melting temperature in the peak effect, which shows a peak in critical currents as function of magnetic field (or vortex density).

Radius of Gyration

The investigation of three-dimensional structures of moving flux lines in non-equilibrium steady states is one of the main goals of this work. Hence, we are interested in a quantity which reflect fluctuations of flux lines. There are some standard quantities used to characterize the dynamical properties of the vortex system such as the roughness or radius of gyration, the dynamic wandering, and the mean square displacement of flux lines. The dynamic wandering measures a correlation between the displacement of the flux line elements in each plane and the bottom plane. The mean square displacement of flux lines measures the total displacement of center of mass of flux lines from the beginning of the simulation. These quantities can also be generalized and used for system that the quantity of interests strongly depend on the time needed to prepare the system, waiting time s . These will be discussed later.

The radius of gyration is the root mean square displacement of flux line elements from its center of mass. We use this to directly investigate the effect of the different defect

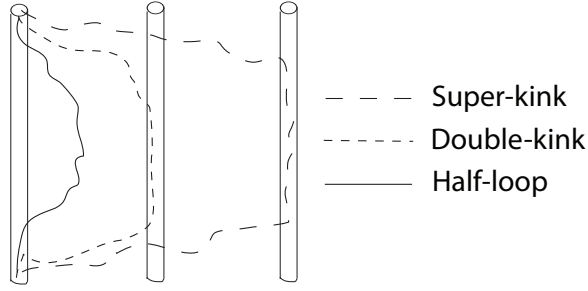


Figure 3.1: Thermally activated half-loop, double-kink, and super-kink.

types on the shape of flux lines. The expression for this quantity is

$$r_g = \left(\frac{1}{N_v L} \sum_{i,z} \langle [x_{iz} - x_{z_{cm}}]^2 \rangle \right)^{\frac{1}{2}},$$

where x_{iz} is the i^{th} element of line z , $x_{z_{cm}}$ is the center of mass of line z , $x_{iz} - x_{z_{cm}}$ is the displacement of the iz line segment, and L is the number of layers of vortex lines. In the case of a system with columnar defects, we use the maximal displacement in each flux line to determine the number of half-loop or double-kink excitations. If the maximal displacement in each flux line is approximately equal or greater than the average distance between defects, this line is considered to have a double-kink excitation. In contrast, for a maximal displacement greater than the size of defect but less than the average distance between defects, we consider them as half-loop excitations.

Static Structure Factor

Another quantity which reveals a symmetry or structure of materials in equilibrium and out of equilibrium is the static structure factor. Periodic arrangements of atoms or molecules in a solid are more ordered but have lower symmetry than system with random arrangements such as fluids or gases. Most systems result in the highly-ordered, low-symmetry crystalline solid as they are cooled to the lowest temperatures. Experimentally, scanning force and tunneling microscopes are some of the most practical tools used to obtain direct image near the surface of materials. In order to probe bulk structure of materials at the atomic scale, it is more appropriate to use a special technique such as scattering of neutrons, electrons, or photons. For instance, the elementary scattering theory such as Bragg's law shows that an incident wave on planes of crystalline or non-crystalline structure will be diffracted or reflected off the planes. The constructive and destructive interference of the wave scattered from different atoms and different planes will form different patterns on the screen, which depends on internal structures of each material. From scattering theory, the differential cross-section, which is proportional to the intensity of the scattered wave, can be expressed as a term of an extensive quantity called structure function

$$\frac{d^2\sigma}{d\Omega} \propto I(\mathbf{q}),$$

where

$$\begin{aligned} I(\mathbf{q}) &= \int e^{-i\mathbf{q}\cdot(\mathbf{x}_1-\mathbf{x}_2)} \langle n(\mathbf{x}_1)n(\mathbf{x}_2) \rangle d^d x_1 d^d x_2 \\ &= \langle n(\mathbf{q})n(-\mathbf{q}) \rangle \end{aligned}$$

is simply a Fourier transform of the two-point density-density correlation function and

$$n(\mathbf{q}) = \int d^d x e^{-i\mathbf{q}\cdot\mathbf{x}} n(\mathbf{x}) = \sum_{\alpha} e^{-i\mathbf{q}\cdot\mathbf{x}_{\alpha}}$$

is the Fourier transform of the local density $n(\mathbf{x})$. The intensive version of this function obtained by dividing the above quantity by a number of particles or its volume is called the structure factor

$$S(\mathbf{q}) = V^{-1}I(\mathbf{q}), \text{ or } S(\mathbf{q}) = N^{-1}I(\mathbf{q})$$

In our study we could expect that an ordered or quasi-ordered vortex structure such as the Abrikosov vortex lattice or Bragg glass would form a periodic pattern of this static structure factor peaks. On the other hand, a disordered structure such as the vortex glass or vortex liquid would result only a single peak.

Voltage Noise Spectrum

As we know that disorder has a direct effect on vortex motion, probing the nature of disorder is one of the main research in superconductivity. The effect of disorder on the dynamics of driven vortices has been studied by means of the voltage noise power spectrum which is defined by

$$S(\omega) = \left| \int v(t) e^{i\omega t} dt \right|^2.$$

It directly reflects periodicity of the average velocity moving vortex lattice. Voltage noise due to a moving vortex lattice can be interpreted in the form of a broadband noise or narrow band noise. It has been shown that in the presence of weak pinning strength, point defects, and low driving force, vortices are in the plastic regime and characterized by a broadband noise signal proportional to a power law $1/\omega^{\alpha}$ [85]. The narrow band noise is expected to exist as long as the moving vortices remains its long-range or quasi long-range order such as the moving Abrikosov vortex lattice or moving Bragg glass. Bullard and Das have performed intensive investigations on this quantity in driven vortex systems in the presence of weak point and columnar defects [33]. They have proved the coincidence of the narrow band noise and the washboard frequency which is defined by $\omega = 2\pi\langle v \rangle/a_0$. Here $\langle v \rangle$ is the average velocity, and a_0 is the intervortex distance. The reason for the existence of this washboard noise is that quenched disorder in the system occasionally trapped some vortices, resulting in 'stick-slip' motion and, hence, a periodically varying average overall velocity of the moving Bragg glass.

The existence of broadband noise and appearance of the washboard frequency has been experimentally demonstrated [86, 87, 88, 89] and numerically investigated both in two-dimensional [90, 91, 92] and three-dimensional systems [33, 93]. The magnitude of the broadband noise strongly depends on the applied current and the external field [94]. It is shown that the broadband noise in the ‘peak regime’, where the peak effect occurs, appears with the onset of the motion of vortices. The noise power increases to its maximum slightly above the critical current. The noise power decreases at large applied current since the rapidly moving vortices are much less noisy. It was also suggested that the magnitude of the broadband noise would reach its maximum in the regime of plastic flow. For three-dimensional simulations, the washboard frequency is reported in the system of moving Bragg glass in the presence of weak pinning disorder. The voltage noise was also used to study the transition from the moving disordered phase, such as the moving vortex glass, to the moving ordered phase, such as moving Bragg glass or moving Abrikosov vortex lattice. The evolution of the voltage noise from the $1/\omega^\alpha$ broadband noise to the washboard noise is the signature of such a phase transition. The existence of the washboard noise in the system consisting of strong point and columnar disorder is still unclear and will be one of our main investigation in this work.

It was recently shown by Pautrat and Scola [95] that there exists narrow band noise in the peak effect regime, near the critical temperature T_c , where a long range temporal correlations of vortices exist. The characteristic frequency found in this experiment is observed to be different from the washboard frequency. The associated length scale was then calculated and found to match with the width of the sample rather than the intervortex distance which is much larger in orders of magnitude. This brings our attention to one of our results which shows that the associated length scale is found to be as small as the width of the pinning center rather than the intervortex distance or the width of the sample. The detailed investigation will be discussed in the next chapter.

3.2.2 Aging Dynamics

The two-time density-density correlation function, which is used in the simulation, is defined and explained in this section.

Two-Time Density-Density Correlation Function

Interesting properties for systems out of equilibrium, which strongly depend on time, can be revealed if one considers the two-time autocorrelation function at times t and s . In the system of interacting vortices, aging phenomena are investigated by means of the local two-time density-density correlation function at site i at different times

$$C(t, s) = [\langle \rho_i(t) \rho_i(s) \rangle]$$

where $\langle \dots \rangle$ is the average over local sites i and $[\dots]$ represents a disorder average over different defect distributions. This form of the correlation function will be used for this work. This quantity measures the correlation of the particle at site i for different times.

As $t \rightarrow \infty$, particles will move independently and lose their correlation. Hence, this autocorrelation function will decay to zero in the long time limit. For a glassy system, the rate at which this correlation decays to zero depends strongly on the total time elapsed ' t ' and the waiting time ' s ', i.e., the system ages.

Chapter 4

Characterization of Nonequilibrium Steady States

The results in this section are from simulations in a system of $[x, y, z] = [\frac{2}{\sqrt{3}} \times 10\lambda, 10\lambda, 20b_o]$ with fully periodic boundary conditions at temperature $T=10$ K or $T=0.002 \epsilon_0 b_0$. We choose the system's $L_x : L_y$ aspect ratio to be $2 : \sqrt{3}$ to accommodate an even square number of vortices to fit in the system while arranged in the triangular lattice [96]. We have tested that the penetration length of $\lambda = 35b_o$ and cut-off interaction range of 5λ in this system size had no effect on the equilibrium vortex configuration due to the sharp cut-off interaction range. In the absence of a driving force and pinning sites, square numbers of randomly placed vortices were observed to arrange into six-fold or hexagonal lattice after the system equilibrated. The average spacing of $9b_o$ between defects gives a total number of 1710 lines of columnar defects. Each columnar defect contains 20 point defect elements thus a total of 1710×20 point defect elements in the system.

The main point of investigation in this work is to fully characterize the dynamical properties of the driven vortex lines in the presence of strong pinning centers at low temperatures and fields. Bullard and Das [96] have studied the system in the regime where the pinning strength is weak in comparison to the parameter ϵ_0 of this work. They concentrated on the effects of columnar and point defects on the voltage power spectrum in the driven non-equilibrium steady states. In addition, we focus on the spatial structures of driven flux lines in various regimes including pinned, critical, and flowing/steady states. In order to be able to observe the effect due to these pinning sites, the maximal displacement for each random move is $\Delta = 0.25b_0$. This is to guarantee that the flux lines will not move too fast and skip the pinning sites. We studied the effect of maximal displacement Δ on the dynamics of vortices and found that if Δ was too small, systems would be trapped in metastable states and required a much longer simulation time to reach equilibrium. We also studied the effect of different initial vortex configurations on the dynamics of moving vortices. When a small drive was applied to the system with randomly placed columnar defects, we found that randomly placed vortices ended up in the pinned Bose glass phase while the periodically prearranged vortex lattice formed the partially pinned Bose glass phase. In both cases, vortices ended up in randomly placed configurations since the strong pinning centers tear apart any regular lattice. This was also true for the

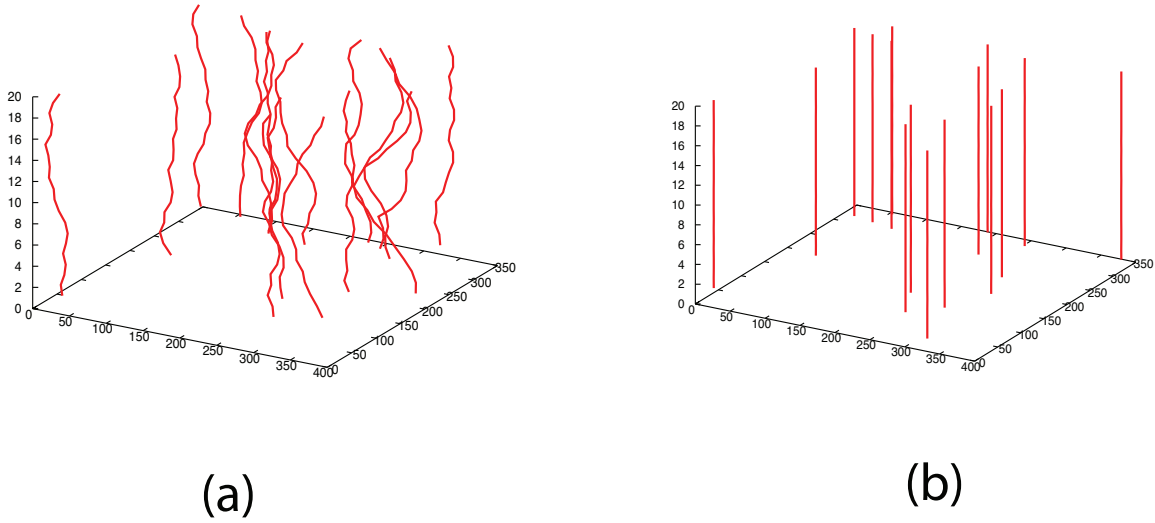


Figure 4.1: At low drives, randomly placed vortices form the (a) pinned Vortex glass and (b) pinned Bose glass phases in the systems with randomly placed point and columnar defects, respectively. Much longer simulation time is needed in order to get the systems out of these metastable states and reach true thermal equilibrium. The figures show only the flux lines but not the defects.

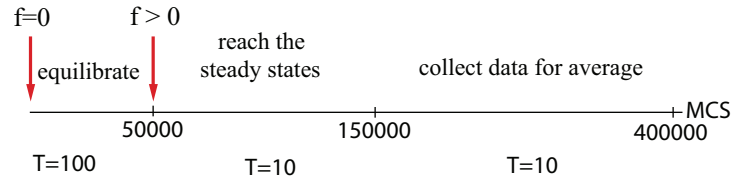


Figure 4.2: The time line for the simulation. First, equilibrate the system at $T = 100$ for 50000 MCS. The temperature is suddenly decreased to $T = 10$ and the system is driven to reach the steady states for the next 100000 MCS. Finally, quantities of interest are obtained every 30 MCS for the rest of 250000 MCS.

systems with randomly placed point defects, randomly placed vortices ended up in the disordered vortex glass at the end of the simulation. Much higher fields are required in order to have the interaction potential overcome the pinning potential and cause vortices to form the equilibrium six-fold lattice configuration.

In our work, we randomly place the vortex lines in the system at an initial high temperature $T=100$ and let them equilibrate for 50000 MCS in the absence of driving force. After thus annealing the flux line system, the temperature is suddenly quenched to low temperature $T=10$. At this time, the external drive is then applied for another 100000 MCS to reach its steady state. Quantities of interest are then collected every 30 MCS for the next 250000 MCS. Quantities of interest are averaged over a number of vortex lines and defect distributions. For all types of defect distributions, we have tested that flux lines with this annealing method yielded the pinned states. Annealing yields the highest critical current in our simulation. In comparison to the experimental result, we calculate the fields for each number of vortices we use in the simulation. Systems with 16,

36, 64, and 100 lines of vortices in the simulation are comparable to systems with internal magnetic fields of 0.019 T, 0.043 T, 0.076 T, and 0.119 T, respectively.

4.1 Current-Voltage (I-V) Characteristics

Various phases of moving vortices can be characterized or identified by means of the current-voltage characteristics [53, 97, 98]. The sample follows Ohm's law when it is in the normal state but behaves quite different when it is in the superconducting state. It was shown that the driven vortices would move with an average velocity v and give rise to a voltage drop across the sample V . By investigating the I-V curves, three different dynamics elastic, plastic, and liquid phases of moving vortices were suggested in dc transport experiment [55, 99]. In a vortex glass [22], the nonlinear relationship between the current density J_c and the voltage response V is expected to be

$$V \sim e^{-(J_c/J)^\mu}, \mu \leq 1.$$

This nonlinear form of the I-V curve is also found in the Bose glass with coefficient μ of 1/3 [34]. We observe nonlinear I-V curves in the critical regime of all our results. However, poor statistics does not allow us to measure the exponent μ .

In the regimes investigated, we first study the effect on the critical currents due to various spatial configurations of defects in the sample. It is expected that the critical currents in systems with correlated disorder should be higher than in those with uncorrelated disorder. The strength and number of point defect elements for each configuration is the same, i.e. the same defect density. We choose to present our data in the regime where the I-V curve is rising just above the critical depinning threshold. Far above the critical current, all I-V curves start to saturate and merge as a consequence of a numerical artifact due to the limitation of each movement. As mentioned at the end of section 3.1, the acceptance rate for each move depends on the driving force. Larger moves are accepted for increasing driving force. However, they reach the maximal displacement which is set to 0.25 in the simulation when the driving force reaches a finite value. This can be observed as the saturation of the I-V curve at high drive. The saturation of the I-V curve at high drives is also reported in the numerical simulation by Bullard [33].

The first part of this work comprises the investigation of defect configuration on the I-V curves. There are six defect configurations used in the simulation: a triangular and rectangular arrangement of columnar defects, randomly placed splayed columnar defects, a mixture of point and randomly placed columnar defects, and randomly placed point defects. In the case of columnar defects, defect elements in each layer are arranged on top of each other which results in highly correlated defects with the highest critical currents. For the system with mixed defects, the ratio between the point defect elements and randomly placed columnar defect elements is 1:1. The splayed defects are created by placing columnar defects at random positions and tilting them slightly in random directions. In our simulations we tilt them such that the displacement between the top and the bottom layer for each defect is about $5 b_o$. A larger value of the displacement would result in a randomly placed point defect configuration and therefore, lower critical

currents. With the same defect density, the difference in the value of critical currents for each I-V curve should be a direct result due to the difference in the spatial configuration of defects. Small cross sections for each type of defect configuration are shown in Fig. 4.3.

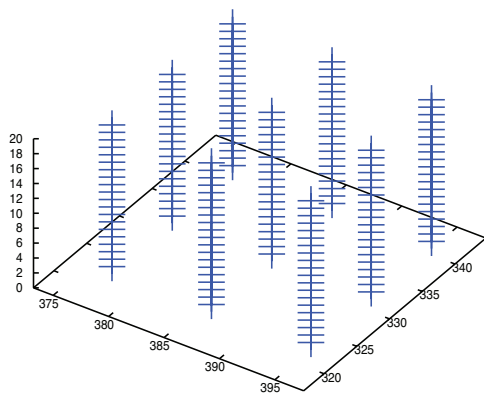
Characteristic I-V curves for systems with different types of defect distributions are shown in Fig. 4.4. It is shown that critical currents for systems with triangular and rectangular arrangement of columnar defects are higher than those with randomly placed columnar defects, randomly placed splayed columnar defects, a mixture of point and randomly placed columnar defects, and randomly placed point defects, respectively. This is in good agreement with the experimental and numerical work [33, 47], which clearly demonstrate that the columnar defects are more effective and give larger critical current density J_c than a system with point defects. At low and intermediate drive, flux lines are trapped in a metastable state and spend most of the time inside the center of the pinning sites. Flux lines wandering between nearby defects may occur due to the thermally activated jumps. The average velocity is extremely small and can be explained by the theory of the flux creep [100]. Far above the critical currents flux lines flow freely. In the case of a system with randomly placed point defects, the pinning force density does not add coherently over the length of the vortex. This will promote the wandering of flux lines in the sample. Note that the real pinning strength for a columnar defect is stronger than for a point defect by approximately an order of magnitude. In our simulations, the pinning strength of all defect configurations is set to be the same to allow for more direct comparisons. In addition, systems with lower vortex densities should have higher critical currents due to a weaker interaction between vortices [101, 102]. As the external field is decreasing, the pinning potential energy overcomes the vortex interaction energy and leads to the pinned state. Fig. 4.5 and Fig. 4.7 show I-V curves obtained from systems with randomly placed columnar and point defects for increasing vortex density. The critical currents in systems with point defects are smaller than those with correlated columnar defects. As the number of flux lines increases, the critical current becomes smaller for both types of defect distributions. Notice that the largest fluctuation in the velocity for each I-V curve is observed just above the critical current. This is supported by the largest value of the standard deviation in velocity in the critical regime. For various vortex densities, at approximately equal velocity, the fluctuations tend to be larger in the system with lower density of flux lines. This can be seen obviously in the I-V curves for systems with point defects. This indicates that the competition between vortex interactions, elastic energy, thermal fluctuations, pinning potentials is extremely prominent in this regime, regardless of the defect configurations. These results are in a good agreement with the results by Bullard [33]. However, we do not observe the crossing of the I-V curves for different vortex density, which is explained as the numerical artifact local update in the Metropolis algorithm. Larger local moves are suppressed by the vortex interaction for increasing vortex density, hence we obtain a smaller velocity and slope of the I-V curve.

In order to estimate the critical depinning threshold for each curve, we amplify the I-V curves in the low velocity regime and perform a linear extrapolation for each I-V curve until it crosses the x -axis which corresponds to the driving force. The linear extrapolation is performed such that the line has the greatest slope before dropping to zero value. Fig. 4.6 (left figure) and Fig. 4.8 (left figure) show the amplification of the I-V curves of

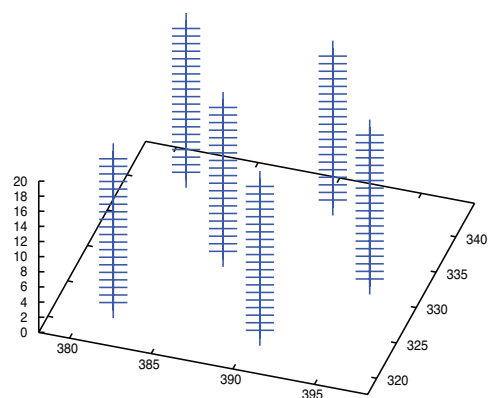
Table 4.1: Critical depinning threshold for various vortex density

Vortex density (lines)	Critical depinning force (ϵ_0/b_0)	
	Point defect	Columnar defect
16	1.38	2.44
36	1.35	2.36
64	1.33	2.28
100	1.30	2.2

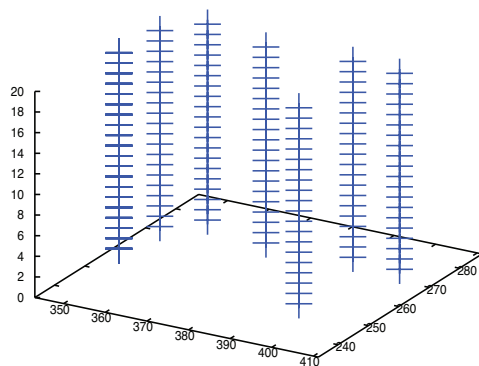
the systems with randomly placed columnar defects and point defects in the low velocity regime. Critical currents for systems with 16, 36, 64, and 100 lines with randomly placed columnar and point defects are thus determined as 2.44, 2.36, 2.28, 2.20 and 1.38, 1.35, 1.33, 1.30, respectively. This is summarized in Table 4.1. Critical currents and number of vortex lines in the system with randomly placed columnar and point defects are plotted in Fig. 4.6 (right figure) and Fig. 4.8 (right figure), respectively. This same tendency of decreasing critical current for increasing vortex density is also found in [96].



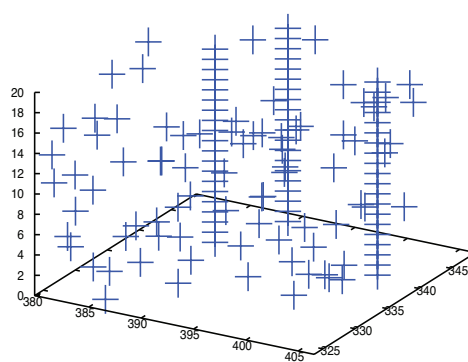
Rectangular



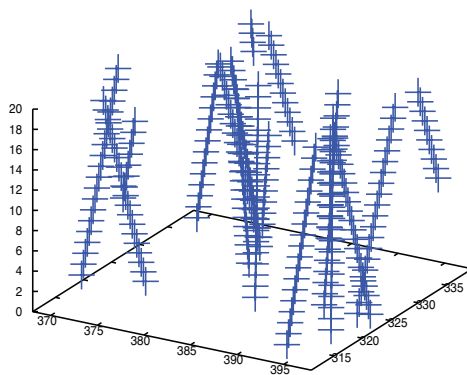
Hexagonal



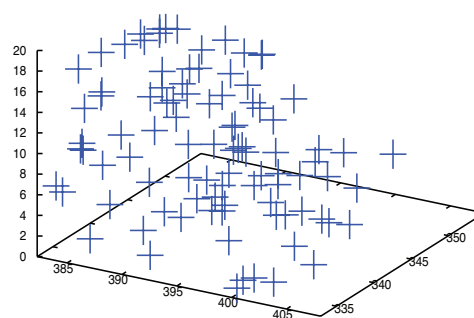
Random Col.



Mixed



Splayed



Point

Figure 4.3: Small cross sections of systems with rectangularly, hexagonally, and randomly placed columnar defects, a mixed system with both randomly placed point and columnar defects, and systems with randomly placed splayed linear defects, and point defects.

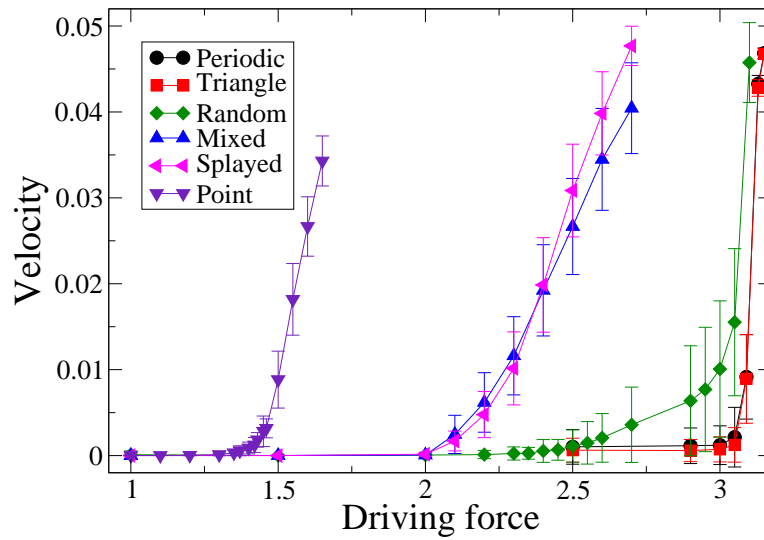


Figure 4.4: I-V curves for the systems with different types of defects. Each system contains 16 flux lines. The system with rectangularly (circle) and triangularly (square) arranged columnar defects have higher critical currents than the systems with randomly placed columnar defects (diamond), splayed columnar defects (left triangle), mixture between points and columnar defects (up triangle), and point defects (down triangle), respectively. This confirms that systems with the correlated defects yield higher critical currents. Please note that the pinning strength for different defect configuration is set to be the same, $0.78 \epsilon_0 b_0$, while the real pinning strength for point defects is smaller by approximately an order of magnitude. Results are obtained from the average of 50 defect distributions.

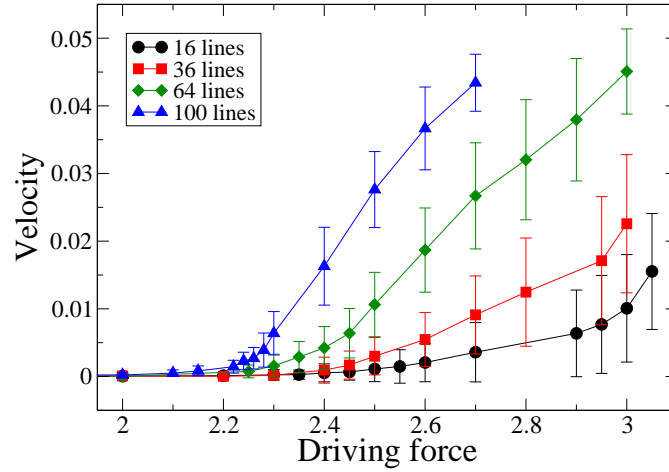


Figure 4.5: I-V curves for systems with randomly placed columnar defects, for various vortex densities. The system with 16 flux lines (circle) has a higher critical current than the systems with 36 lines (square), 64 lines (diamond), and 100 lines (triangle up), respectively. Systems with weaker vortex interactions have higher critical currents. As the external field is decreasing, the pinning potential energy overcomes the vortex interaction energy and leads to the pinned states. Results are obtained from the average of 50 defect distributions.

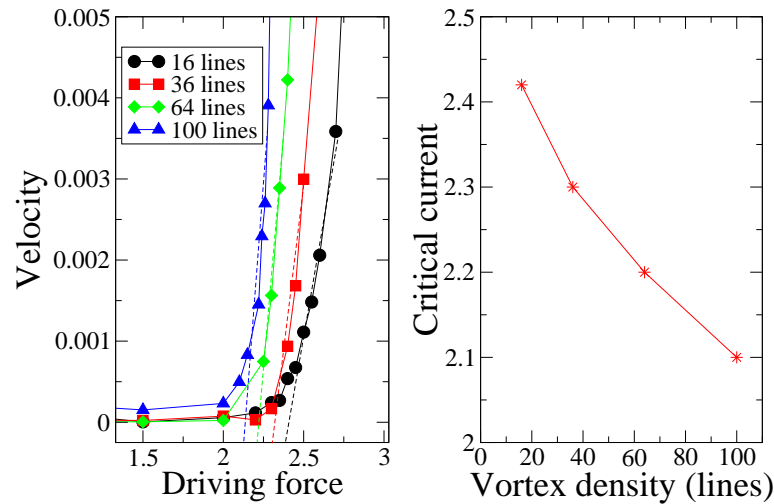


Figure 4.6: (Left figure) I-V curves for systems with randomly placed columnar defects, for various vortex densities, at small velocity. Extrapolation of data is done to achieve the critical currents for each curve. We estimate the depinning current for each curve by extrapolating the curve to the x-intercept. (Right figure) The systems with 16 lines (circle), 36 lines (square), 64 lines (diamond), and 100 lines (triangle up) yield critical current values of 2.44, 2.36, 2.28, and 2.2, respectively. This clearly shows the decrease of the critical depinning currents as the vortex densities increase.

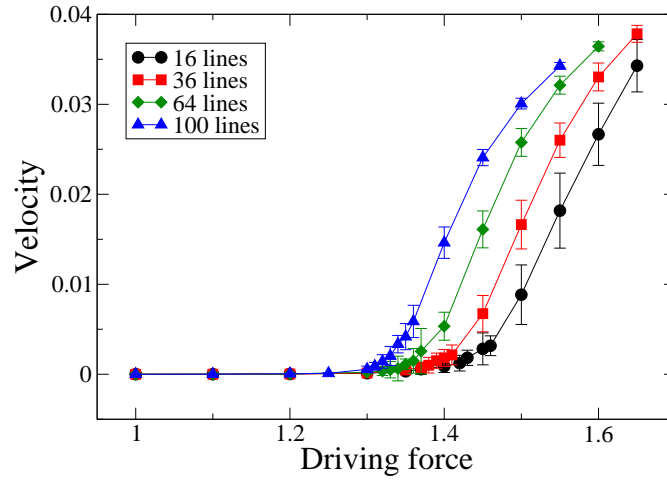


Figure 4.7: Critical currents for systems with point defects with different vortex densities. The system with 16 lines (circle) has a higher critical currents than systems with 36 lines (square), 64 lines (diamond), 100 lines (triangle up), respectively. Similar to the systems with randomly placed columnar defects, this shows that systems with weaker vortex interaction have higher critical currents. Results are obtained from the average of 50 defect distributions.

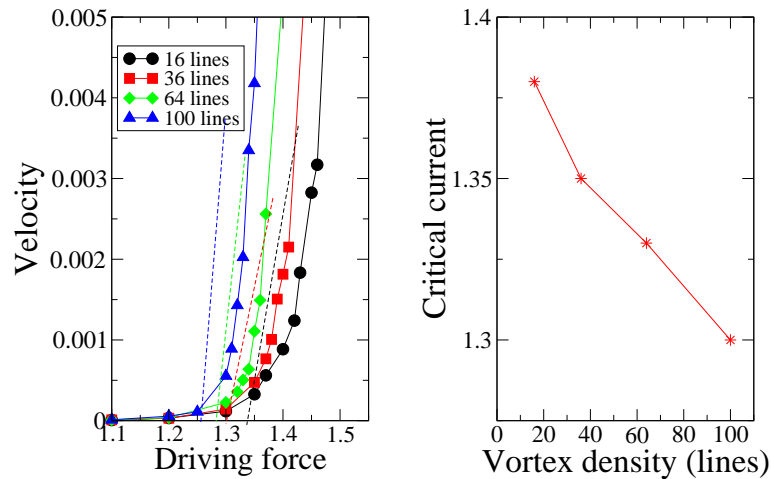


Figure 4.8: I-V curves for systems with point defects, for different vortex densities, at small velocity. A linear extrapolation is performed for each I-V curve to obtain a critical depinning force. This linear extrapolation creates a line which has the greatest slope and is parallel to each I-V curve. Systems of 16 lines (circle), 36 lines (square), 64 lines (diamond), and 100 lines (triangle up) have critical currents of 1.38, 1.35, 1.33, and 1.30, respectively. This clearly demonstrates that systems with weaker vortex interaction or larger lattice spacing, have higher critical currents. Results are obtained from the average of 50 defect distributions.

4.2 Radius of Gyration

Here we measure the root mean square displacement or the radius of gyration near the critical current. Knowing the behavior of the radius of gyration allows us to obtain more information about the shape of the moving flux lines in three-dimensional system. This quantity is not available for a two-dimensional system. The radius of gyration represents the spatial fluctuations of the flux line from its center of mass. We omitted results in the regime of low driving forces since the dynamics is extremely slow. The results in the regime of large driving forces are omitted due to the unphysical limitation for each movement as mentioned in the previous section.

4.2.1 Columnar Defects

Here we present our results first and then compare with the results by Bullard [33, 103]. The plots of the average radius of gyration versus the driving force in the system of 16, 36, 64, and 100 flux lines with randomly placed columnar defects are shown in Fig. 4.9, Fig. 4.10, and Fig. 4.11. For all investigated vortex densities, the radius of gyration in the direction of the drive increases as the drive increases. At low drives, we observe the Bose glass phase as predicted by Ref.[34]. This can be seen by the completely localized vortex lines inside the columnar defects as shown in Fig. 4.12a. The average radius of gyration of the Bose glass would be smaller than the radius of the columnar defect, which is set to 1 in the simulation. Since the pinning force of a columnar defect is very large and overcomes the repulsive vortex interaction, flux lines become localized at different locations resulting in the disordered phase. At intermediate drives close to the critical regime, some flux lines are delocalized and move along the direction of the drive. This coexistence between moving flux lines and localized Bose glass is shown in Fig. 4.12b. It is expected that a small average radius of gyration would occur due to these moving flux lines. At high drives, all flux lines are moving and hence give a larger radius of gyration, see Fig. 4.12c. The radius of gyration increases with the number of vortices and saturates at 64 and 100 lines. The saturation of the radius of gyration indicates the stronger vortex interaction starts to dominate the dynamics at high drives.

At low vortex density, the average spacing between each flux line is larger than the vortex interaction range (penetration length) of $35b_0$. The vortex interaction exponentially falls off at large distances and varies logarithmically at small distances. It would be relatively small when the distance is larger than the interaction range. Along the x-axis, the system of 16 and 36 lines have the average spacing between each flux line of $101b_0$ and $67b_0$. They are measured to be $87.5b_0$ and $58.3b_0$ along the y-axis. At these densities, it is clearly seen that flux lines are weakly interacting and tend to move independently while they are interacting with the defects. The repulsive vortex interactions from the flux line's neighbors are not strong enough to repel each other in order to form the vortex lattice. Defects dominate the dynamics of the moving flux lines in this regime, which promote wandering of the flux lines and hence a larger radius of gyration.

For the denser system of 64 and 100 lines, the average spacing between each flux

line becomes smaller, i.e., $50.5b_0$ and $40.4b_0$ along the x-axis and $43.7b_0$ and $35b_0$ along the y-axis. The vortex interaction becomes significant at these densities. The radius of gyration increases in the intermediate drive regime and tends to saturate at high drive. The driving force averages over times and smoothens the pinning potential as it increases. Flux lines are stiffer as the vortex interaction becomes stronger.

A similar tendency is also observed in the I-V curves from the previous section. The I-V curves for the systems with 16 and 36 lines tend to keep increasing for increasing drive, with concave up shape. On the other hand, the I-V curves for the systems with 64 and 100 lines increase at intermediate drive but reduce in slope at higher drive. We then make the rough conclusion from the similarity of the behavior of the I-V curve and the radius of gyration that the I-V curve can reflect the shape of the vortex line. If the I-V curves tend to increase for increasing drive, it is possible that the moving flux lines are in the weakly interacting regime and move independently and the flux lines will be in the disordered phase. On the other hand, if the I-V curves tend to saturate at high drives, the moving flux lines are in the regime where the vortex interaction is dominant. Flux lines would try to form the Abrikosov vortex lattice.

However, the radius of gyration in the direction transverse to the drive increases as the drive increases. It probably also decreases at larger driving forces, but this regime is inaccessible. From the data we have, we see that the radius of gyration in the direction of the drive is much larger than the radius of gyration in the direction transverse to the drive. The drive tries to stretch and push partially unpinned flux lines in its direction. This happens until the vortices find the nearest pinning center to occupy or the elastic energy is comparable to the vortex interaction or pinning potential. Then the partially pinned flux lines will depin and flow in the direction of the drive. The radius of gyration along the y-axis is not affected since there is no drive in that direction. Flux lines only fluctuate randomly around the center of mass unless they are closer to another flux line and then pushed away from each other while they are moving. They tend to reach the same value at the large drives due to the effect from the elastic energy which is trying to straighten the flux line. The spatial fluctuation of the flux lines is limited at a finite radius. We expect that the slope of the radius of gyration along the y-axis should be larger for increasing temperature since the thermal fluctuation cause the flux lines to be more flexible. We do not yet have data to confirm this prediction. Fig. 4.11 shows the plot of the total radius of gyration defined as $R_g = (R_{gx}^2 + R_{gy}^2)^{1/2}$. It is similar to the plot of the radius of gyration in the x-direction, which is much larger in magnitude and contributes to the overall magnitude. Snapshots of moving vortex lines in Fig. 4.12 show the increasing radius of gyration at low, intermediate, and high drive. Flux lines become very flexible at large drives according to the large radius of gyration.

The fluctuations in the radius of gyration are measured for both x- and y- direction by means of the standard deviation. They behave similarly but differ in magnitude. The standard deviation reaches the maximum just above the critical depinning threshold and becomes small at small and high drives. This shows that there is a significant competition between the pinning potential, elastic energy, driving force, and vortex interaction in the critical regime. For increasing vortex density, the width of the standard deviation decreases as a result of the stronger vortex interaction and a coherent motion of flux lines.

The magnitude of the standard deviation in the y-direction is smaller than the one along the x-axis since the radius of gyration is not affected by the drive in the y-direction. Table 4.2 shows the value of the standard deviation of the radius of gyration for both x- and y-component at the driving force of 2.6. It clearly shows the decrease in the fluctuations for increasing vortex density as the vortex interaction becomes dominant.

Our results differ from the results reported in [33, 103] for much smaller pinning strengths. The data reported there indicate that the radius of gyration, for both x and y direction, in the flowing regime decreases for increasing density. This corresponds to the dynamics which is dominated by the vortex interaction. Our results show the increase in the radius of gyration for increasing density, which is dominated by the pinning potential. The differences arise from the fact that the pinning strength used in this simulation is approximately stronger by a factor of 10 and hence leads to the defect dominated regime. In addition, we simulate our system with a larger penetration length which requires a larger system size to avoid the numerical artifact due to the cut-off interaction. With the same number of vortex lines in the system but larger system size and much stronger pinning strength, we are working in regime where the flux lines are weakly interacting and dominated by the defects.

4.2.2 Point Defects

Point defects directly affect the dynamics of the flux lines. In contrast to systems with columnar defects, this kind of disorder promotes the wandering of the moving flux lines. The effective pinning force on the flux line is incoherent in direction and small in magnitude. The random pinning centers try to pull the vortex lines in the different direction as they traverse the sample, which leads to less effective pinning. In the regime where the defects dominate the dynamics, the radius of gyration for point defect is then expected to be larger than at systems with columnar defects. The dynamics is then explained by the collective pinning theory [100], which describes the dynamics of flux lines in the presence of weak pinning centers.

Fig. 4.16 shows the radius of gyration along the direction of the drive. The shape of the curve is slightly different from the curve from the system with columnar defect. At small drives, the radius of gyration at specific drive slightly increases for increasing density while we observe a large deviation in the system with columnar defects. Therefore, the system with columnar defects is strongly dominated by the pinning centers. For increasing drives, the radius of gyration keeps increasing from the low driving regime and reaches its maximal value at just above the critical depinning threshold. This indicates that the dynamics of the system is slightly dominated by the pinning potential until it reaches the critical threshold.

The radius of gyration then starts to decrease at higher drives just above the critical depinning threshold. This shows that the dynamics is dominated by the vortex interaction which can be seen by the decrease of the radius of gyration for increasing vortex density at a specific drive. The repulsive vortex interaction causes the flux lines to repel each other and tries to form a vortex lattice. This clearly demonstrates that the driving force

plays an important role in the competition between the vortex interaction and pinning potential. Similar to the results from the system with columnar defect, the driving force can change the dynamics from the defect dominated regime to the vortex interaction dominated regime at high vortex densities of 64 and 100 lines. However, this transition is not obvious for the system with columnar defect since we do not observe the decrease in the radius of gyration for increasing drive. In the absence of the drive, the energy due to the pinning potential is greater than the vortex interaction and hence dominates the overall energy. As the driving force increases, the work done on the flux line tries to reduce the free energy and smoothens out the effect due to the pinning centers. Therefore, the dynamics is dominated by the vortex interaction at large driving forces.

For varying densities of vortices, the maximal magnitude of the radius of gyration decreases for increasing vortex density. The maximal magnitude for the radius of gyration in this system is much larger than in the system with randomly placed columnar defects. This is strong evidence showing that uncorrelated defects assist the wandering of flux lines, which results in a large radius of gyration.

The radius of gyration in the direction transverse to the drive behaves differently. Each curve keeps increasing for increasing drives and shows no tendency of decreasing at higher drive. They tend to merge the same value at high drive. The radius of gyration in this direction is hardly affected by the drive since there is no drive in this direction. Flux lines can only diffuse about its center of mass in the absence of the drive. The distance that the flux line element can move away from the center of mass is limited by the elastic energy of the flux lines. The elastic energy tries to pull the flux line element back to its center of mass, which results in a finite radius of gyration. The magnitude is much lower than the one along the drive. For increasing vortex density, the radius of gyration increases since the dynamics is dominated by the defect. The total radius of gyration and a snapshot of moving vortices are plotted in Fig. 4.18 and Fig. 4.19. Fig. 4.19b shows the largest radius of gyration which is observed at the intermediate drives. The largest radius of gyration for increasing vortex density is shown in Table 4.3.

The fluctuations of the radius of gyration for both x- and y-components is also measured by means of the standard deviation. For the x-component, the width of the standard deviation reaches its maximum just above the critical depinning threshold and becomes smaller at small and high drives. The fluctuations become relevant in this region due to the competition of the different energy terms. For increasing vortex density at specific driving force, the width of the standard deviation gets smaller due to the domination of the vortex interaction. Flux lines becomes stiffer since they try to repel each other and form the vortex lattice, which results in the smaller radius of gyration and its fluctuations. The fluctuations in the y-direction behave differently from the one in the x-direction. For increasing driving force, the fluctuations or the width of the standard deviation becomes smaller. The driving force smoothens the pinning potential and causes the vortex interaction to dominate the dynamics. For increasing vortex density, the fluctuations get smaller due to the stronger vortex interaction.

The results from this part are partially similar to the results reported by Bullard, which is for systems with weak point defect at large driving force [33, 103]. Our results

for the radius of gyration in the x-direction well above the critical depinning threshold are similar. The decrease of the radius of gyration for increasing vortex density is observed in both studies. The results just below the critical threshold are different. Our results show a small increase in the radius of gyration for increasing vortex density. This result is not reported in that work. For the radius of gyration in the y-direction, our results are also different. Our radius of gyration grows as the vortex density increases while the results by Bullard show a decrease.

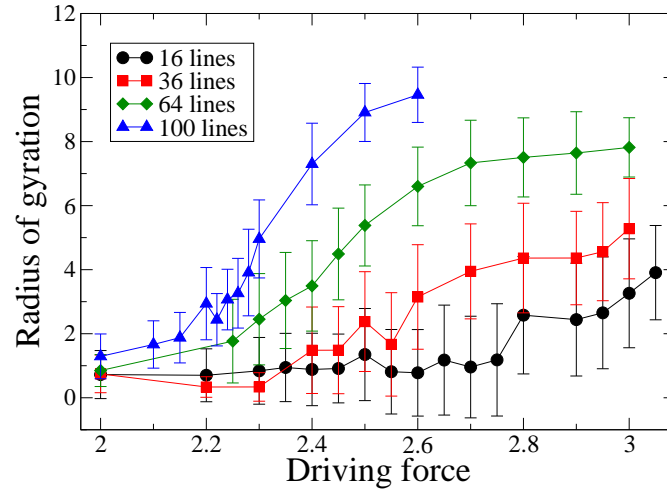


Figure 4.9: Radius of gyration along the direction of the drive for systems with random columnar defects for different densities of flux lines: 16 lines (circle), 36 lines (square), 64 lines (diamond), and 100 lines (triangle up). The radius of gyration tends to increase at all drives as the density of flux lines increases.

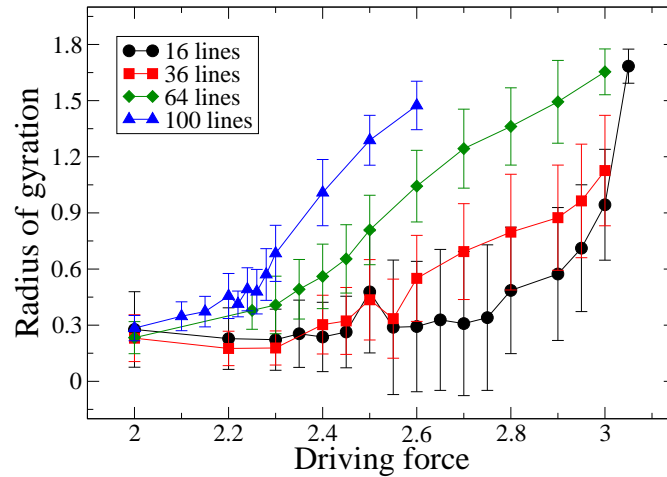


Figure 4.10: Radius of gyration along the direction transverse to the drive for systems with random columnar defects for different densities of flux lines: 16 lines (circle), 36 lines (square), 64 lines (diamond), and 100 lines (triangle up). The radius of gyration tends to increase at all drives as the density of flux lines increases.

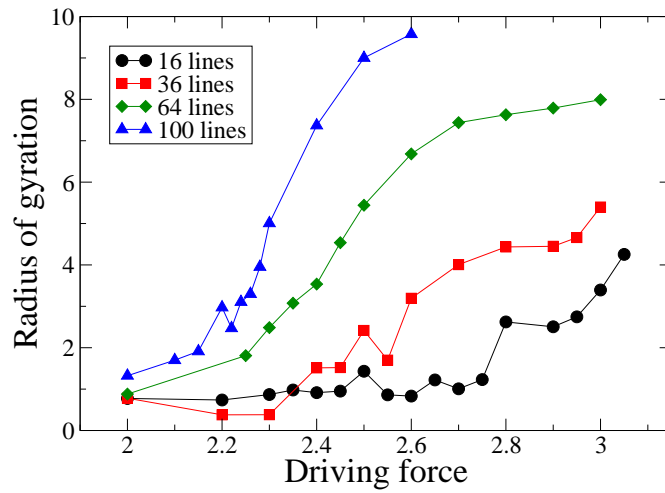


Figure 4.11: Total radius of gyration for systems with random columnar defects for different densities of flux lines. 16 lines (circle), 36 lines (square), 64 lines (diamond), and 100 lines (triangle up). The radius of gyration tends to increase at all drives as the density of flux lines increases.

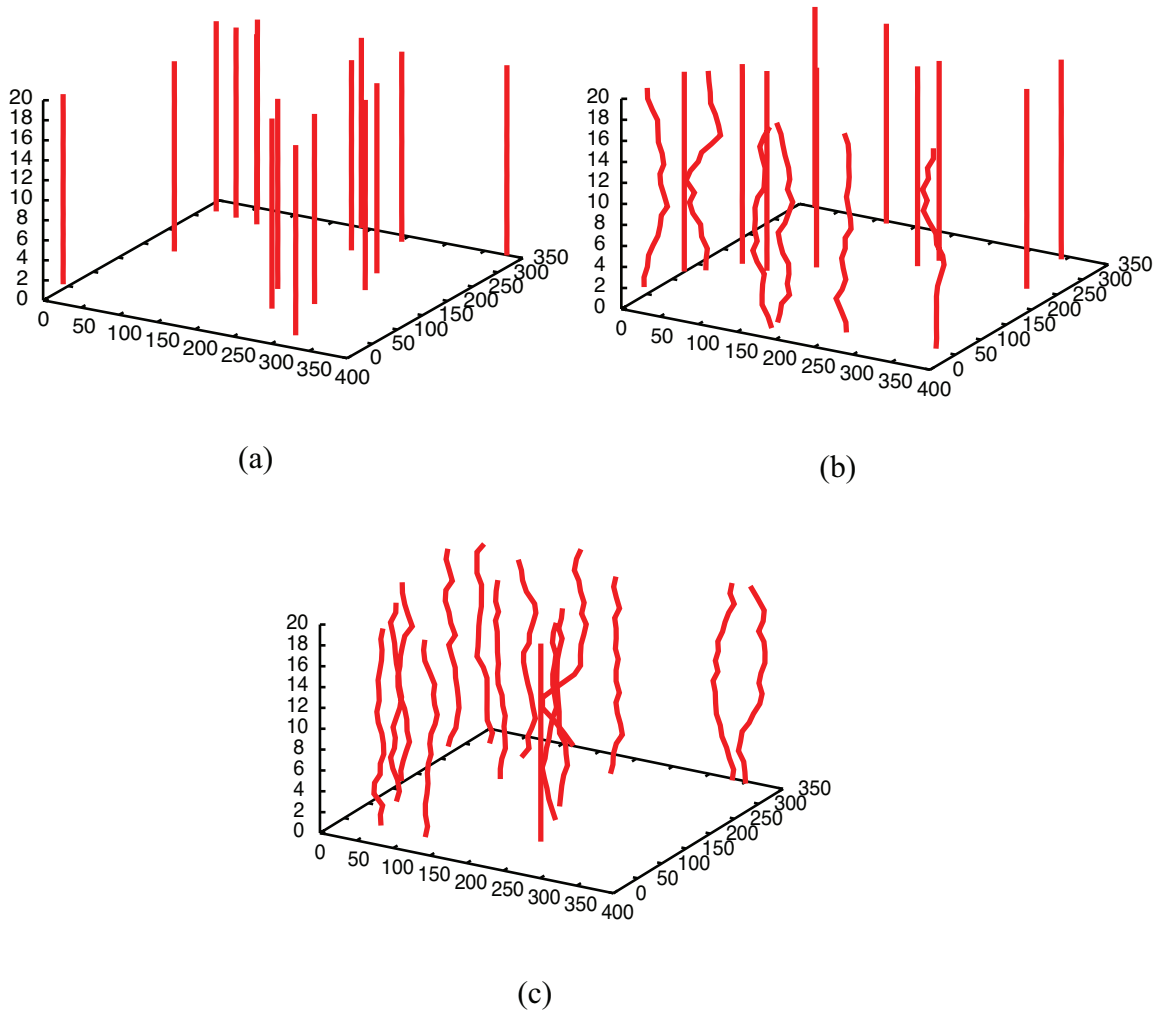


Figure 4.12: Snapshots of moving vortices in the presence of randomly placed columnar defects at (a) low, (b) intermediate, and (c) large drive. Vortex lines are in (a) pinned Bose glass phase, (b) partially pinned Bose glass and moving Vortex glass/liquid phase, and (c) moving Vortex glass/liquid phase.

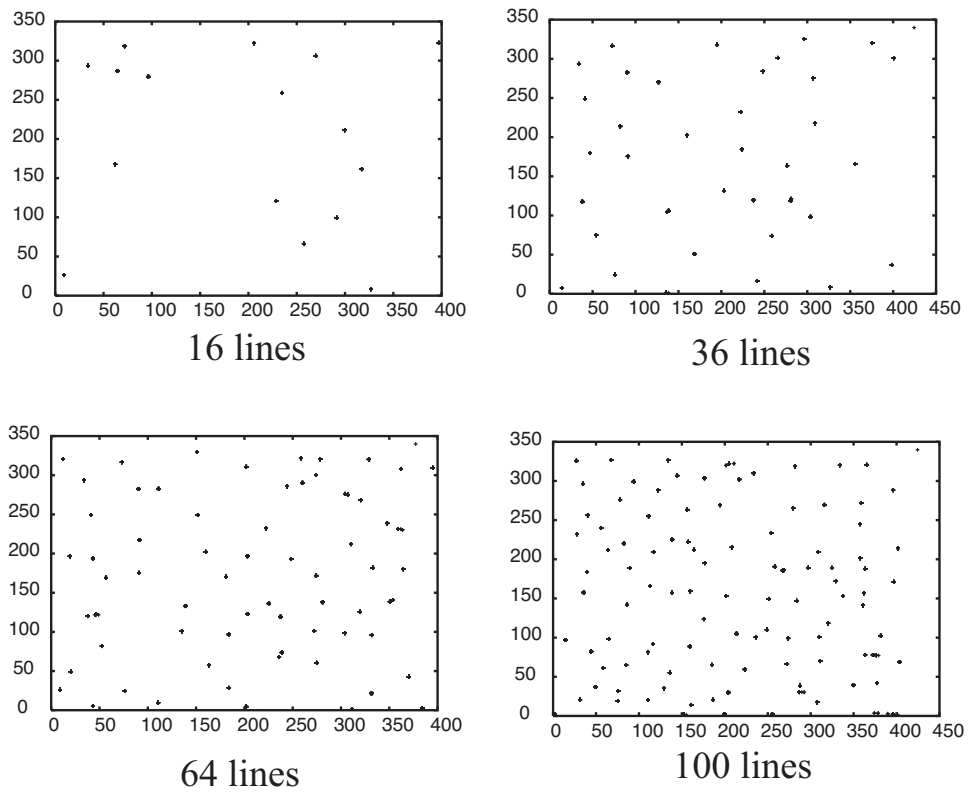


Figure 4.13: Top-view snapshots of the pinned Bose glass for various vortex density. The randomly placed columnar defects are not shown in the figure. At low driving force, all flux lines are localized inside the pinning centers at low drive. The direction of the driving force is from left to right.

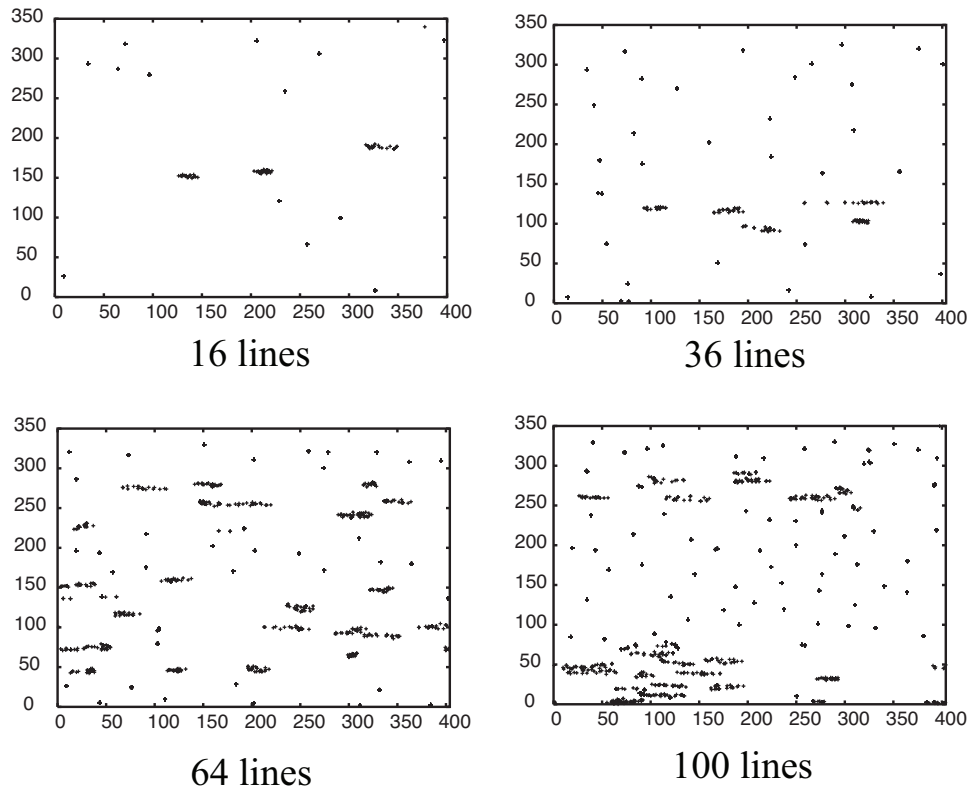


Figure 4.14: Top-view snapshots of partially pinned and moving vortex lines for various vortex densities. The randomly placed columnar defects are not shown in the figure. At intermediate driving force, some of the flux lines are localized inside the pinning centers while the rest of them are moving. It can be seen that the radius of gyration increases for increasing vortex density. The dynamics is governed or dominated by the defects. The direction of the driving force is from left to right.

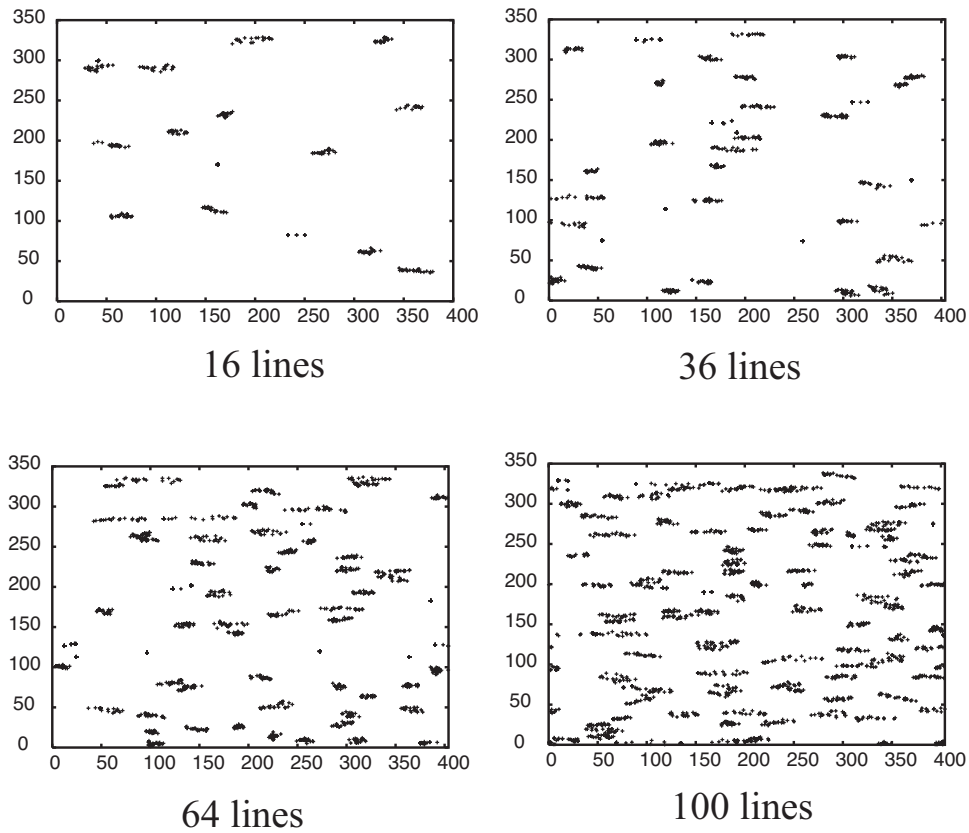


Figure 4.15: Top-view snapshots of moving vortex lines for various vortex densities. The randomly placed columnar defects are not shown in the figure. At high driving force, all of the flux lines are moving and display a liquid-like structure. The direction of the driving force is from left to right.

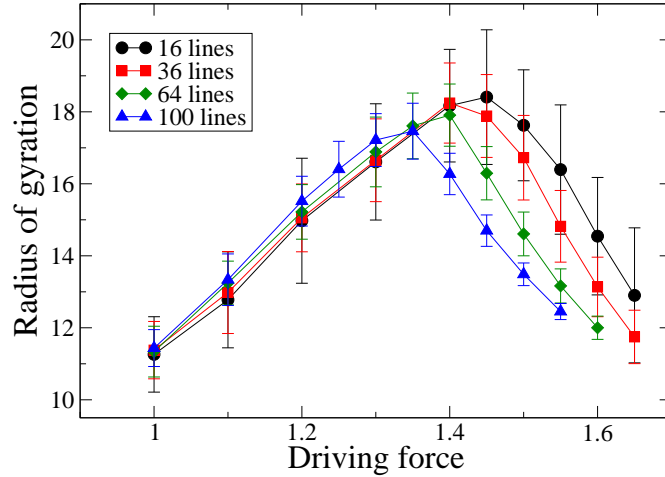


Figure 4.16: Radius of gyration along the x-axis for systems with point defects for different densities of flux lines: 16 lines (circle), 36 lines (square), 64 lines (diamond), and 100 lines (triangle up). The radius of gyration starts to increase as the drive increases and reaches the highest value at the critical current and then decreases.

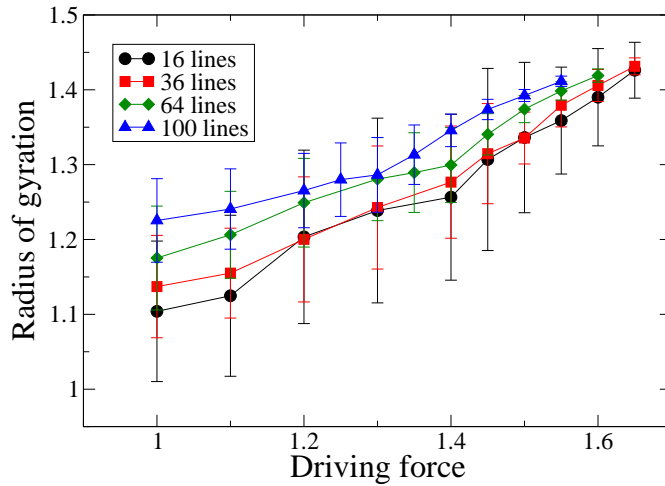


Figure 4.17: Radius of gyration along the y-axis for systems with point defects for different densities of flux lines: 16 lines (circle), 36 lines (square), 64 lines (diamond), and 100 lines (triangle up). The radius of gyration keeps increasing as the drive increases.

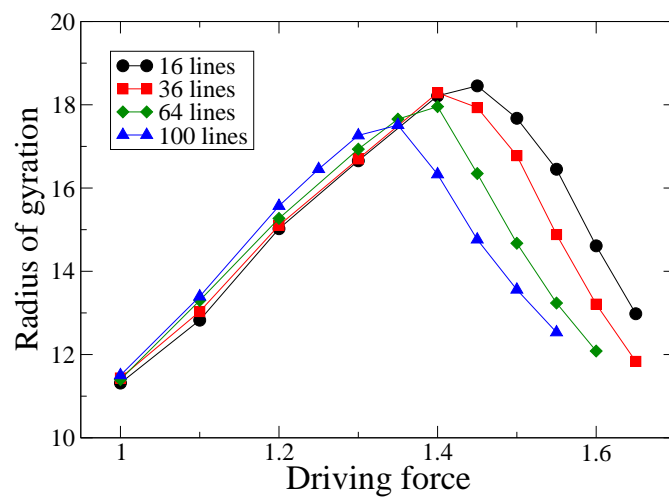


Figure 4.18: Total radius of gyration for systems with point defects for different densities of flux lines: 16 lines (circle), 36 lines (square), 64 lines (diamond), and 100 lines (triangle up).

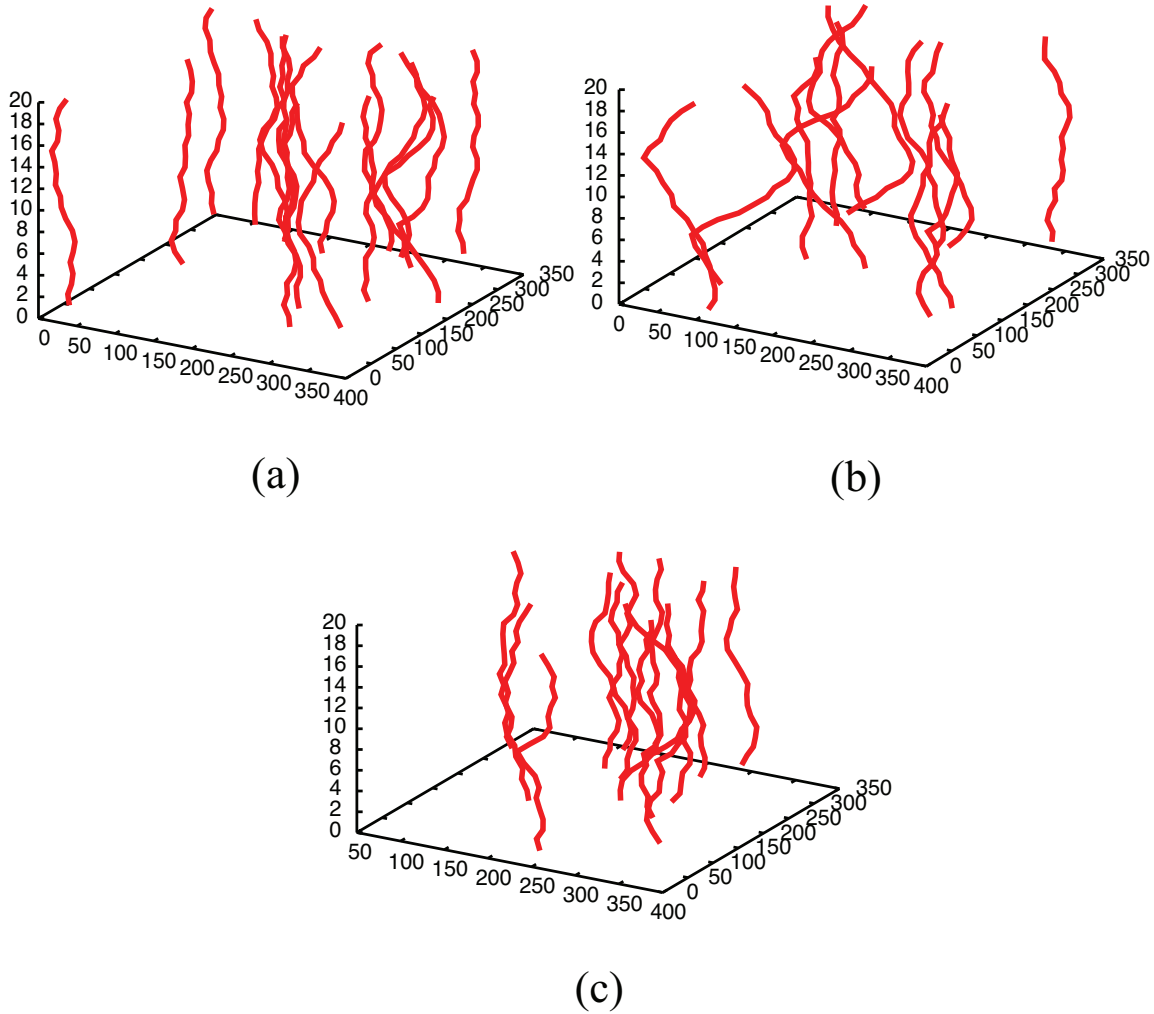


Figure 4.19: Snapshots of moving vortices in the presence of randomly placed point defects at (a) low, (b) intermediate, and (c) large drive. Flux lines are in (a) pinned vortex glass phase, (b) and (c) moving liquid/vortex glass phase. Vortex lines have the largest average radius of gyration at intermediate drive.

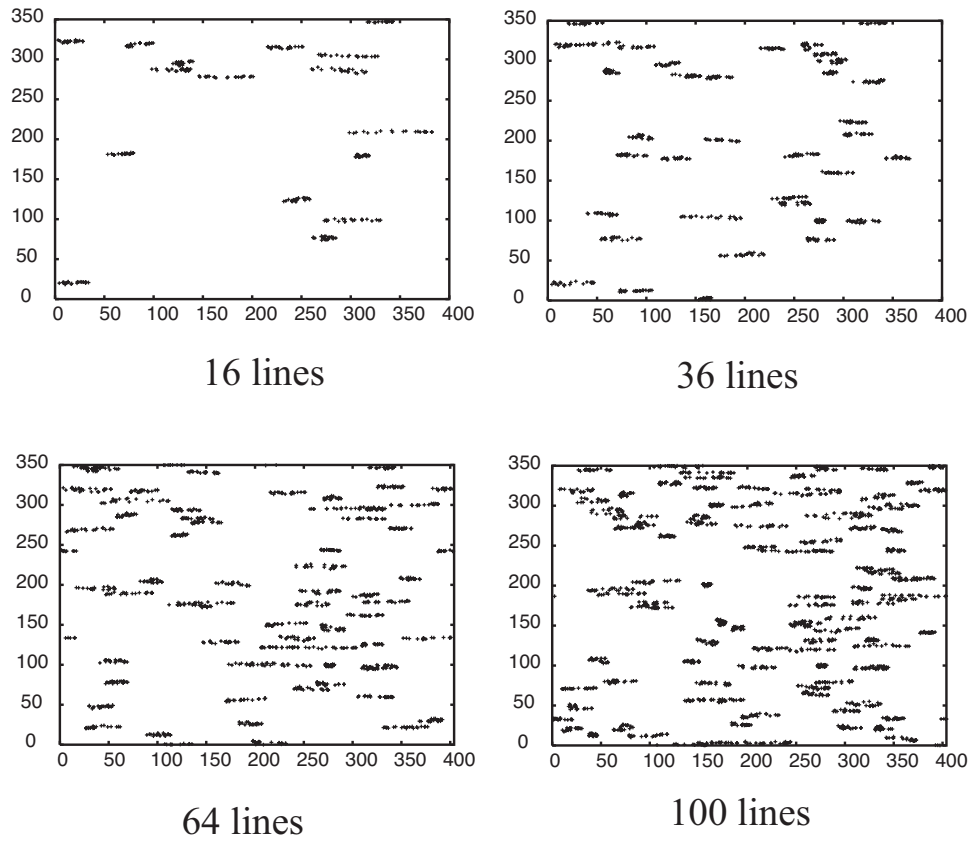


Figure 4.20: Top-view snapshots of moving vortex lines for various vortex densities in the presence of the point defects. The randomly placed point defects are not shown in the figure. At all drives investigated, all of the flux lines are moving and have liquid-like structure. Flux lines stretch along the direction of the drive to find their minimal energy configuration. The direction of the driving force is from left to right.

Table 4.2: Fluctuations in the radius of gyration: columnar and point defects

Vortex density (lines)	Columnar defect		Point defect	
	x-component	y-component	x-component	y-component
16	1.35	0.35	1.54	0.100
36	1.63	0.23	1.17	0.034
64	1.22	0.19	0.60	0.018
100	0.86	0.13	0.31	0.008

Table 4.3: Maximal radius of gyration for the system with point defects

Vortex density (lines)	Maximal radius of gyration (b_0)
16	18.45
36	18.28
64	17.95
100	17.51

4.3 Half-Loop and Double-Kink Excitations

The transition of the dynamics from a regime dominated by disorder to one dominated by the vortex interactions as induced by the driving force has been explained in the previous section. A large radius of gyration of the vortex lines appears at large driving forces for systems with both randomly placed point and columnar defects. At low driving force, the structure of the flux line in both systems is different. Columnar defects promote the straightening of the flux lines while in systems with point defects wandering is promoted. The localized Bose glass in systems with columnar defects at low driving force is observed in our results. Here we describe the conditions for the half-loop, double-kink, and superkink excitations to exist, which were theoretically investigated in Refs. [51, 104]. We shall see that the occurrence of double-kinks or superkinks is a rare event at low temperatures.

Our results obtained from the simulations show that excitations via half-loops are prominent in the intermediate driving force regime corresponding to the prediction. At each vortex density, half-loop excitations occur at intermediate drives and their number decreases for increasing drive. A larger number of half-loop excitations is observed as the density is increased. This indicates that the vortex interaction might play an important role for the existence of half-loop excitations.

Double-kinks, however, are not observed in our simulations at small currents as predicted: because of low statistics, their rate of occurrence would be very low. They appear at drives larger than the critical depinning force. The presence of the double-kinks is not due to thermal fluctuations but strong pinning. As the flux line is moving, it is possible that some vortex elements enter the pinning centers. These flux line elements are trapped while the rest of them are driven along the direction of the drives. The lines keep stretching until the elastic energy overcomes other energies and cause the trapped flux line elements to depin from the defect. This would result in the structure of double-kinks. This is shown in Fig. 4.23.

The following equations in the rest of this subsection are derived in Refs. [51, 104]. In the presence of a columnar defect, the critical current is estimated by $J_c = cU/\phi_0 l_\perp$ where l_\perp is the root-mean-square transverse wandering and U is the pinning strength. To predict the value of the critical current, U is simply the pinning strength of the columnar defect and l_\perp is the radius of the columnar defect b_0 , which is temperature dependent. In a similar manner, one can predict the depinning threshold for the flux line to have a half-loop and double-kink configuration by setting the transverse wandering distance l_\perp to $b_0 < l_\perp < d$ and $l_\perp = d$, where d is the average spacing between two columnar defects. The half-loop is then predicted to occur in the regime of moderate driving force, $J_1 < J < J_c$, where

$$J_c = \frac{cU_0}{\phi_0 b_0}, \quad J = \frac{cU_0}{\phi_0 l_\perp}, \quad \text{and} \quad J_1 = \frac{cU_0}{\phi_0 d}.$$

Obviously, the distance that the flux line extends in the direction transverse to the columnar defect is inversely proportional to the current. The larger the distance that flux line extend, the smaller a current is required. One is interested in the probability of finding

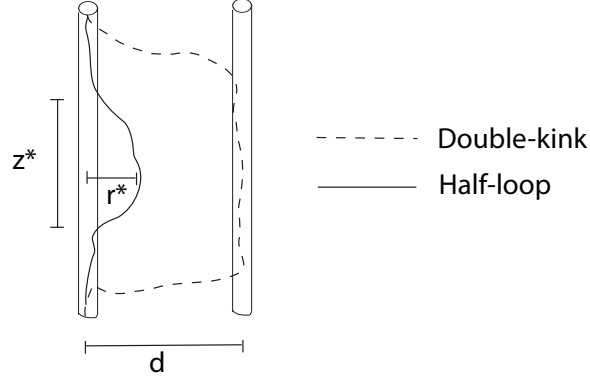


Figure 4.21: A flux line extends by a length of r along the drive direction and separates by a length of z from the columnar defect. The mean distance between two columnar defects is d .

half-loop excitation by determining the phenomenological free energy barrier of a single driven flux line, which is described in the last section

$$F_1 = \int_0^L \left[\frac{1}{2} \tilde{\epsilon}_1 \left[\frac{d\mathbf{r}}{dz} \right]^2 + V_1[\mathbf{r}(z)] - \mathbf{f}_L \cdot \mathbf{r}(z) \right] dz,$$

where the Lorentz force is $f_L = J\phi_0/c$. One can simply estimate the magnitude of each term and obtains

$$\delta F_1(r, z) \approx \frac{\tilde{\epsilon}_1 r^2}{z} + U_0 z - f_L r z.$$

The first term is due to the elastic energy of the flux line wandering with the radius of r . The second term is the increase of the free energy due to unoccupied pinning center of a length z . The last term is the energy due to the Lorentz force. In the absence of the Lorentz force, optimization of the free energy with respect to r and z , $\delta F_1(r, z)/\delta r$ and $\delta F_1(r, z)/\delta z$, results in the saddle-point parameters

$$r^* = \left[\frac{U_0}{\tilde{\epsilon}_1} \right]^{1/2} \quad z^* = \frac{U_0 c}{\phi_0 J}.$$

Inserting these parameters back into the above free energy equation, one obtains the saddle-point energy of the flux line

$$\delta F_1^* = \frac{c \tilde{\epsilon}_1^{1/2} U_0^{3/2}}{\phi_0 J}.$$

With the definition of the Lorentz force, one can simplify this energy of the thermally activated half-loop, double-kink, and superkink excitations into the form of

$$E^* = \delta F_1^* = \sqrt{\tilde{\epsilon}_1 U_0} r,$$

where z and r are the distances that the flux line extends along and transverse to the pinning center. For $r > 0$ or $J > 0$, these excitations represent saddle points that yield

energy barriers for the motion of flux lines. According to the thermally assisted flux flow model for vortex transport, the temperature dependent resistivity is approximated by

$$\rho(T) \approx \rho_0 e^{-U_B(J)/T}.$$

In the presence of these excitations, the system needs to overcome this energy barrier $U_B(J) \approx E^*$ in order to set flux lines in motion.

In the case of the double-kink and superkink, part of the flux line extends to the nearby columnar defect. Since this involves two columnar defects, the second term of the energy of the flux line wandering is modified as

$$E \approx 2E_k \frac{r}{d} + \varepsilon(r)z - f_L r z.$$

where the first term is the energy of the kink extending by the distance of r . A factor of 2 comes from the fact that there are two legs extending out of the columnar defect. The second term is the energy due to the localized flux line of length z in the nearby columnar defect with the difference in the pinning potential $\varepsilon(r)$. In the case where the pinning strength of the columnar defects is of equal magnitude, the energy of the double kink $E_k = \sqrt{\tilde{\epsilon}_1 U_0} d$ is obtained if one sets the transverse distance $r = d$. The superkink is obtained if $r = 2d, 3d, 4d$, and so on. For different pinning strength, $\varepsilon(r)$ is the difference in the pinning potential between two columnar defects which can be approximated by

$$\varepsilon(r) \approx \frac{1}{n_0(\mu) r^{d_\perp}}.$$

where $n_0(\mu)$ is the density of states at the chemical potential. d_\perp denotes the number of transverse dimensions, which is 2 in this case. In the absence of the Lorentz force, optimizing the free energy with r and z yields the saddle-point parameters

$$Z^* \approx \frac{E_k n_0(\mu)}{d} (R^*)^3.$$

Optimizing in the presence of the Lorentz force respect to z leads to

$$R^* \approx \left[\frac{1}{n_0(\mu) f_L} \right]^{1/3}.$$

By using the above parameter and optimizing the free energy with r , one obtains

$$R^* \approx \left[\frac{Z^* d}{E_k n_0(\mu)} \right]^{1/3}.$$

These last two saddle-point parameters lead to $f_L = E_k/Z^* d$ and the energy of the saddle-point configuration of

$$E^* \approx \frac{E_k}{d} \left[\frac{c}{n_0(\mu) \phi_0 J} \right]^{1/3}.$$

There exists a soft ‘‘Coulomb’’ gap [105] in the distribution of pinning energies, which is analogous to the density of states $n_0(\mu)$. At $T = 0$ this $n_0(\mu) \rightarrow 0$ when long-range interactions are present. This leads to the divergence of the saddle-point energy. Thus large double-kinks or superkinks are very rare to occur since they are energetically unfavorable.

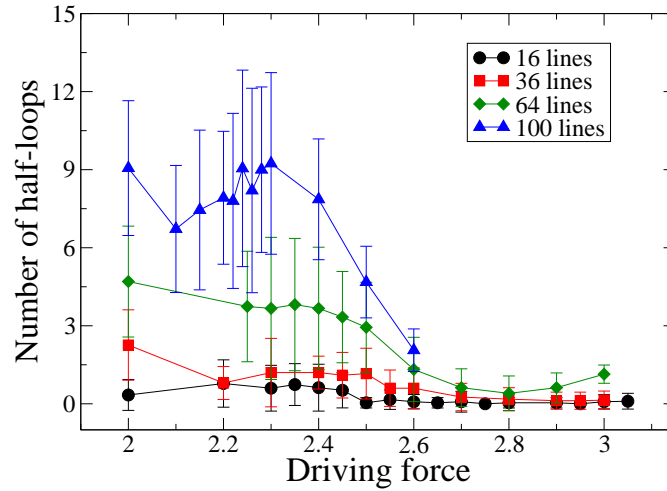


Figure 4.22: Number of half-loops for systems with random columnar defects for different densities of flux lines: 16 lines (circle), 36 lines (square), 64 lines (diamond), and 100 lines (triangle up). The number of half-loops shows a maximum just above the critical current and then tends to decrease at all drives as the density of flux lines increases.

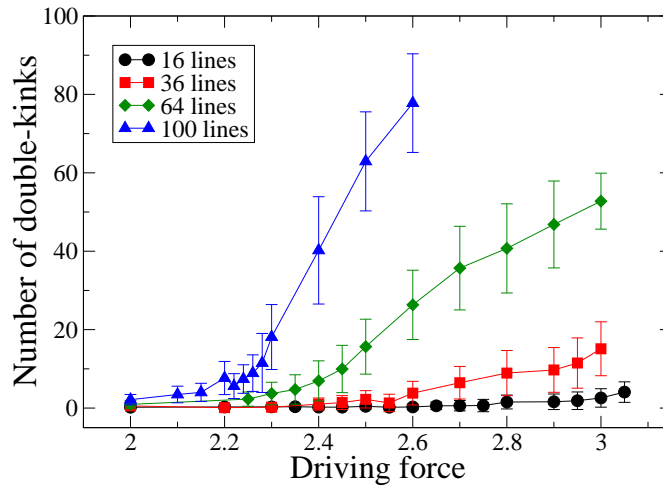


Figure 4.23: Number of double-kinks for systems with random columnar defects for different densities of flux lines: 16 lines (circle), 36 lines (square), 64 lines (diamond), and 100 lines (triangle up). The number of double-kinks tends to increase at all drives as the density of flux lines increases.

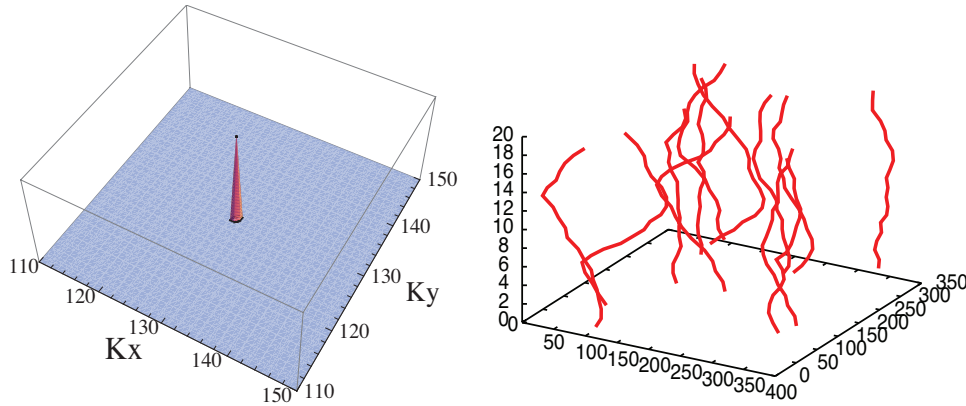


Figure 4.24: A static structure factor plot and a sample snapshot of moving vortex lines, seen in our simulations at all drives and vortex densities, in the non-equilibrium steady state. Due to the strong pinning strength, this single peak corresponds to the moving plastic or moving liquid phases of vortices as seen from a snapshot.

4.4 Diffraction Plot/Structure Factor

In the regime that we study, the pinning strength is very strong which results in the plastic or liquid motion of flux lines when high enough drives are applied. Experimentally, this plastic motion can be indicated directly by means of a single peak in a diffraction plot/ structure factor. We observed this behavior for all our results in this strong pinning regime. We have investigated this quantity in a different system of weak pinning defects and observed hexagonal Brag peaks corresponding to the hexagonal structure of the moving flux lines. Fig. 4.23 shows an example of the diffraction plot in a system with point defects. The single peak indicates the presence of an isotropic liquid or a disordered solid of moving flux lines. In order to support this result, the snapshots in Fig. 4.13, Fig. 4.14, Fig. 4.15, and Fig. 4.20 show these liquid-like disordered structures.

4.5 Voltage Noise Spectrum

The voltage noise due to the motion of vortices in systems with randomly placed columnar and point defects is measured. Narrow band noise is observed in systems with point defects, but the frequency does not match with the washboard frequency. The washboard frequency is predicted to be proportional to the average velocity of moving vortices and inversely proportional to the lattice constant, $\omega = 2\pi\langle v \rangle/a_0$. It is explained that the presence of this washboard noise is due to the periodicity of the voltage signal, which is observed to drop when the moving flux line moves across the sample of thickness W . This keeps happening and yields the frequency of $f = 1/\tau$, where τ is the time it takes the flux line to move for one lattice constant a_0 . One can see that this periodic signal of the voltage drop occurs when the moving flux lines maintain the periodic structure such as the Abrikosov vortex lattice, i.e., each flux line moves with the same characteristic frequency f or time τ . The washboard signal disappears if each flux line moves independently, i.e., each flux line gives different characteristic frequency f or time τ . This results in the well known broadband noise. The presence of strong pinning centers can give rise to this independent characteristic time τ since it tries to stop the motion of flux lines as previously seen from the last sections. Here we investigate the effect of strong pinning centers, such as strong point and columnar defect, on the behavior of the washboard noise. The range of the frequency in our simulations is between 0 and 0.5 rad/MCS while it is reported to be between 0 and 1600 Hz in the experiment performed by Togawa [89]. The results of this work is dramatically different from the results reported by [33, 103] for much weaker pinning strengths.

4.5.1 Randomly Placed Point Defects

Broadband noise is observed for systems with point defects at all vortex densities. The results are averaged over 50 defect realizations and initial vortex positions. We investigate in the regime where the driving force is set to 1.5, where the system has reached a non-equilibrium steady state. The presence of broadband noise indicates the existence of the moving liquid phase which is in agreement with the experimental result in the peak effect regime [94]. This is strongly supported by the appearance of the single peak in the structure factor and the snapshot of moving vortex liquid in Fig. 4.25. As previously explained, each flux line in this system with strong point defect moves independently, which gives a different characteristic time τ . This leads to the loss of washboard signal in our results. However, washboard noise is observed in the system with weak point defect [33, 103]. In the presence of the weak pinning centers, a system of flux lines forms the moving Bragg glass, which is a quasi-long-ranged ordered structure. The characteristic time of each moving flux line slightly deviates from its mean value and hence can still give rise to the washboard frequency.

The magnitude of the broadband noise decreases for increasing vortex density, indicating that the flux lines tend to reorder at higher vortex density. This is also reflected by the decrease of the radius of gyration for increasing vortex density. The magnitude of the noise indicates the fluctuations of the velocity around its mean. The larger the magnitude

of the noise, the larger the value of the velocity deviated from its mean. At higher vortex density, the vortex interaction dominates the system and causes the flux lines to be stiffer. The stronger vortex interaction energetically favors the Abrikosov vortex lattice which is less noisy and gives the smaller magnitude of the broadband noise. The decrease of the noise power for increasing vortex density or interaction strength has also been reported in both experiment and numerical simulation [90, 94].

The $1/\omega^\alpha$ -like broadband noise has also been reported in simulations of two- and three-dimensional vortex models [85]. The two-dimensional Coulomb gas model for vortex-antivortex pair fluctuations is used in that work. The exponent of $\alpha = 1.5$ was obtained in the system in the absence of a magnetic field, with the number of vortices equals to the number of antivortices. The $1/\omega$ behavior is observed in the system with applied magnetic field, when the number of vortices is slightly greater than the number of antivortices. This is similar to the experimental results by Roger [106] and Festin [107]. In that work, the voltage noise is temperature dependent. The voltage noise at high frequency behaves like $1/\omega$ at higher temperature and like $1/\omega^{3/2}$ at lower temperature. This value of $\alpha = 1.5$ is obtained from a functional renormalization group calculation for point defects to one-loop order in three-dimensions [108]. Also in that work, the $1/\omega$ behavior is observed at $T = T_c$, in the absence of a magnetic field, in the three-dimensional vortex loop model. In the presence of a small number of vortices, the $1/\omega$ behavior is observed for a broader range of temperature, near the critical temperature. The voltage noise power spectrum in our work, with strong pinning centers, varies approximately like $1/\omega^\alpha$ with α close to 1.3, which is well fitted in the low frequency regime. This value is obtained by plotting a function of $1/\omega^\alpha$ with different α , and then comparing to the curve of the voltage noise. We expect that the value of the exponent α obtained by this method would be slightly different from the real value. By using this method, the value of $\alpha = 1.7$ is obtained in the intermediate frequency regime. Our exponent value is smaller than the exponent $\alpha = 2$, which is the mean-field value, as found in the system of driven vortices interacting with weak point and columnar defects [109]. Fig. 4.27 shows the voltage noise along the x-direction for selected driving forces and various vortex densities. The moving flux lines are in the flowing regime before the saturation. The results demonstrate that all the voltage noises behave in a similar manner, $S(\omega) \propto 1/\omega^{1.3}$. It shows no narrow band peaks at all drives and fields, indicating the presence of moving fluid or disordered structure at all drives and fields.

As shown in Fig. 4.26, the y-component of the broadband noise is observed to be nearly flat white noise and decreases in magnitude for increasing vortex density. The smaller magnitude of the noise is due to the smaller velocity fluctuations and hence the presence of white noise. The motion of the vortex lines in the y-direction is not affected since there is no driving force in this direction. Each moving flux line can only fluctuate around its center of mass which results in zero average velocity.

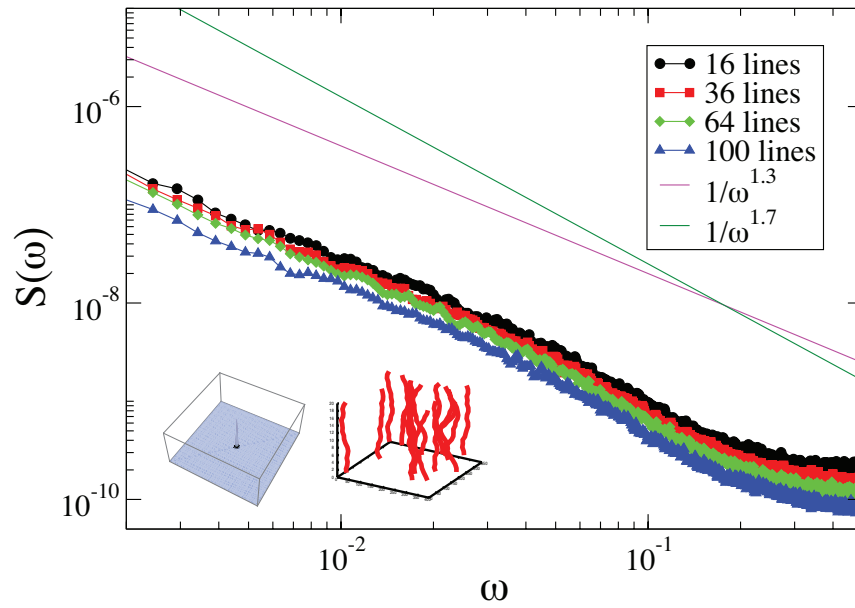


Figure 4.25: Voltage noise in the drive direction for systems with randomly placed point defects at various vortex densities. The driving force along the x-axis for each curve is set to be 1.5. The magnitude for each curve increases as the vortex density increases from 16 to 36, 64, and 100, respectively. The broadband noise in these systems reflects the property of the moving disordered phase, such as a moving liquid or plastic phase. This is supported by the single peak in diffraction plot and the snapshot of disorderly moving flux lines on the bottom left of the figure. The scaling behavior with $f \propto 1/\omega^{1.3}$ and $f \propto 1/\omega^{1.7}$ are plotted for the low and intermediate frequency regime, respectively.

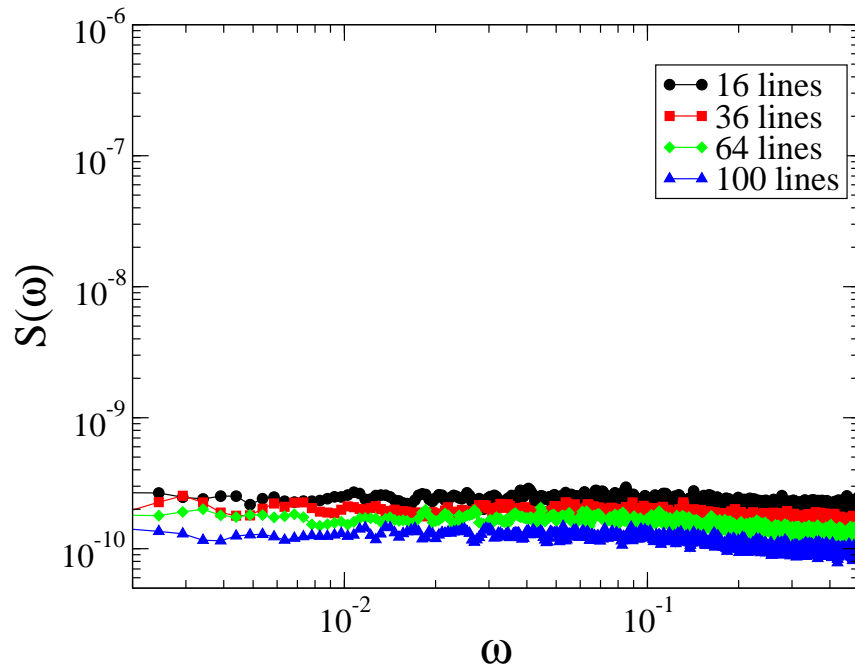


Figure 4.26: Voltage noise in the transverse direction to the driving force (y-direction) for systems with randomly placed point defects at various vortex densities. The driving force in the x-axis for each curve is set to be 1.5. Similar to the voltage noise in the x-direction, the magnitude for each curve decreases as the vortex density increases from 16 to 36, 64, and 100, respectively. The broadband noises in these systems reflect the property of the moving disordered phase, such as moving liquid or plastic phase. However, the slope of the broadband noises in these systems is smaller than those along the x-direction.

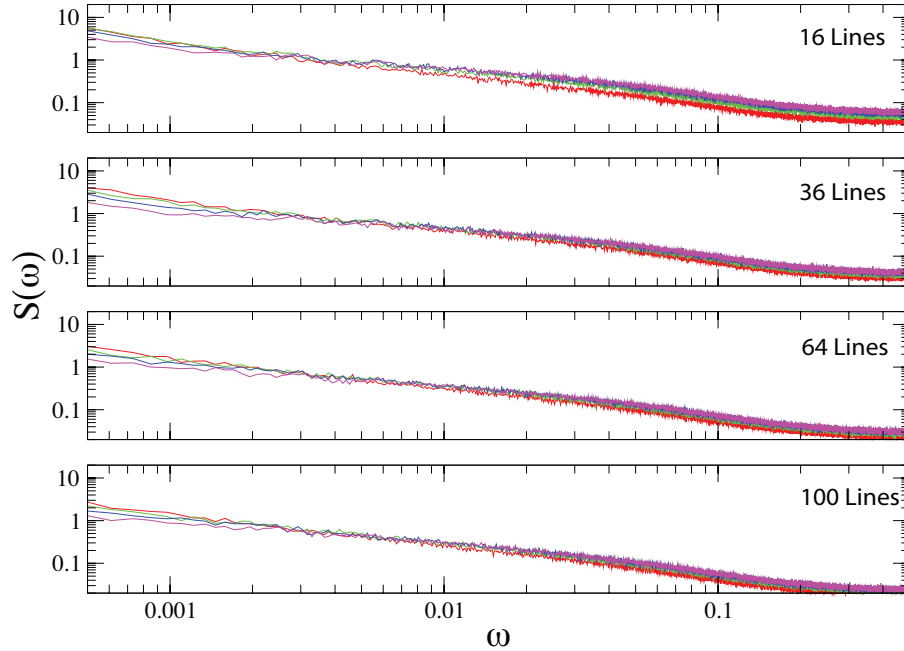


Figure 4.27: Velocity/voltage power spectra for a system with randomly placed point defects at various velocities. From the top to bottom the number vortex lines increases from 16 to 36, 64, and 100. Broadband noise peaks are observed at all densities and velocities of vortex lines. For each density, the magnitude of each peak is increased for increasing velocity which is shown as a red, green, blue, and pink line, respectively. Moving vortex lines are in the moving plastic or moving liquid phases supported by the single peak in the structure factor and a snapshot of moving flux lines.

4.5.2 Randomly Placed Columnar Defects

Narrow band noise is observed for the systems with a number of 16, 36, 64, and 100 flux lines. The results are the average taken over 50 realizations of the defect and initial vortex positions. Fig. 4.28 shows the plot for the x-component voltage noise for a system in a non-equilibrium steady state with the driving force of 2.7 along the x-direction. The fundamental frequency and its harmonics for each vortex density are measured to be the same or very close; 0.0038, 0.0075, 0.012, 0.016, 0.019, and 0.023. As described in the last section, the presence of these narrow band peaks suggests a periodicity of moving vortices in the x-direction. This contradicts with the results obtained in the previous sections. Our results show that the moving vortices in the presence of the strong columnar defects are in the moving liquid phase. This is supported by the existence of the single peak in structure factor and the snapshot of a liquid structure of the flux lines. The voltage noise should then behave like a broadband noise and shows no narrow band peaks.

To understand the nature of these observed peaks, we then calculate the associated length scale corresponded to these peaks. The washboard frequency, $\omega = 2\pi\langle v \rangle/a_0$, is then calculated and compared to the frequency of the observed peaks. The average velocity and the lattice constant for each system are required in order to obtain this quantity. The average velocity for the systems of 16, 36, 64, and 100 flux lines at this driving force is 0.00359, 0.00911, 0.0267, and 0.0434, respectively. The associated lattice constants for each system are $101b_0$, $67.4b_0$, $50.5b_0$, and $40.4b_0$. The calculated fundamental washboard frequencies for each vortex density are 0.000223, 0.000567, 0.00166, and 0.00267. These values are incompatible with the observed frequency of 0.0038, which is observed for all vortex density. Hence, our observed frequency is independent of the average velocity and the vortex density or the lattice constant. This is compared in Table 4.4.

Normally, the associated length scale for the washboard frequency is the lattice constant. The length scale for each system is then calculated from the observed frequency and the average velocity. The calculated length scales, in the unit of b_0 , for the first six narrow band frequencies for the system of 16, 36, 64, and 100 lines are shown in Table 4.5. The explanation for the presence of these narrow band peaks in the x-direction will be at the end of this subsection, after comparing to the results obtained in the y-direction.

The power of the narrow band noise increases for increasing vortex density but tends to decrease for higher harmonics. This indicates that the flux line is less stiffer at higher vortex density. This is also supported by the increase in the radius of gyration for increasing vortex density. The moving vortices are in the regime where the pinning centers dominate the dynamics. In addition, the larger velocity fluctuation gives the larger power output as observed in the power spectrum. As seen in Fig. 4.5, the standard deviation of the moving flux lines at driving forces of 2.6 and 2.7 decreases for increasing vortex number. This is different from the results obtained in the system of weak pinning strength where the smaller velocity fluctuation and hence the smaller power output are observed [33].

The narrow band peaks for the y-component are also observed for all vortex density, but with much lower magnitude. The noises are more flatten, which indicates that they have smaller velocity fluctuations. The fundamental frequency for each vortex density is approximately the same. The power tends to increase for the increasing vortex density, indicating the larger velocity fluctuations. However, the associated length scales cannot be calculated since the average velocity for all vortex density are extremely small, which can be considered as zero. The existence of the narrow band peaks in the absence of a driving force in the y-axis can be explained in the term of fluctuation of the flux line inside the pinning center.

Due to the fact that there is no driving force in the y-direction, the dynamics of the pinned vortex line in the y-direction is due to the repulsive vortex interaction from the nearby moving vortex lines. Consider a situation where a flux line is pinned inside the columnar defect, the energy due to the repulsive vortex interaction gets stronger as the other moving vortex lines get closer. This causes the pinned flux line elements to move away from the center of the columnar defect with a specific velocity. After the moving vortex lines pass this pinned vortex line, each element of the pinned vortex line

difuses back to the center of the columnar defect due to the elastic energy and thermal fluctuations. Due to the periodic boundary condition, the moving flux line leaves one side of the system and comes back on the opposite side. This keeps happening until the pinned vortex line depins from the pinning center, which results in the periodicity of the time scale and hence yields the narrow band peak in the power spectrum. Since the vortex line moves very slowly inside the pinning center, it gives the small magnitude of the power spectrum.

Its higher harmonics can be understood as the result of the different time scales. These different time scales can arise from the localized flux line inside two or more columnar pinning centers. Since they are at different locations, they feel different forces. The closer one moves away from the center of the columnar defect at a faster rate while the further one is moving away with a slower rate. As a result, this leads to the repetition of the different time scales τ and hence different velocity fluctuations. This gives rise to the observed harmonics of the narrow band peak. This could be the same explanation for the observed narrow band peaks in the x-direction.

Even though the strong pinning strength for the system with point defect is the same, this behavior is not observed in the system with point defect since each vortex line element of the flux line moves almost independently. Each of them may be trapped inside the pinning center at different locations and feels different forces in different directions while other moving flux lines are passing. This applies to the rest of the system and gives rise to different time scales. These various time scales yield the different frequencies observed in the noise and hence result in the characteristic broadband noise.

In comparison to the system with point defects, the $1/\omega$ scaling behavior is observed for the system with randomly placed columnar defects in the low frequency regime. From our results in the previous section, the higher value of the exponent $\alpha \approx 1.3$ is observed in the system with strong point defects. This behavior of $1/\omega^\alpha$ is obtained in the systems of two- and three-dimensional vortex models [85]. In that work, the change in the exponent is due to the effect of the strength of the applied magnetic field and the dimension of the system. The system with no vortices, or zero field, a number of vortex equals to the number of antivortex, gives the $1/\omega$ scaling behavior. The systems with a nonzero vortex density at both two- and three-dimensions give the $1/\omega^{3/2}$ scaling behavior. The small difference in the value of the exponent of our results show the effect from the defect configurations. Correlated defects gives a larger exponent than the one with uncorrelated defects. The $1/\omega^\alpha$ scaling behavior with $\alpha = 2$ in the system with the weak columnar defect is numerically obtained by Das [109] and similarly observed. This leads to another conclusion that the change in the exponent might come from the effect of the pinning strength, i.e., the strong pinning strength gives the small value of the exponent. However, our results are from a different regime from Ref.[109]. This needs further investigation for the dependence of this value.

Table 4.4: Predicted washboard frequency for columnar defects : x-component

Vortex number (lines)	Lattice constant (b_0)	Velocity (b_0/mcs)	Predicted frequency ω_x	Measured frequency $\omega_x \& \omega_y$
16	101	0.00359	0.000223	0.0038
36	67.4	0.00911	0.000567	0.0038
64	50.5	0.0267	0.00166	0.0038
100	40.4	0.0434	0.00267	0.0038

Table 4.5: Predicted length scale for columnar defects: x-component

Peak	Measured frequency ω_x	Calculated length scales (b_0) for each vortex number (lines)			
		16	36	64	100
1 st	0.0038	5.94	15.06	44.15	71.76
2 nd	0.0075	3.01	7.06	22.37	36.36
3 rd	0.012	1.88	4.77	13.98	22.72
4 th	0.016	1.41	3.58	10.49	17.04
5 th	0.019	1.19	3.01	8.83	14.35
6 th	0.023	0.981	2.49	7.29	11.86

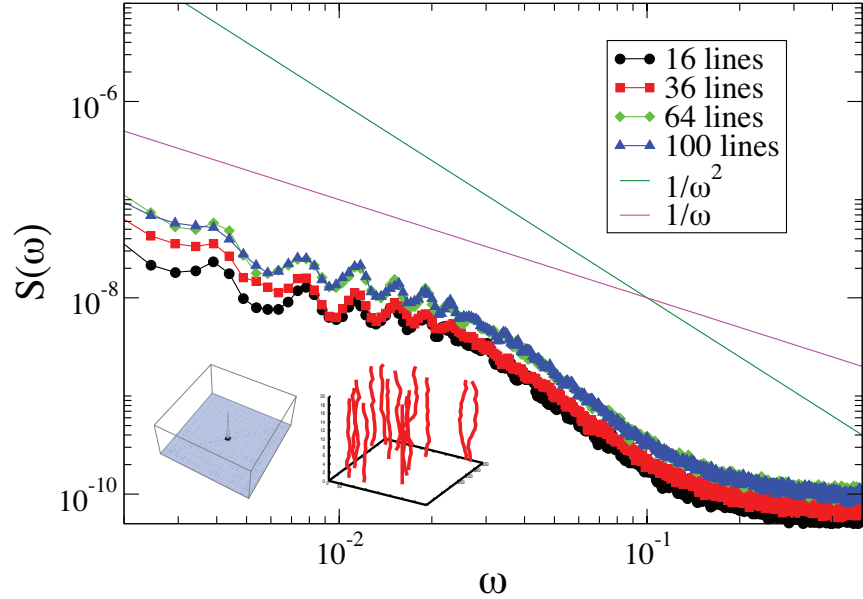


Figure 4.28: Voltage noise in the direction of the driving force (x-direction) for systems with randomly placed columnar defects at various vortex densities. The driving force along the x-axis for each curve is set to be 2.7. Unlike the systems with point defects, the magnitude for each curve increases as the vortex density increases from 16 to 36, 64, and 100, respectively. Surprisingly, the presence of narrowband peaks in these systems does not reflect the periodicity of the moving vortex lines. The flux lines are in the moving liquid or plastic phase, which is supported by the existence of a single peak in the diffraction plot and a plastic vortex structure in a snapshot. Moreover, the frequency for each harmonic for each curve tends to coincide even though the vortices move with different velocity and have different density. This is clearly not the washboard frequency. The presence of the narrow band peaks in this moderate driving force regime indicates the effect due to the strong pinning centers. The time scale that the pinned vortices move across the pinning center is large in comparison to the time scale it takes the flux line to move for one vortex lattice. This process keeps occurring in the system and affects the average velocity, which gives rise to the characteristic narrow band peaks. The higher harmonics are observed due to a faster time scale that the flux lines take to depin. In addition to the narrow band peaks, the $1/\omega$ -like behavior is observed for the noise power in the low frequency regime. The $1/\omega^2$ power law is observed for the intermediate frequency.

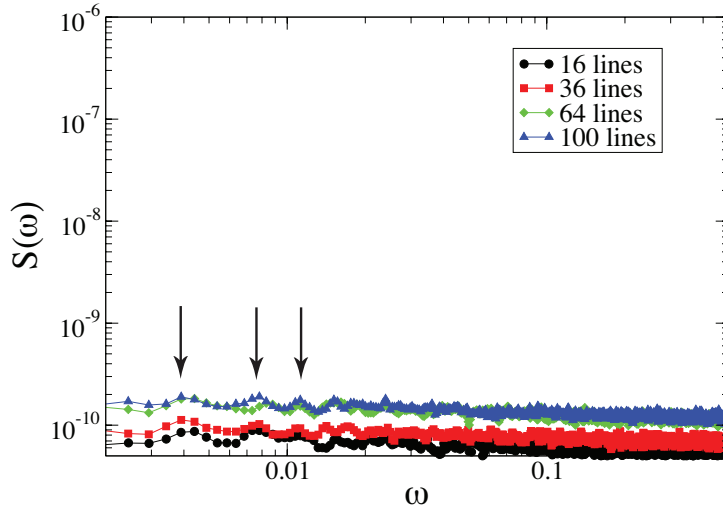


Figure 4.29: Voltage noise in the direction transverse to the driving force (y-direction) for systems with randomly placed columnar defects at various vortex densities. The driving force along the x-axis for each curve is set to be 2.7. Similar to the voltage noise in the x-direction with columnar defects, the magnitude for each curve increases as the vortex density increases from 16 to 36, 64, and 100, respectively. Similar to the results in the x-direction, the presence of narrowband peaks in these systems does not reflect the periodicity of the moving vortex lines. Flux lines are in the moving liquid or plastic phase, which is supported by the existence of a single peak in the diffraction plot and a plastic vortex structure in a snapshot. Moreover, the frequency for each harmonic for each curve tends to coincide even though they have different velocities and vortex densities. This is clearly not the washboard frequency. The reason is similar to the results in the x-direction, i.e., the presence of the fundamental peak and its harmonics is due to the different time scales that the flux lines need to depin. This time scale is comparable to the time scale it takes the flux line to move for one vortex lattice constant. A large number of this process occurs in the system and results in the periodicity of this time scale and hence the presence of the narrow band peaks.

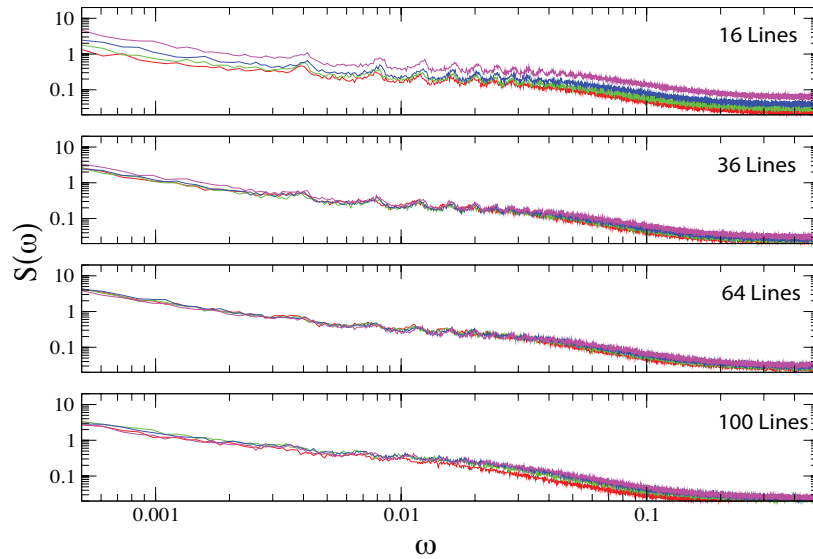


Figure 4.30: Velocity/voltage power spectra for the system with randomly placed columnar defects at various velocities, in the x-direction. From the top to bottom systems with the number of 16, 36, 64, and 100 vortex lines are shown. Narrow band noise peaks are clearly observed in the system of 16 lines and tend to disappear at larger densities of vortex lines. For each density, the magnitude of each peak is increased for increasing velocity (red, green, blue, and pink line, respectively). This indicates the larger velocity fluctuations for increasing vortex density. However, each narrow band noise frequency and their harmonics are approximately equal and independent of velocity and density of vortex lines. This will give the same length scale, which is different from the length scale calculated from the washboard frequency. Moving vortex lines are in the moving plastic or moving liquid phases supported by the single peak in the structure factor and a snapshot of moving flux lines.

Chapter 5

Aging Dynamics

Here an investigation of the aging phenomena in the vortex glass is reported. Many glassy systems exhibit aging phenomena, which have attracted great interest during the past decades. It was misleading that the aging phenomena uniquely characterized glassy systems such as polymer glasses [77], and spin glasses [110]. Recently, it has been realized that aging phenomena can be found in many other systems [31, 78, 111, 112, 113, 114]. Glassy materials provide extremely large relaxation times which are considerably long enough and allow one to be able to investigate aging phenomena. In order to identify or characterize properties of aging phenomena, the slow relaxation must be associated with three other properties. The first one is the power-law behavior of the slow relaxation far from equilibrium towards equilibrium. This power-law relaxation is observed when the time elapsed is between a microscopic time t_{micro} and an equilibration time t_{eq} . The microscopic time is extremely small, i.e., time for a single spin to flip. The equilibration time can be days to years. The second property is the breaking of time-translation invariance of observables such as the autocorrelation or autoresponse functions. The autocorrelation function depends on a waiting time s and an observable time t but not just on the time elapsed $t - s$. The last one is the existence of the dynamical scaling behavior at long times $t/s \gg 1$. Here we investigate the relaxation behavior of the density autocorrelation function upon the change of parameters which include temperature, pinning strength, vortex-vortex interaction range, and defect density.

5.1 Preparation of the System

The system of interacting flux lines from the previous section is used to study aging phenomena in this section. The density autocorrelation function is used to investigate the three properties mentioned above. The system contains 16 flux lines, 320 vortex line elements, with a total number of 22320 weak point defects. The system size is $[x, y, z,] = [\frac{2}{\sqrt{3}} \times 8\lambda, 8\lambda, 20b_0]$ which is smaller by 2λ on the x and y axis than before. The number of layers or the length along the z -axis remains the same. This smaller system size shows no finite size effect due to the sharp cut-off interaction. In the absence of defects, it has been tested that the vortex lines, which are randomly placed in the system

at the beginning, are allowed to equilibrate and form an Abrikosov vortex lattice. The aging phenomenon is expected to occur when systems out-of equilibrium undergo a slow relaxation to equilibrium. The system with weak point defects is chosen since the vortex lines can equilibrate in a finite simulation time. The system would remain in the long-lived metastable states if the system with the columnar defects is used instead.

In order to investigate aging phenomena in this system, vortex lines are prepared in an out-of equilibrium state: vortex lines are placed randomly in the system with weak point defects at the beginning. In order to have a slow dynamics, the temperature is set to 10K from the beginning, $t = 0$, to the rest of the simulation, i.e., no temperature quenching. The vortex lines are allowed to relax during the waiting time s . The density autocorrelation is then measured every 50 MCS from $t = s$ to $t = s + 100000$ MCS.

In order to investigate the breaking of time-translation invariance, the system is allowed to relax during different waiting times ‘ s ’. The density autocorrelation function is then plotted against $t - s$. If the data does not collapse on a single curve, it shows the breaking of time-translation invariance. At large enough waiting times, all curves collapse on a master curve since they are asymptotically reduced to equilibrium.

Finally, the density autocorrelation function is then plotted against t/s in order to display the dynamical scaling behavior. If all the curves collapse on a single curve, it shows the ‘full aging’ or ‘simple aging’. Sometimes the curves slightly deviate from a master curve but can be corrected if the autocorrelation is multiplied by a function of a waiting time. This ‘multiplicative aging’ can be written as

$$\tilde{C}(t, s) \approx s^{-b} f_C\left(\frac{t}{s}\right)$$

This dynamical scaling behavior is expected to occur in the regime where $t, s \gg 1$ and $t - s \gg 1$. The exponent b is obtained by plotting the autocorrelation $C(ms, s)$, where $m = t/s$, against s on a log-log scale. For different values of $m = t/s$, a slope for each plot is approximately equal to a value of $-b$. We measure values of b for several values of $t/s \gg 1$ and then take the average. This method is used in Ref.[115].

The algorithm to generate the density autocorrelation function $\langle n_i(s)n_i(t) \rangle$ is explained as follows. Since the system of interacting vortex lines is initially prepared in the disordered phase, the repulsive vortex interaction causes each flux line to repel each other. After a finite time elapsed, positions of the center of mass of each vortex line may be different from the beginning. The change in the position over time leads to the decay of the autocorrelation function. The interacting vortex lines are randomly placed in the system and allowed to relax from $t = 0$ to $t = s$. The density of the vortex line element is generated by setting a circular area, with a radius equal to one, at positions of each vortex line element at $t = s$. As time elapses, we count the number of this vortex line elements in the circle as the density, i.e., it can be either 0 or 1. This density is represented by $n_i(t)$, where i is the number of the vortex line elements. Therefore, $n_i(t = s)$ is always 1. Due to the repulsive vortex interactions and the random positions of the vortex line elements at the beginning, flux line elements tend to move away from each other and cause a change in their positions. $n_i(t > s)$ can be 0 at a later time if this vortex line element leaves this circle. In the presence of defects, this vortex line element can be trapped inside the defect

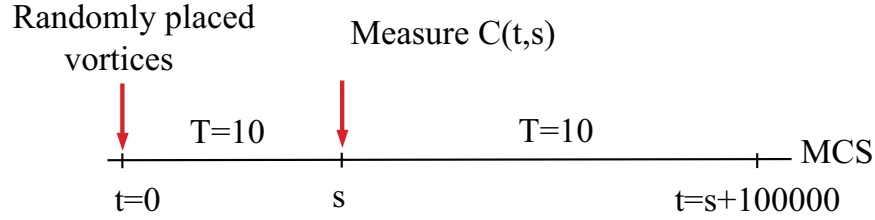


Figure 5.1: Sketch of the density autocorrelation measurement. At $t=0$, vortex lines are brought out of equilibrium by random placement in the system at $T=10\text{K}$ in the presence of weak point defects. The vortex lines are allowed to relax for different waiting times s . The density autocorrelation function is then measured for every 50 MCS from $t = s$ to $t = s + 100000$ MCS.

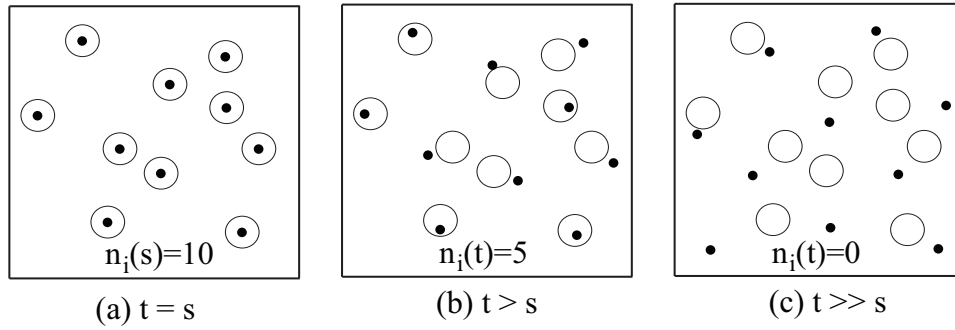


Figure 5.2: Sketch of the vortex line elements (small solid circle) and their unit circles (large circle) at different observation times. At (a) $t = s$, each vortex line element stays inside its own circle and gives a total number of vortex line elements staying inside the circles of $n_i(t = s) = 10$. At later times (b), the repulsive vortex interactions cause vortex line elements to move away from their initial positions (large circle). This results in a smaller occupation number $n_i(t > s) = 5$. At long time (c) $t \gg s$, it is possible that all vortex line elements leave the circle, $n_i(t \gg s) = 0$, which results in a complete decorrelation. For instance, the autocorrelation $n_i(s)n_i(t)$ at these three times is calculated as $C(s, t = s) = 10 \times 10 = 100$, $C(s, t > s) = 10 \times 5 = 50$, and $C(s, t \gg s) = 10 \times 0 = 0$.

over a long time and causes $n_i(t > s)$ to be 1. The product of $n_i(s)n_i(t)$ is calculated for every 50 MCS for the next 100000 MCS. This quantity is then averaged over the different vortex line elements and defect distributions. Fig. 5.2 shows the algorithm for calculating the density autocorrelation function. We have checked the results for different values of the radius of the circle and found that it does not affect the results in the aging regime where $t/s \gg 1$.

5.2 Dynamical Scaling Behavior

We investigate the dynamical scaling behavior by considering a two-time correlation function for a system of interacting vortices in the absence of defects and compare exponents b and λ_c/z with recent results reported in Ref. [31, 116]. Bustingorry [31] studied the aging dynamics by means of numerical simulations of the London-Langevin model of the interacting vortex lines in the vortex glass regime, which occurs at low temperatures. Values for the exponent b are reported from the scaling of the two-time mean square displacement. Romá [116] reported both exponents b and λ_c/z by means of Monte Carlo simulations of the three-dimensional gauge glass model at the critical temperature.

5.2.1 A Single Flux Line

Before we investigate the behavior of the dynamical exponents, we first study the non-equilibrium dynamics for the system of a single flux line in a clean superconductor at low temperature. This can be done by setting the pinning strength and the energy due to the vortex interactions to zero. It is observed that the autocorrelation function for different waiting times as a function of $t - s$ at $T=10$ slowly decays and collapses on a single curve while decaying to small values. The decay is due to the presence of small thermal fluctuations which causes a straight flux line to wiggle over time. This nice collapse of the data shows the presence of time translation invariance, i.e., the system is in equilibrium with its environment and does not age. This is shown in Fig. 5.3. The system undergoes the exponential decay at short times and then displays power-law behavior at long times $t > 10^3$ MCS. Fig.5.4a is a plot of the autocorrelation function on the normal-log scale. It shows a linear behavior approximately up to $t < 1000$ MCS, which indicates the exponential decay. Fig.5.4b shows a linear behavior on a log-log scale at larger times, which describes the existence of the power-law decay.

We do not measure the exponent b and λ_c/z of the single flux line due to the absence of time-translation invariance in the density autocorrelation. However, Bustingorry [31] recently investigated the behavior of the two-time mean square displacement and the two-time density-density correlation function for a system of a single flux line with weak disorder at various temperatures below the critical temperature. It was reported that the aging phenomenon occurs at very low temperature and gives values of the exponent b between 0.25 and 0.5 for increasing temperature. In similar systems but without disorder, we did not observe the aging phenomena in these two quantities at $T=10$. We have also checked for the behavior of these two quantities for a system of a single flux line in the presence of disorder. It is observed that the presence of the defect slightly affects the dynamics of the flux line. For increasing waiting time, the autocorrelation decays slightly slower at small time elapsed but collapses on a single curve at long times, where the aging phenomena is expected to occur. We will show later that the values of the exponent b measured in this work for systems of interacting vortices in the presence of defects are significantly different from the results obtained in Refs.[31, 116].

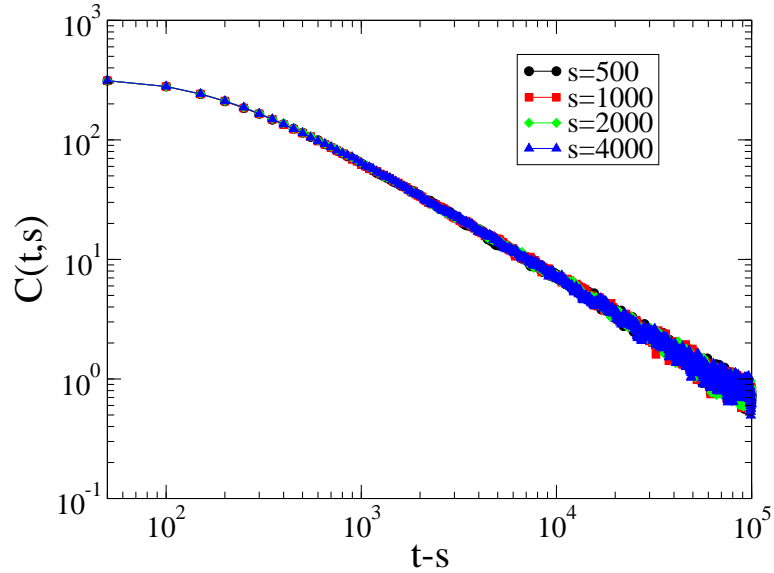


Figure 5.3: Two-time density-density correlation for noninteracting vortices with no disorder at $T = 10$. The correlation decays due to thermal fluctuations. The data collapse perfectly, which shows that they are independent of the waiting time s . A dependence on the time difference $t - s$ shows that time-translation invariance holds in this system. The data comprises an average over 315 defect distributions.

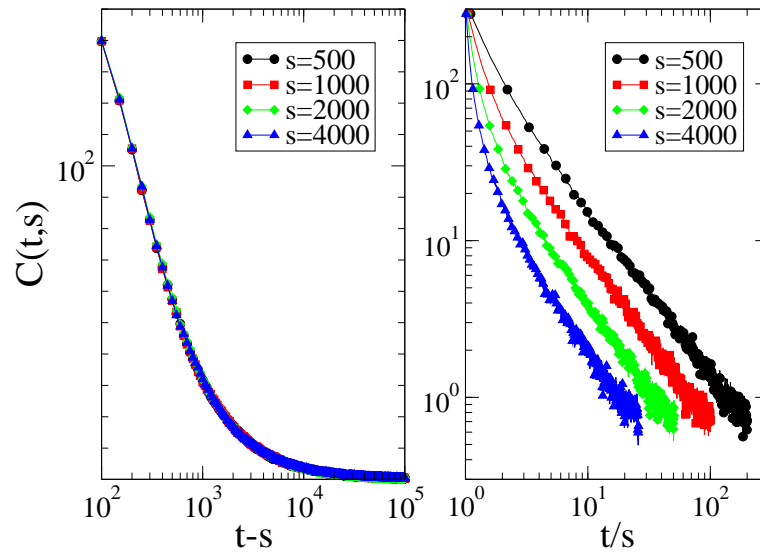


Figure 5.4: Two-time density-density correlation for noninteracting vortices with no disorder at $T = 10$ as a function of (a) $t - s$ with a log scale on the x-axis and a normal scale on the y-axis and (b) t/s on a log-log scale. The data in (a) shows the exponential decay of the autocorrelation up to 1000 MCS. It becomes a power-law decay at longer times as shown in (b).

5.2.2 Varying Pinning Strength

Next, we study the system of interacting vortices in absence of defects. We set the interaction range to $\lambda_{ab} = 35$, temperature $T=10$, average distance between defects $dist = 9.0$, and the pinning strength $pin=0$. Flux lines are randomly placed in the system at $t = 0$ and allowed to relax for a waiting time s . The density-density autocorrelation function is measured at $t = s$ for every 50 MCS until the end of the simulation. As a result, the data for the autocorrelation when plotted against $t - s$ do not collapse onto each other and depend on both t and s . This is a clear evidence that the time-translation invariance of the autocorrelation is broken.

Similar to the system of a single line, it undergoes an exponential decay at small times followed by a power-law decay at larger times. Another difference is that the system decays at a faster rate at intermediate times than at longer times. The faster rate arises because of the presence of the stronger repulsive vortex interactions. Due to the random positions of the flux lines at the beginning, some of them may be too close to each other and encounter a stronger repulsive force. As shown in Fig. 5.5, systems with a longer waiting time decay slower than systems with a smaller waiting time as expected. As shown in Fig.5.6, the plots of autocorrelation against t/s tend to have a power-law relaxation for $t/s \gg 1$ MCS. For small waiting times, the autocorrelation at small t/s strongly deviates from a master curve which indicates the presence of fast relaxation regime.

Since our data are extremely noisy, it is difficult to measure the exponent b . In this case, we extract the exponent b by plotting the autocorrelation $s^b C(t, s)$ against t/s with various values of b and see which value of b fits best. The waiting times of $s = 500, 1000, 2000$, and 4000 MCS are selected since they show a nice collapse of the data for long times $t/s \gg 1$. Our data show a qualitative scaling with $b \approx 0.2$ and $\lambda_c/z \approx 0.396$ for $t/s = 20$. This multiplicative scaling form is chosen due to the fact that the autocorrelation function does not show a plateau for larger s [31]. An additive or simple aging scaling with the exponent $b = 0$ is expected if a plateau is observed. From these two systems, it is clear that the multiplicative aging is stronger for a smaller b . A smaller λ_c/z explains the slower relaxation at long times. In this case, the vortex lines are initially placed at random positions. The strong repulsive interactions cause some of the flux lines to repel each other at early times, which results in the fast dynamics. At longer times, the average spacing between each flux line is of equal magnitude while trying to form Abrikosov vortex lattice. The dynamics becomes much slower in this regime, where the aging phenomena is observed. This gives rise to a small value of λ_c/z .

We also investigate the effect of the pinning centers and vortex interactions on these exponents. First, we are interested in a regime of usual interaction range $\lambda_{ab} = 35$, $T=10$, $dist = 9$ with various pinning strengths of $pin = 0.0, 0.01, 0.02, 0.05$. Fig.5.5, Fig.5.7, Fig.5.9, and Fig.5.11 show the plots of the autocorrelation as a function of $t - s$ for $pin = 0.0, 0.01, 0.02$, and 0.05 , respectively. It is clearly seen that time translation invariance is broken. As the pinning strength increases, we observe that the autocorrelation function for different waiting times tends to pile up closer to each other, which causes the time-translation invariance to disappear. Naively, the increase of the pinning strength causes the systems to reach equilibrium faster.

By plotting the autocorrelation function as a function of t/s for systems with various pinning strengths, it is observed that systems with stronger pinning strengths decay slower than systems with weaker pinning strengths. Systems with a waiting time of $s = 500$ for various pinning strengths are shown in Fig.5.29. As explained in Ref.[117], we can obtain the value of the dynamical exponent b by plotting $C(ms, s)$ against s for different values of $m = t/s$ and the waiting times on a log-log scale. This can be done by first plotting $C(t, s)$ over against t/s . As shown in Fig.5.4b, the curves do not show any collapse. Next, we select a specific value of t/s and read off the value of the autocorrelation function for different waiting times. We plot these values against the waiting time and observe a straight line. Its slope is approximately equal to $-b$. We repeat this for several values of $m = t/s$ and then take the average to get a better statistics for the value of b . It is observed that the value of the exponent b increases with increasing the pinning strength: 0.20, 0.24, 0.452, and 0.751. Fig.5.8a, Fig.5.10a, and Fig.5.12a show the plot of $C(ms, s)$ vs s for $pin = 0.01, 0.02$, and 0.05 . With these values of b , Fig.5.8b, Fig.5.10b, and Fig.5.12b show that the corrected autocorrelation function $s^b C(t, s)$ when plotted over against t/s nicely collapse on a single curve.

Up to this point, our results confirm the existence of the aging phenomena by showing the presence of the slow power-law relaxation, breaking of the time translation invariance, and dynamical scaling behavior. Our results are different from the behavior of b observed in [31], which reports smaller values of $b < 0.5$ for increasing pinning strength. The larger values of b correspond to slower dynamics which is observed in our results. It is slower in the sense that it decays to zero at slower rate. The presence of the vortex interactions and pinning centers slows down the dynamics of vortex lines at the long time regime as mentioned earlier. As the vortex lines try to move away from each other during the small time regime, some of the vortex elements get trapped by the pinning centers. If the pinning strength is very weak, the vortex interactions still dominate the dynamics and the system relaxes slower to its equilibrium state. The vortex elements get temporarily trapped, but depin themselves later. This actually slows down the dynamics. The systems can still reach the equilibrium Abrikosov vortex lattice or Bragg glass, but take this process much longer time. However, for much stronger pinning strengths, the vortex elements are trapped inside the pinning centers for much longer time, which results in the nonequilibrium vortex glass. This would cause the dynamics of the system to be faster in the sense that all motions stop at shorter times. Flux line elements can only wiggle while they are pinned inside the pinning centers. Again, the dynamics is described to be slower due to the slower decay of the autocorrelation function.

Another important dynamical exponent can be obtained by plotting the autocorrelation function against t/s . Since the autocorrelation function undergoes a power-law decay at long times, $f_c(t, s) (t/s)^{-\lambda_c/z}$, its slope measures the exponent λ_c/z . We measure this slope from the data with $s = 500$ from $t/s = 21$ to $t/s = 200$, where it shows the power-law behavior. The value of the exponent λ_c/z increases for increasing pinning strength: 0.396, 0.461, 0.676, and 0.899. As shown in Fig.5.29, the larger values of this exponent indicate the slower decorrelation of the autocorrelation function. This figure shows the data for different pinning strengths for $s = 4000$. The reason is similar to what is explained for the value of the exponent b . At larger waiting times, more vortex elements get trapped

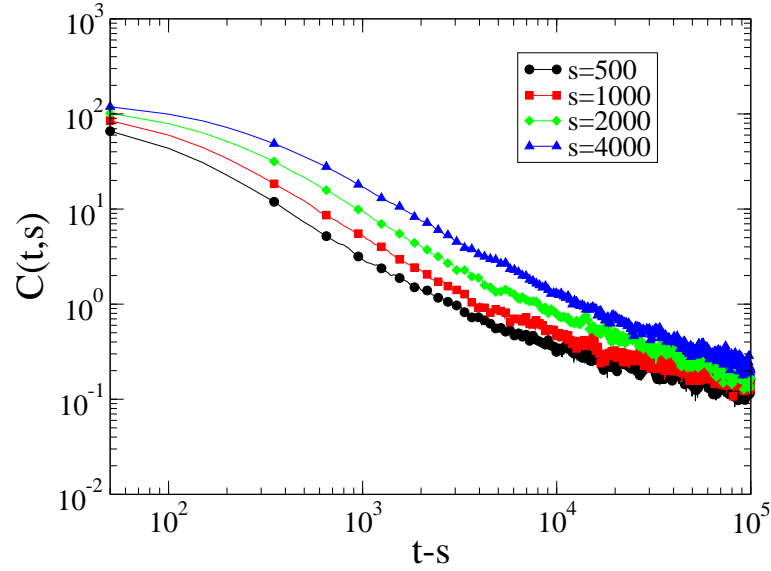


Figure 5.5: Two-time density-density autocorrelation function as a function of $t - s$ for interacting vortices without disorder at $T = 10$ and $\lambda = 35b_0$. The data for waiting times $s=500, 1000, 2000,$ and 4000 MCS do not collapse on each other. Each curve depends on an observation time t and a waiting time s , which shows that time-translation invariance is broken in this system. Systems with larger waiting times decorrelate slower than systems with smaller waiting times. The plot shows changes in the slope at longer times indicating that systems decay at slower rate at long times. The data comprises an average over 1475 defect distributions.

inside pinning centers as we start to measure the autocorrelation function. According to our method to measure the autocorrelation function, a larger number of vortex line elements are pinned inside the pinning centers for longer waiting times. This results in larger values of the autocorrelation function for larger waiting times, which corresponds to larger values of λ_c/z .

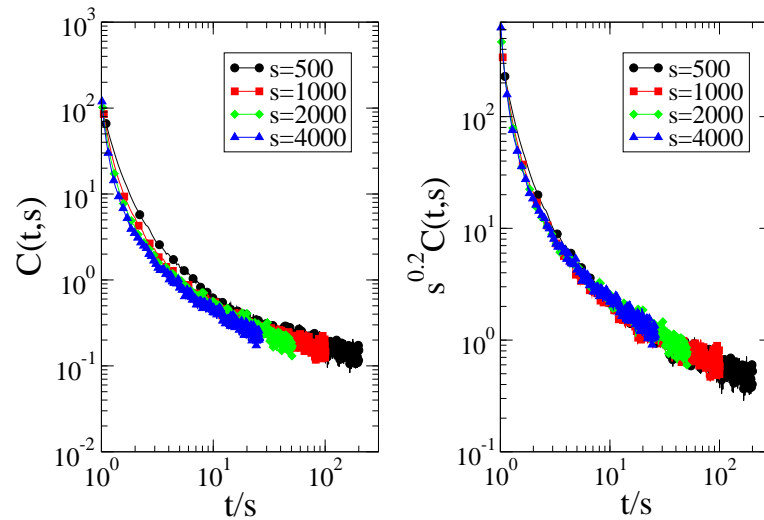


Figure 5.6: Two-time density-density autocorrelation function as a function of t/s for interacting vortices without disorder at $T = 10$ and $\lambda = 35b_0$. The data are for waiting times $s=500, 1000, 2000,$ and 4000 MCS. (a) The curves nearly collapse on each other for large values of t/s . (b) The curve qualitatively collapse on each other when the scaling function is corrected by $s^{0.2}C(t,s)$. The value of the exponent is obtained by plotting the curves for several values of b . It is found that the value of 0.2 gives qualitatively nice collapse of the data. This indicates the presence of simple aging behavior. The data comprises an average over 1475 defect distributions.

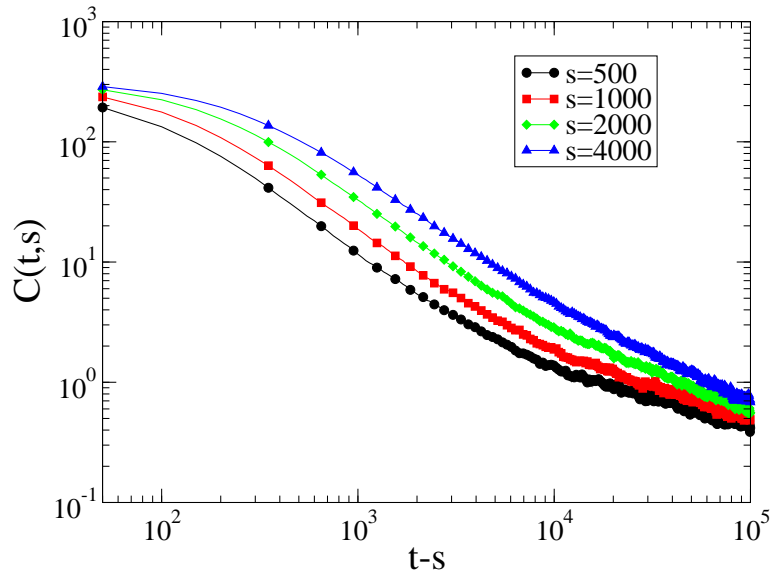


Figure 5.7: Two-time density-density autocorrelation function as a function of $t - s$ for interacting vortices with disorder at $T = 10$, $\lambda = 35b_0$, and pinning strength 0.01. The data for waiting times $s=500$, 1000, 2000, and 4000 MCS do not collapse on each other. The system with a larger waiting time decorrelates slower than the system with a smaller waiting time. In comparison to the system without defects above, the system with defects tends to decorrelate slower and is less noisy at long times. The data comprises an average over 815 defect distributions.

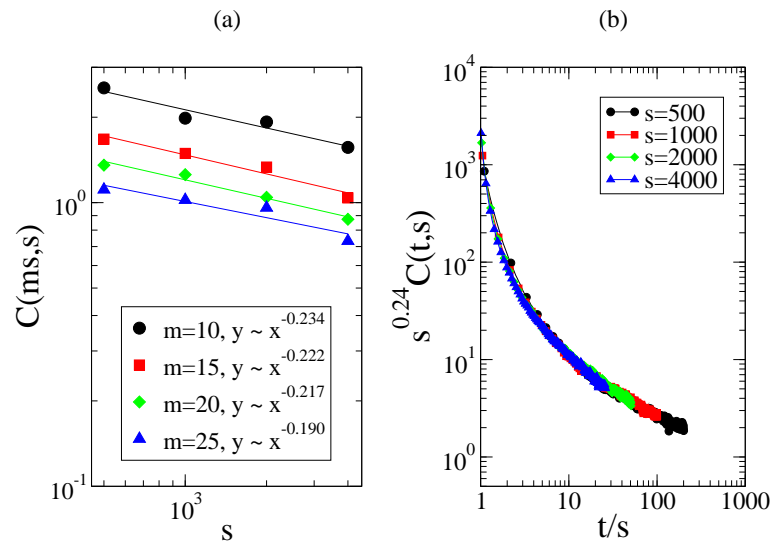


Figure 5.8: (a) Two-time density-density autocorrelation function as a function of s for interacting vortices with disorder at $T = 10$, $\lambda = 35b_0$, pinning strength 0.01, and different values of m . A regression analysis is performed for $m = t/s = 10, 15, 20$, and 25 and gives the slopes of $-0.234, -0.222, -0.217$, and -0.190 . The data is extremely noisy and large fluctuations of the data are present at long times. (b) Based on the measured slopes, the data collapse better for $b = 0.24$, which is higher than the average of the measured values.

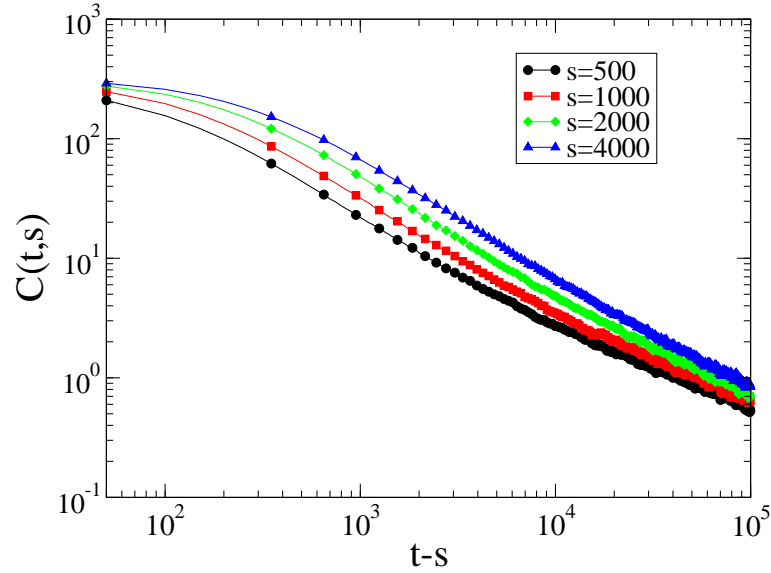


Figure 5.9: Two-time density-density autocorrelation function as a function of $t - s$ for interacting vortices with disorder at $T = 10$, $\lambda = 35b_0$, and pinning strength 0.02. The data for waiting times $s=500, 1000, 2000,$ and 4000 MCS do not collapse onto each other. The autocorrelation function behaves in a similar manner as in Fig.5.7, but tends to decorrelate slower. The data comprises an average over 700 defect distributions.

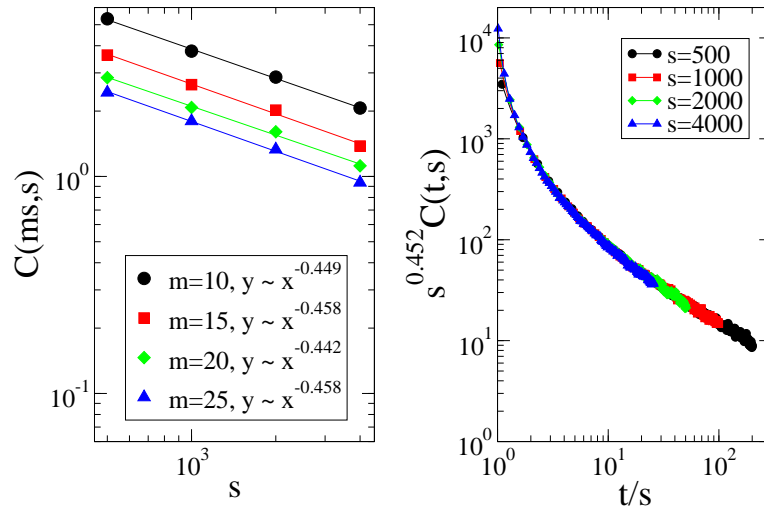


Figure 5.10: (a) Two-time density-density autocorrelation function as a function of s for interacting vortices with disorder at $T = 10$, $\lambda = 35b_0$, pinning strength 0.02, and different values of m . A regression analysis is done for $m = t/s = 10, 15, 20,$ and 25 at long times and gives the slopes of $-0.449, -0.458, -0.442,$ and -0.458 . The average of these values gives the exponent $b \approx 0.452$. (b) The data nicely collapse for $b = 0.452$.

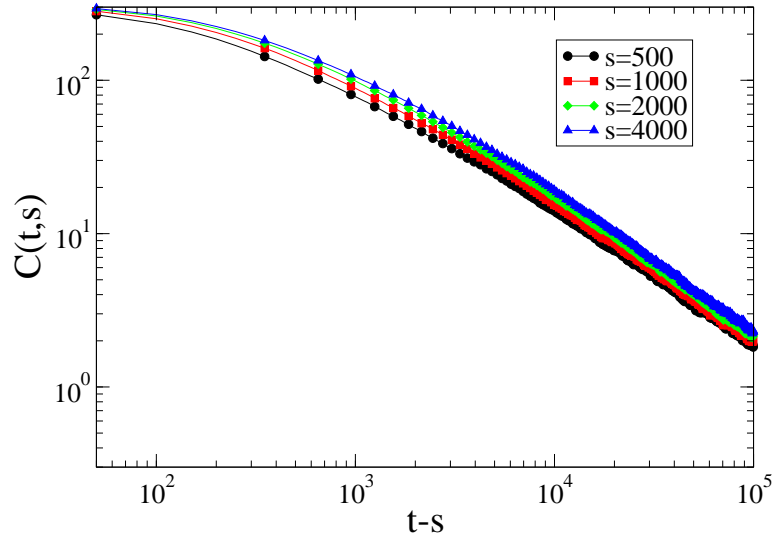


Figure 5.11: Two-time density-density autocorrelation function as a function of $t - s$ for interacting vortices with disorder at $T = 10$, $\lambda = 35b_0$, and pinning strength 0.05. The data for waiting times $s=500, 1000, 2000,$ and 4000 MCS do not collapse on each other. All curves shift up closer to the curve for large waiting time. The change in slope at long times disappears. The data comprises an average over 500 defect distributions.

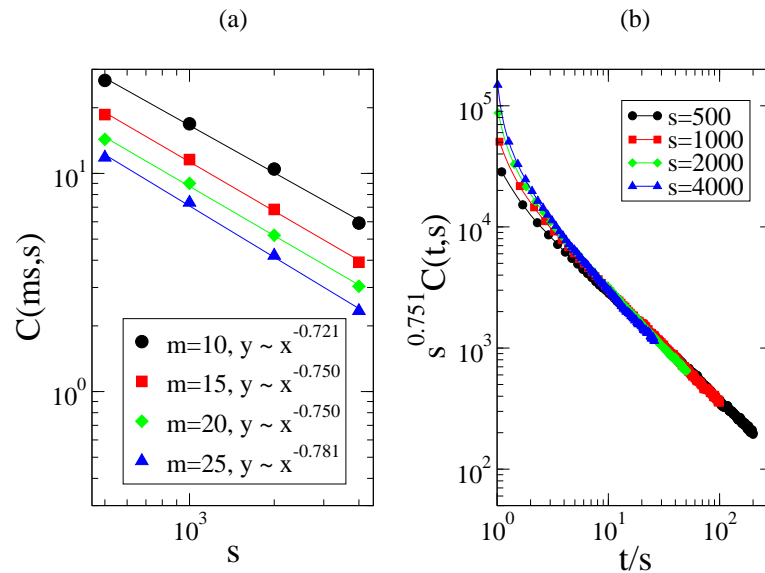


Figure 5.12: (a) Two-time density-density correlation as a function of s for interacting vortices with disorder at $T = 10$, $\lambda = 35b_0$, pinning strength 0.05, and different values of m . Regression analysis is done for $m=10, 15, 20,$ and 25 and gives the slope of $-0.721, -0.750, -0.750,$ and -0.781 . The average of the values give the exponent $b \approx 0.751$. (b) The data nicely collapse for $b = 0.751$ at long times. The data for smaller waiting times strongly deviate from a master curve at small times indicating the presence of fast dynamics at the beginning of the measurement.

5.2.3 Varying Interaction Range

After we start with random positions of the flux lines, in order to have the system out of equilibrium, the repulsive interactions act as the driving force to drive the system to equilibrium. Some of the flux lines move at faster rate at the beginning if they are located close to each other. As the time elapses, one would expect that the repulsive forces due to the nearby flux lines become smaller. This results in a slower dynamics as the time elapses. For various interaction ranges, we choose to study the system with the pinning strength of 0.02, $T=10$, and penetration lengths of 10, 20, 25, and 35. Our results from the previous section for $\lambda_{ab} = 35$ give nearly perfect collapse of the autocorrelation when plotted over against t/s with $b=0.452$.

Fig.5.17, Fig.5.15, Fig.5.13, and Fig.5.9 show the plots of the autocorrelation for increasing interaction range. Similar to the effect due to the pinning strength, we found that the curves shift closer to each other for decreasing interaction range. The change in the slope at long times also disappears for decreasing interaction range. The breaking of time-translation invariance is relevant for the systems with larger interaction range. For the system with $\lambda_{ab} = 10$, we observed that the time-translation is slightly broken up to $t = 2 \times 10^4$. The data collapse at larger time indicating that the aging phenomena tend to disappear.

Fig.5.18a, Fig.5.16a, Fig.5.14a, and Fig.5.10a show the plots of the autocorrelation function $C(ms, s)$ against the waiting time s . The exponent b is extracted from the slope for each value of $m = t/s$. It is observed that the values of the exponent b increase for decreasing interaction range: 0.452, 0.645, 0.688, and 0.872. Fig.5.18b, Fig.5.16b, Fig.5.14b, and Fig.5.10b show the plots of the autocorrelation $s^b C(t, s)$ as a function of t/s . The curves nicely collapse onto a single curve for $t/s \gg 1$. For this case, the dynamics becomes slower for decreasing interaction range since the repulsive interaction is weaker. At the beginning of the simulation, flux lines in the system with smaller interaction range move away from each other at a slower rate. Since the dynamics is slower, the pinning potential becomes more effective. For a specific pinning strength, flux lines with smaller interaction range can be trapped inside pinning centers longer than those with larger interaction range. This causes the autocorrelation to decay slowly and gives larger values of b . Since we have discussed that the exponent λ_c/z behaves in the similar manner as the exponent b , we observed the smaller values of the exponent λ_c/z : 0.961, 0.828, 0.781, and 0.676 for increasing interaction range. The data for the largest waiting time of $s = 4000$ for various interaction ranges are compared and shown in Fig.5.30. The data slightly deviate from each other and show the trend of decreasing exponents for increasing interaction range.

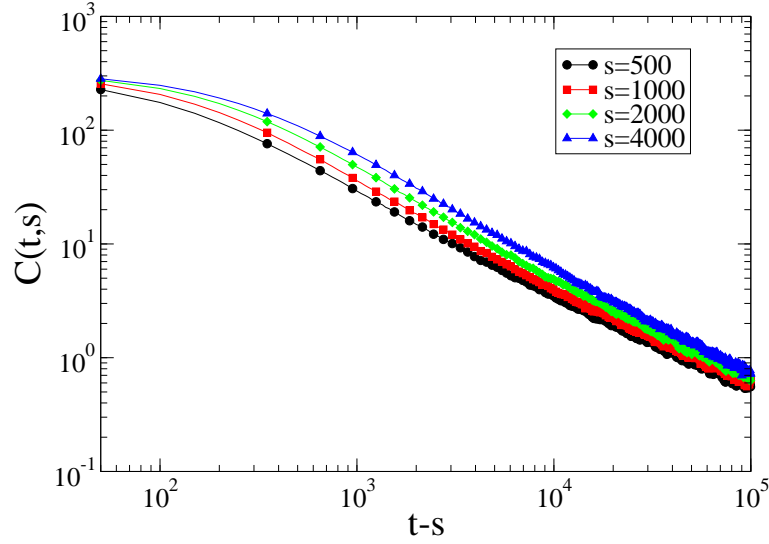


Figure 5.13: Two-time density-density correlation as a function of $t - s$ for interacting vortices with disorder at $T = 10$, $\lambda = 25b_0$, and pinning strength 0.02. The data for waiting times $s=500$, 1000, 2000, and 4000 MCS do not collapse onto each other. The system with a larger waiting time decorrelates slower than the system with smaller waiting time. It decays faster than the system with an interaction range of $35b_0$. All curves shift up closer to the curve for large waiting time. The data comprises an average over 770 defect distributions.

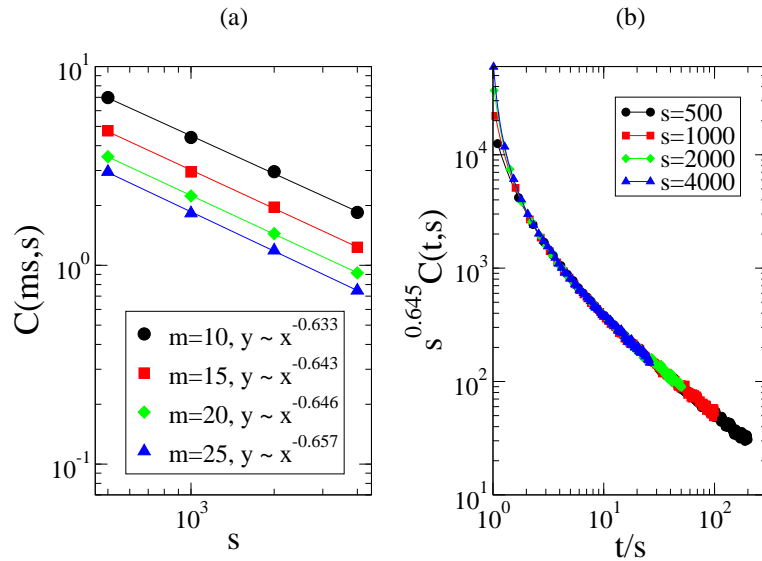


Figure 5.14: (a) Two-time density-density correlation as a function of s for interacting vortices with disorder at $T = 10$, $\lambda = 25b_0$, pinning strength 0.02, and different values of m . Regression analysis is done for $m=10$, 15, 20, and 25 and gives the slope of -0.633 , -0.643 , -0.646 , and -0.657 . The average of the exponent $b \approx$ is 0.645. (b) The data collapse qualitatively for $b = 0.645$ at long times.

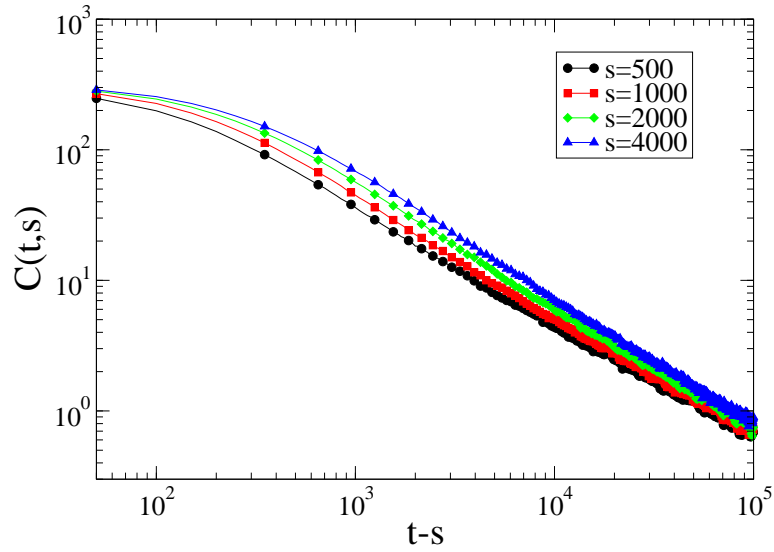


Figure 5.15: Two-time density-density correlation as a function of $t - s$ for interacting vortices with disorder at $T = 10$, $\lambda = 20b_0$, and pinning strength 0.02. The data for waiting times $s=500$, 1000, 2000, and 4000 MCS do not collapse onto each other. The system with a larger waiting time decorrelates slower than the system with smaller waiting time. It decays faster than the system with an interaction range of $35b_0$. All curves shift up closer to the curve for large waiting time. The data comprises an average over 500 defect distributions.

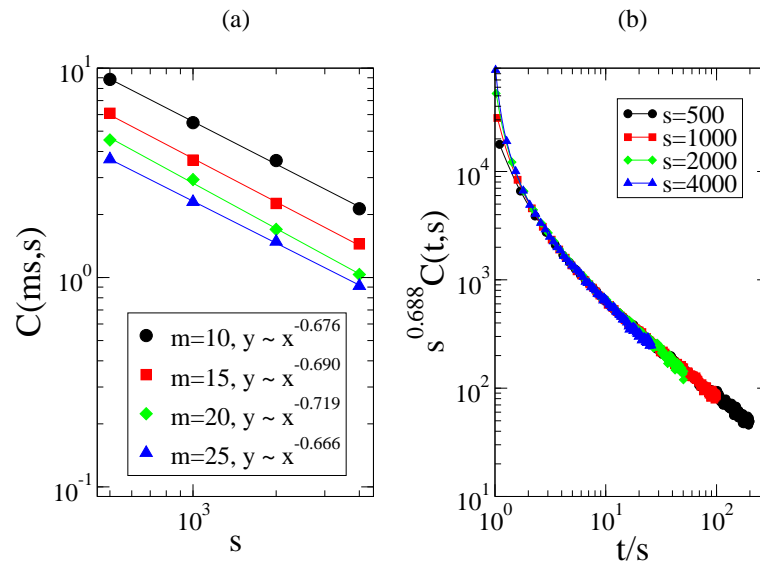


Figure 5.16: (a) Two-time density-density correlation as a function of s for interacting vortices with disorder at $T = 10$, $\lambda = 20b_0$, pinning strength 0.02, and different values of m . Regression analysis is done for $m=10$, 15, 20, and 25 and gives the slope of -0.676, -0.690, -0.719, and -0.666. The average of the values gives the exponent $b \approx 0.688$. (b) The data nicely collapse for $b = 0.688$ at long times.

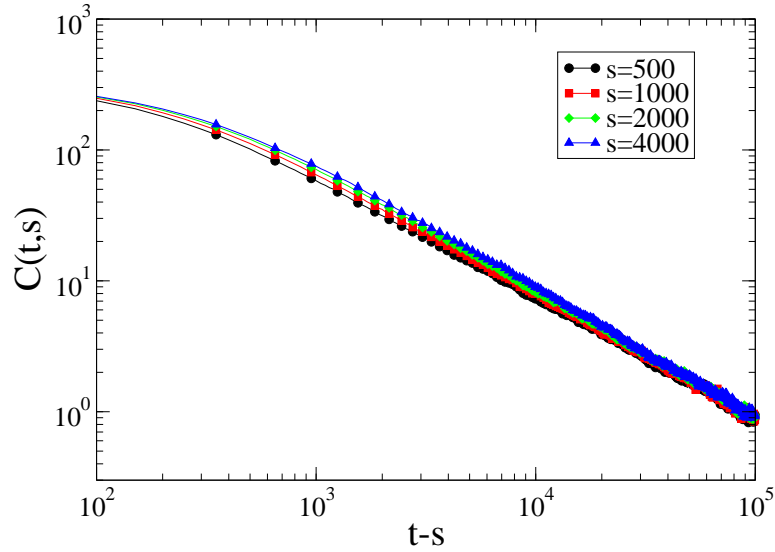


Figure 5.17: Two-time density-density correlation as a function of $t - s$ for interacting vortices with disorder at $T = 10$, $\lambda = 10b_0$, and pinning strength 0.02. The data for waiting times $s=500$, 1000, 2000, and 4000 MCS do not collapse onto each other. The system with a larger waiting time decorrelates slower than the system with smaller waiting time. It decays faster than the system with an interaction range of $35b_0$ and $20b_0$. All curves shift up closer to the curve for large waiting time. The data comprises an average over 500 defect distributions.

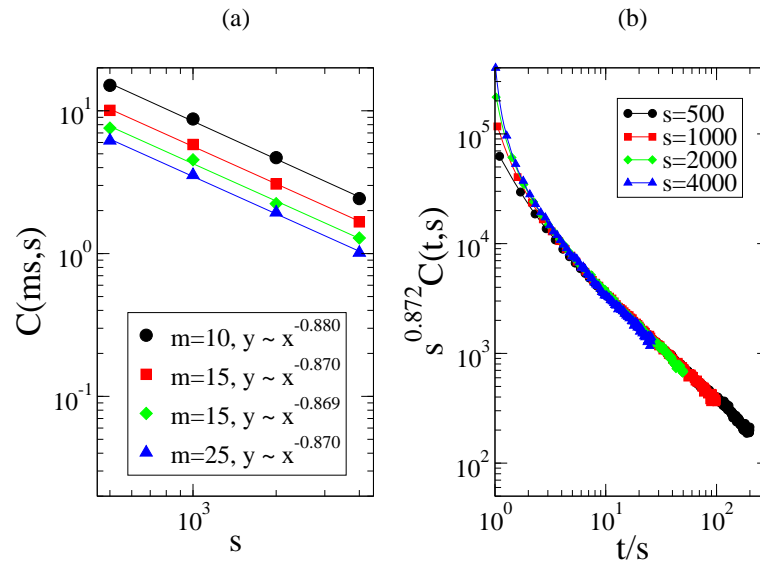


Figure 5.18: (a) Two-time density-density correlation as a function of s for interacting vortices with disorder at $T = 10$, $\lambda = 10b_0$, pinning strength 0.02, and different values of m . Regression analysis is done for $m=10$, 15, 20, and 25 and gives the slope of -0.880, -0.870, -0.869, and -0.870. The average of the values gives the exponent $b \approx 0.872$. (b) The data nicely collapse for $b = 0.872$ at long times.

5.2.4 Varying Temperature

Next, we investigate the effect of the temperature on the aging dynamics. We expect that the autocorrelation would decay faster in systems with stronger thermal fluctuations. Fig.5.9, Fig.5.19, and Fig.5.21 show the plots of the autocorrelation as a function of $t - s$ for temperatures of 10, 20, and 50. As expected, the increase in temperature causes the dynamics to be faster causing the autocorrelation for different waiting times to shift closer to each other for increasing temperature. The change in the slope at long times still present at all temperatures studied since thermal fluctuations promotes faster dynamics. As mentioned earlier in previous sections, the change in the slope at long times occurs when the autocorrelation decorrelates faster. It was reported that temperatures slightly affect the values of the exponent b of the mean square displacement [31] as long as it is well below the critical temperature.

We study the system of a fixed interaction range of $35b_0$, $dist = 9$, and a pinning strength of 0.02 at $T=10, 20$, and 50. These temperatures are well below the experimental critical temperature of $T_c \approx 90$. Fig.5.10a, Fig.5.20a, and Fig.5.22a show the measurement of b for increasing temperatures. We found that the values of exponent b are slightly affected for increasing temperatures: 0.452, 0.436, and 0.450. Since higher temperatures cause larger fluctuations in the system, it becomes more difficult to obtain less noisy data and hence a value of b . Fig.5.10b, Fig.5.20b, and Fig.5.22b show that the data qualitatively collapse on a single curve. However, the values of the exponent λ_c/z reveals better statistics. It slightly decreases for increasing temperature: 0.676, 0.616, and 0.583. The dynamics of the system becomes faster for increasing temperature since the higher temperature directly increases the transition rate or the probability for a vortex line element to move to a new state. Fig.5.31 shows the autocorrelation at different temperatures for the systems with the largest waiting time $s = 4000$, which can be seen that the system at higher temperatures decay faster than the one at lower temperatures. However, thermal fluctuations become stronger for the system at higher temperatures and longer times $t/s \gg 1$. This results in the large fluctuations in the value of the exponent b .

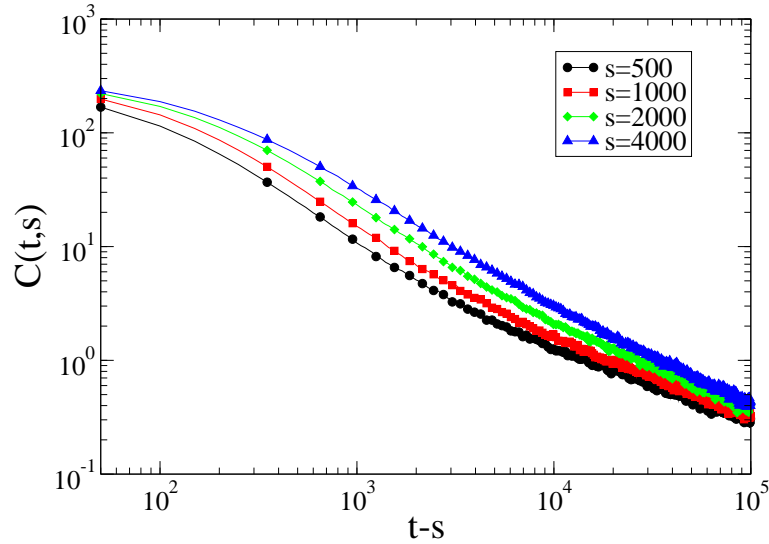


Figure 5.19: Two-time density-density correlation as a function of $t - s$ for interacting vortices with disorder at $T = 20$, $\lambda = 35b_0$, and pinning strength 0.02. The data for waiting times $s=500$, 1000, 2000, and 4000 MCS do not collapse onto each other. The system with a larger waiting time decorrelates slower than the system with smaller waiting time. It decays faster than the system at temperature $T = 10$. All curves shift up closer to the curve for large waiting time. The data comprises an average over 900 defect distributions.

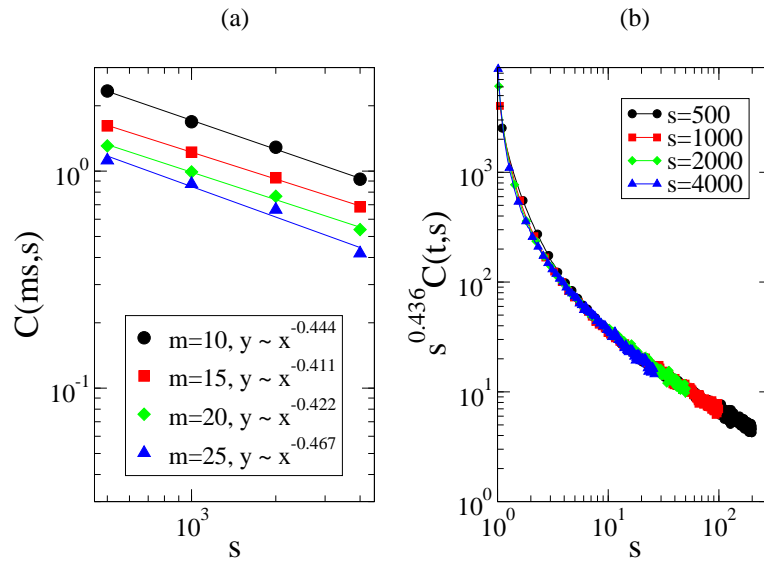


Figure 5.20: (a) Two-time density-density correlation as a function of s for interacting vortices with disorder at $T = 20$, $\lambda = 35b_0$, pinning strength 0.02, and different values of m . Regression analysis is done for $m=10$, 15, 20, and 25 and gives the slope of -0.444, -0.411, -0.422, and -0.467. (b) The data nicely collapse for $b = 0.436$ at long times.

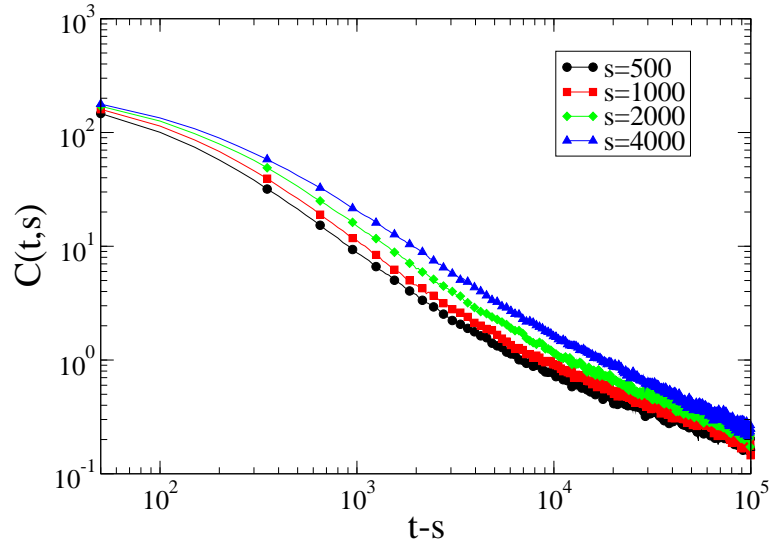


Figure 5.21: Two-time density-density correlation as a function of $t - s$ for interacting vortices with disorder at $T = 50$, $\lambda = 35b_0$, and pinning strength 0.02. The data for waiting times $s=500$, 1000, 2000, and 4000 MCS do not collapse onto each other. The system with a larger waiting time decorrelates slower than the system with smaller waiting time. It decays faster than the system at temperature $T = 10$ and $T = 20$. All curves shift up closer to the curve for large waiting time. The data comprises an average over 950 defect distributions.

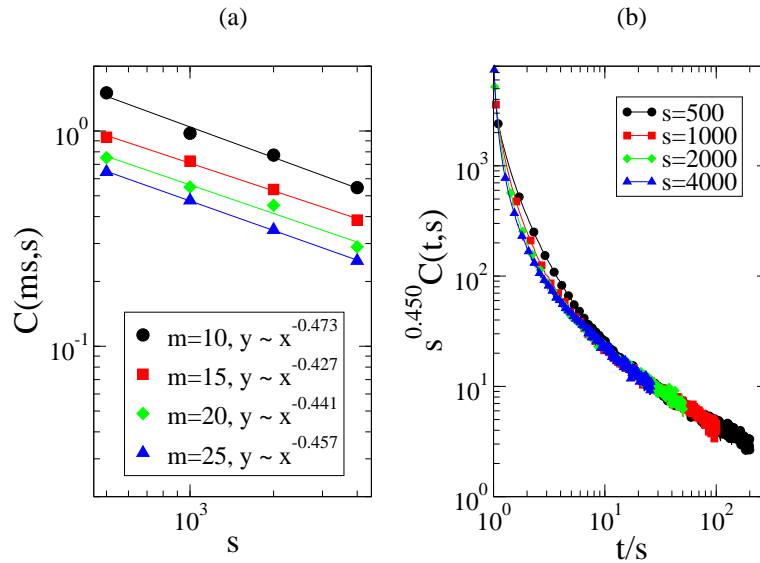


Figure 5.22: (a) Two-time density-density correlation as a function of s for interacting vortices with disorder at $T = 50$, $\lambda = 10b_0$, pinning strength 0.02, and different values of m . Regression analysis is done for $m=10$, 15, 21, and 25 and gives the slope of -0.473, -0.427, -0.441, and -0.457. (b) The data nicely collapse for $b = 0.450$ at long times.

5.2.5 Varying Defect Density

Finally, we investigate the effect of the defect density on the exponent b and λ_c/z for a fixed interaction range $35b_0$, $T=10$, and a pinning strength 0.02. We study systems with the average spacing between each defect of $9b_0$, $12b_0$, $15b_0$, and $20b_0$, i.e., the pinning density decreases as the average spacing increases. We expect that the systems would decorrelate slower if the defect density becomes higher. Fig.5.9, Fig.5.23, Fig.5.25, and Fig.5.27 show the plots of the autocorrelation for decreasing defect density as a function of $t - s$. It clearly shows the breaking of the time-translation invariance at all of the defect densities studied in this work. The change in the slope at long times is present in all systems that we studied. This indicates the presence of fast dynamics of the flux lines. Fig.5.10a, Fig.5.24a, Fig.5.26a, and Fig.5.28a show the measurement of b for different pinning density. As expected, the dynamics becomes faster as the pinning density decreases as shown in Fig.5.32 and causes the values of b to decrease. The values of exponent b are found to be 0.452, 0.352, 0.299, and 0.26 for decreasing defect density. The values of the exponent λ_c/z also decreases for decreasing pinning density: 0.676, 0.564, 0.555, and 0.527. Fig.5.10b, Fig.5.24b, Fig.5.26b, and Fig.5.28b show the nice collapse of the data on a single curve when $s^b C(t, s)$ is plotted over against t/s .

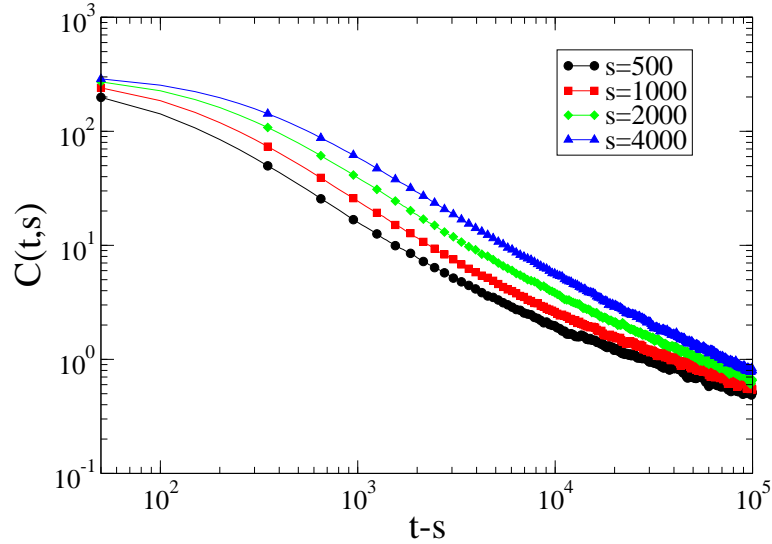


Figure 5.23: Two-time density-density correlation as a function of $t - s$ for interacting vortices with disorder at $T = 10$, $\lambda = 35b_0$, pinning strength 0.02, and $dist = 12$. The data for waiting times $s=500, 1000, 2000$, and 4000 MCS do not collapse onto each other. The system with a larger waiting time decorrelates slower than the system with smaller waiting time. All curves shift up closer to the curve for large waiting time. The data comprises an average over 1150 defect distributions.

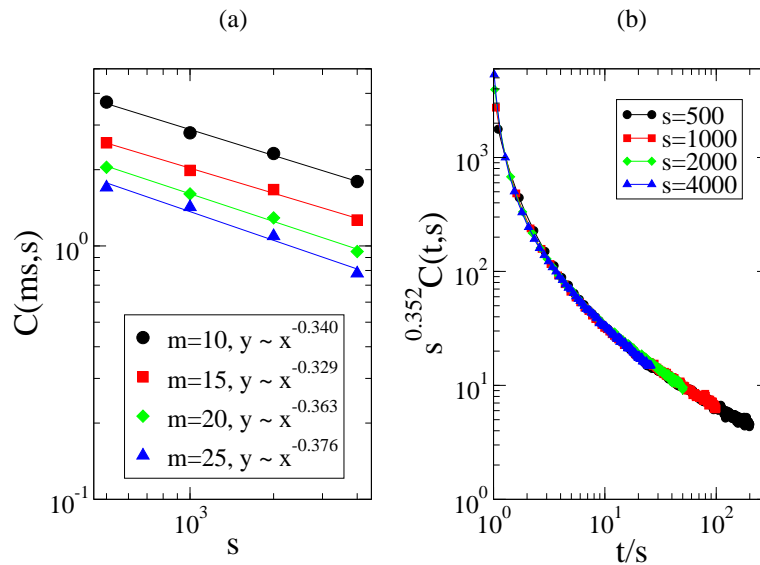


Figure 5.24: (a) Two-time density-density correlation as a function of s for interacting vortices with disorder at $T = 10$, $\lambda = 35b_0$, pinning strength 0.02, $dist = 12$, and different values of m . Regression analysis is done for $m=10, 15, 20$, and 25 and gives the slope of $-0.340, -0.329, -0.363$, and -0.376 . (b) The data nicely collapse for $b = 0.352$ at long times.

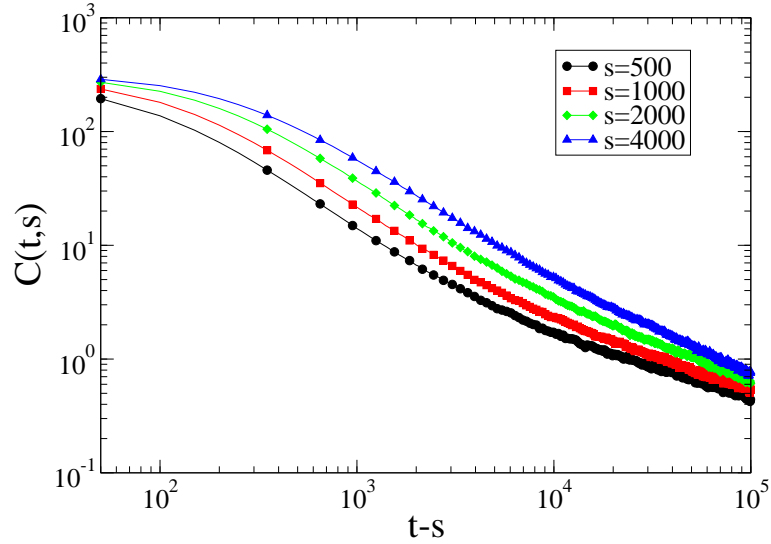


Figure 5.25: Two-time density-density correlation as a function of $t - s$ for interacting vortices with disorder at $T = 10$, $\lambda = 35b_0$, pinning strength 0.02, and $dist = 15$. The data for waiting times $s=500, 1000, 2000$, and 4000 MCS do not collapse on each other. The system with a larger waiting time decorrelates slower than the system with smaller waiting time. All curves shift up closer to the curve for large waiting time. The data comprises an average over 1450 defect distributions.

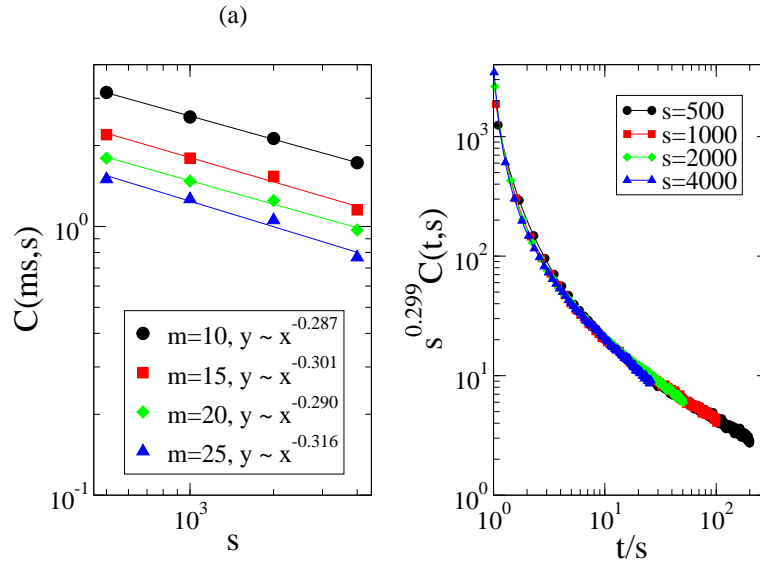


Figure 5.26: (a) Two-time density-density correlation as a function of s for interacting vortices with disorder at $T = 10$, $\lambda = 35b_0$, pinning strength 0.02, $dist = 15$, and different values of m . Regression analysis is done for $m=10, 15, 20$, and 25 and gives the slope of $-0.287, -0.301, -0.290$, and -0.316 . (b) The data collapse qualitatively for $b = 0.299$ at long times.

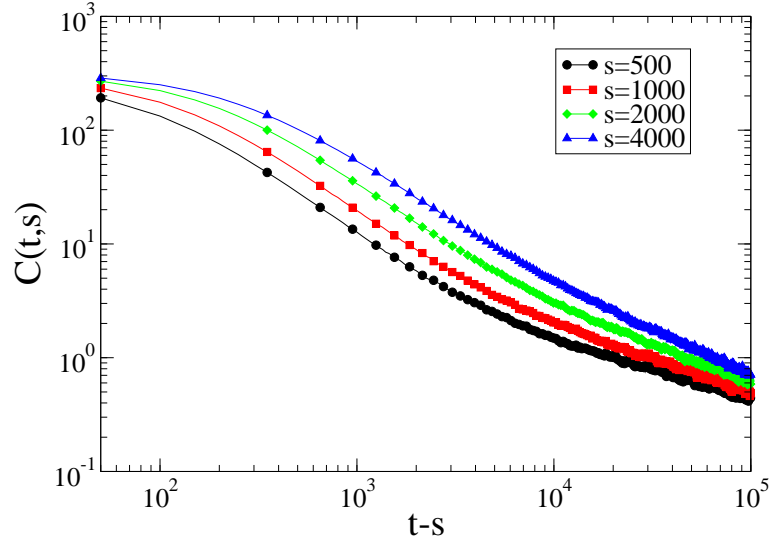


Figure 5.27: Two-time density-density correlation as a function of $t - s$ for interacting vortices with disorder at $T = 10$, $\lambda = 35b_0$, pinning strength 0.02, and $dist = 20$. The data for waiting times $s=500$, 1000, 2000, and 4000 MCS do not collapse on each other. The system with a larger waiting time decorrelates slower than the system with smaller waiting time. All curves shift up closer to the curve for large waiting time. The data comprises an average over 1080 defect distributions.

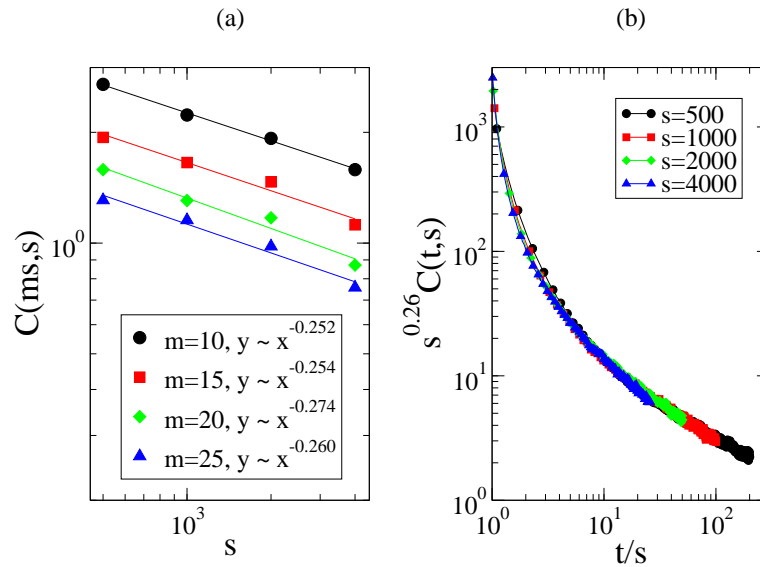


Figure 5.28: (a) Two-time density-density correlation as a function of s for interacting vortices with disorder at $T = 10$, $\lambda = 35b_0$, pinning strength 0.02, $dist = 20$, and different values of m . Regression analysis is done for $m=10$, 15, 20, and 25 and gives the slope of -0.252, -0.254, -0.274, and -0.260. (b) The data collapse qualitatively for $b = 0.26$ at long times.

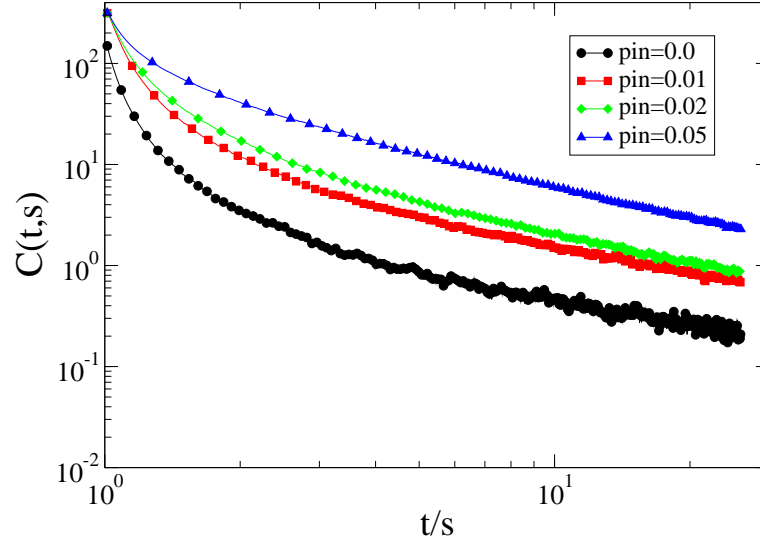


Figure 5.29: The autocorrelation for systems with $s=4000$, $\lambda_{ab} = 35b_0$, $T=10$, $dist = 9b_0$. Systems with a stronger pinning strength decay slower than systems with a weaker pinning strength. The systems with slower dynamics yield larger values of the exponents b and λ_c/z : $pin = 0.0$, $b = 0.2$, $\lambda_c/z = 0.396$; $pin = 0.01$, $b = 0.24$, $\lambda_c/z = 0.461$; $pin = 0.02$, $b = 0.452$, $\lambda_c/z = 0.676$; and $pin = 0.05$, $b = 0.751$, $\lambda_c/z = 0.899$.

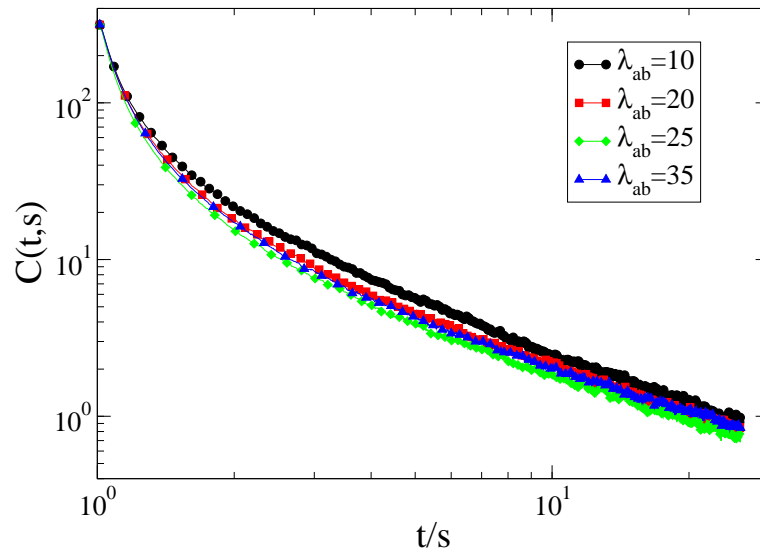


Figure 5.30: The autocorrelation for systems with $s=4000$, $pin = 0.02$, $T=10$, $dist = 9b_0$. Systems with a larger interaction range s decay faster than systems with a smaller interaction range. The systems with slower dynamics correspond to larger values of the exponents b and λ_c/z : $\lambda_{ab} = 10$, $b = 0.872$, $\lambda_c/z = 0.961$; $\lambda_{ab} = 20$, $b = 0.688$, $\lambda_c/z = 0.828$; $\lambda_{ab} = 25$, $b = 0.645$, $\lambda_c/z = 0.781$; and $\lambda_{ab} = 35$, $b = 0.452$, $\lambda_c/z = 0.676$.

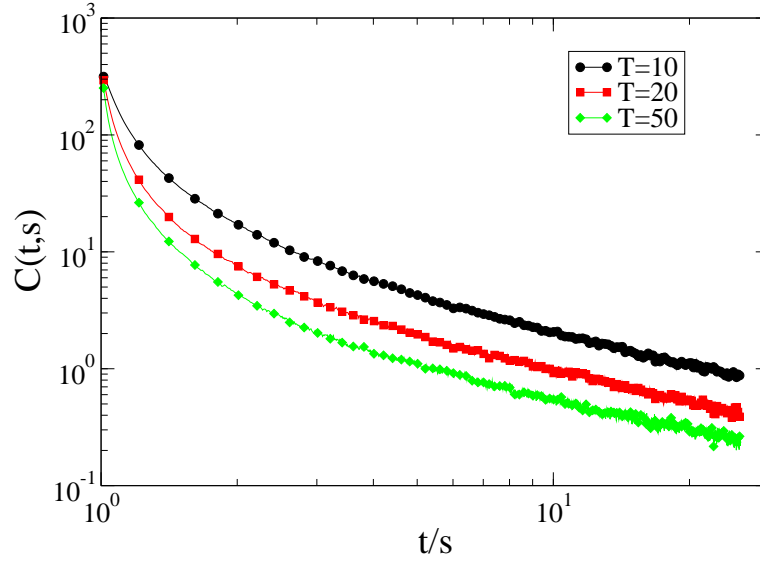


Figure 5.31: The autocorrelation for systems with $s=4000$, $pin = 0.02$, $\lambda_{ab} = 35b_0$, $dist = 9b_0$. Systems at a higher temperature s decay faster than systems at a lower temperature. The systems with slower dynamics correspond to larger values of the exponents b and λ_c/z : $T=10$, $\lambda_{ab} = 10$, $b = 0.452$, $\lambda_c/z = 0.676$; $T=20$, $b = 0.436$, $\lambda_c/z = 0.616$; and $T=50$, $b = 0.450$, $\lambda_c/z = 0.583$.

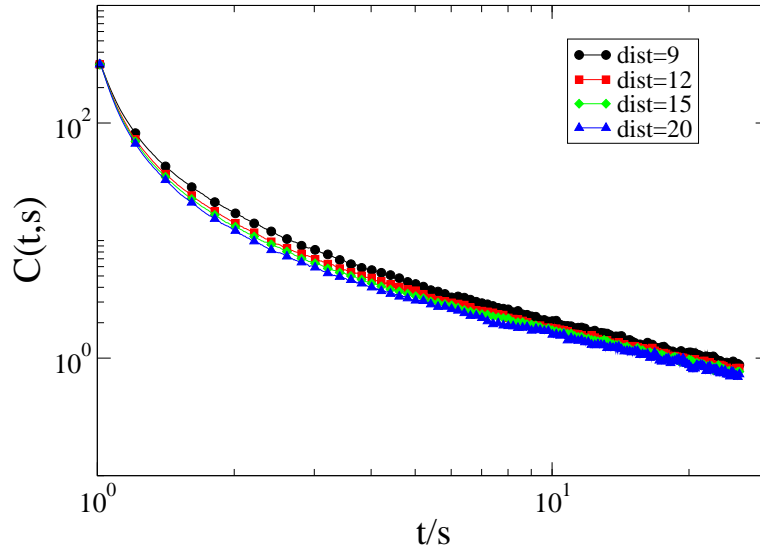


Figure 5.32: The autocorrelation for systems with $s=4000$, $pin = 0.02$, $T=10$, $\lambda_{ab} = 35b_0$. Systems with a higher defect density s decay slower than systems with a lower defect density. The systems with slower dynamics correspond to the larger values of the exponents b and λ_c/z : $dist = 9b_0$, $b = 0.452$, $\lambda_c/z = 0.676$; $dist = 12b_0$, $b = 0.352$, $\lambda_c/z = 0.564$; $dist = 15b_0$, $b = 0.299$, $\lambda_c/z = 0.555$; and $dist = 20b_0$, $b = 0.260$, $\lambda_c/z = 0.527$.

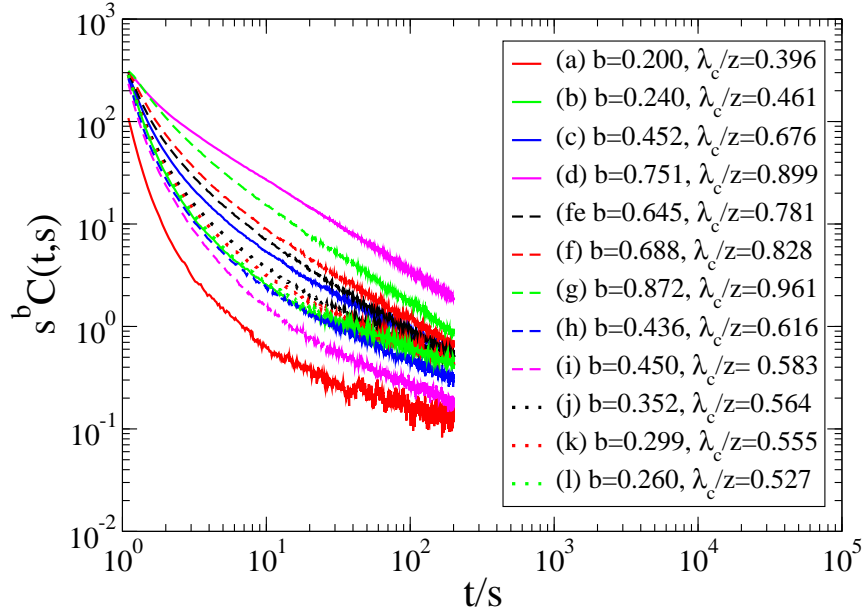


Figure 5.33: Behavior of the autocorrelation functions as a function of t/s for $s = 500$ MCS with parameters

- (a) $T=10$, $\lambda_{ab} = 35.0$, $dist = 9$, $pin=0.00$
- (b) $T=10$, $\lambda_{ab} = 35.0$, $dist = 9$, $pin=0.01$
- (c) $T=10$, $\lambda_{ab} = 35.0$, $dist = 9$, $pin=0.02$
- (d) $T=10$, $\lambda_{ab} = 35.0$, $dist = 9$, $pin=0.05$
- (e) $T=10$, $\lambda_{ab} = 25.0$, $dist = 9$, $pin=0.02$
- (f) $T=10$, $\lambda_{ab} = 20.0$, $dist = 9$, $pin=0.02$
- (g) $T=10$, $\lambda_{ab} = 10.0$, $dist = 9$, $pin=0.02$
- (h) $T=20$, $\lambda_{ab} = 35.0$, $dist = 9$, $pin=0.02$
- (i) $T=50$, $\lambda_{ab} = 35.0$, $dist = 9$, $pin=0.02$
- (j) $T=10$, $\lambda_{ab} = 35.0$, $dist = 12$, $pin=0.02$
- (k) $T=10$, $\lambda_{ab} = 35.0$, $dist = 15$, $pin=0.02$
- (l) $T=10$, $\lambda_{ab} = 35.0$, $dist = 20$, $pin=0.02$

where λ_{ab} is the penetration length which represents the interaction range, $dist$ is an average spacing between each defect. At long time $t/s \gg 1$, the scaling function $f_c(t/s)$ behaves like $(t/s)^{-\lambda_c/z}$. The dynamical scaling parameter λ_c/z is obtained by measuring a slope for $21 < t/s < 200$ for $s=500$.

Table 5.1: Dynamical scaling exponents b and λ_c/z for various systems.

T (K)	λ_{ab} (b_0)	pin (ϵ_0)	dist (b_0)	b	λ_c/z ($s = 500$)	λ_c/z ($s = 4000$)
10	35.0	0.0	9.00	0.20	0.396	0.759
10	35.0	0.01	9.00	0.24	0.461	0.843
10	35.0	0.02	9.00	0.452	0.676	0.920
10	35.0	0.05	9.00	0.751	0.899	1.004
10	25.0	0.02	9.00	0.645	0.781	0.961
10	20.0	0.02	9.00	0.688	0.828	1.005
10	10.0	0.02	9.00	0.872	0.961	1.051
20	35.0	0.02	9.00	0.436	0.616	0.900
50	35.0	0.02	9.00	0.450	0.583	0.845
10	35.0	0.02	12.00	0.352	0.564	0.881
10	35.0	0.02	15.00	0.299	0.555	0.893
10	35.0	0.02	20.00	0.260	0.527	0.848

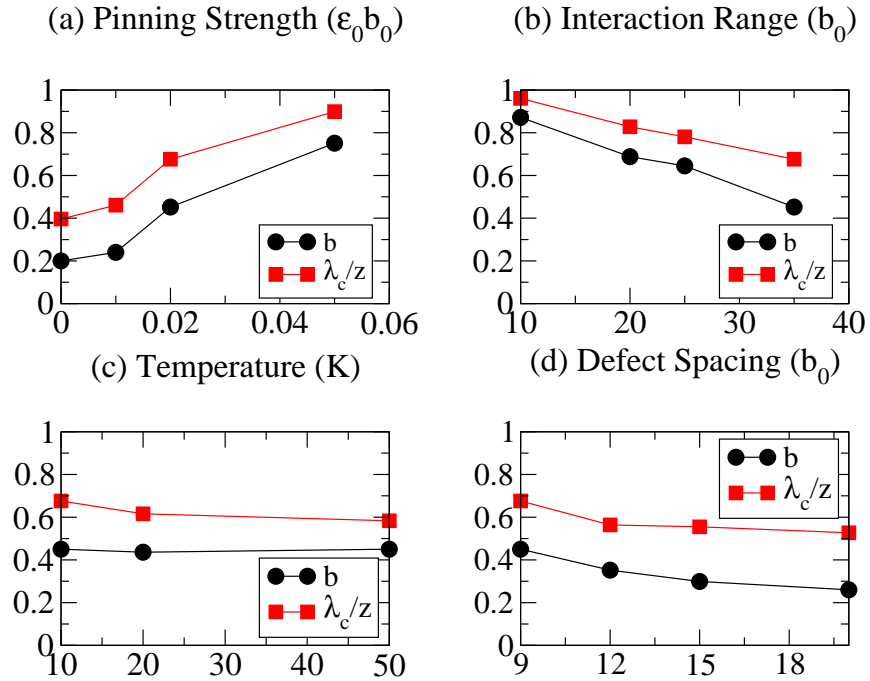


Figure 5.34: Dynamics exponents b (circle) and λ_c/z (square) as a function of (a) pinning strength (b) Penetration length which represents the interaction range (c) temperature and (d) an average spacing between each defect. The data in (b), (c), and (d) is for the system with the pinning strength of 0.02.

5.2.6 Conclusions

The aging phenomena in the system of interacting vortices occur at low temperature in the presence of long range interactions. They also depend on parameters such as the pinning strength, interaction range, and the defect density. The aging properties: slow power law relaxation, breaking of time-translation invariance, and the dynamical scaling are observed through the investigation of the density autocorrelation function. We characterized the aging properties by extracting the dynamical exponents b and λ_c/z from the autocorrelation function at long times $t/s \gg 1$. We found that the values of the exponent b and λ_c/z tend to behave in a similar manner. They tend to increase for the slower dynamics and decrease for the faster dynamics of the flux lines. Longer interaction range, higher temperature, lower defect density, and weaker pinning strength cause faster dynamics and hence lower the values of the scaling exponents. We found that the pinning strength and the interaction range strongly affect the values of the exponents. Our values of these exponents vary between 0 and 1 due to the different combinations of the pinning strength, interaction range, temperature, and defect density. Most of our findings for the exponent values b and λ_c/z do not agree with the results reported in Ref.[31] for the Langevin simulations at low temperature and for the gauge glass model at the critical temperature Ref.[116]. We did not observe aging in a system of a single flux line, but was observed in Ref.[31]. Our results are different from the behavior of b observed in [31], which reports smaller values of $b < 0.5$ for increasing pinning strength. We observed larger b for increasing pinning strength. The exponents b and λ_c/z We have summarized the values of exponent b and λ_c/z for various parameters in Table 5.1 and Fig. 5.34. The asymptotic behavior, which describes the exponent λ_c/z , for each case is shown in Fig.5.33. Our results are also different from the study of aging dynamics of the bond-disordered two-dimensional Ising model at $T < T_c$ [117]. It is found that the exponents b and λ_c/z decrease for decreasing temperature, which is in the opposite direction of our results. However, an increase of the width of the distribution of the coupling constant J_{ij} shows similar behavior. The aging is more relevant for a smaller width of the distribution, i.e., similar effect as we decrease the pinning strength.

Chapter 6

Discussion and Conclusion

In this work I have presented numerical investigations of two types of nonequilibrium systems. The first part concerned the nonequilibrium steady state of driven magnetic flux lines in type-II superconductors subject to the strong point or columnar disorder. The second part was a study of the nonequilibrium relaxation properties of the same system but with much weaker point defects. In particular, we have investigated the aging dynamics and its three crucial properties: slow power-law relaxation, breaking of the time-translation invariance, and the presence of dynamical scaling.

We have found that the dynamics of driven magnetic flux lines using a three-dimensional elastic line model displayed remarkable phenomena. Interesting features arise due to the competition between the elastic energy, pinning potential, repulsive vortex interaction, and the driving force. In the absence of the driving force and defect, we observed the Abrikosov vortex lattice as expected. The pinned vortex glass is observed in systems with strong point defect. The pinned Bose glass is observed in the presence of strong columnar defects. From our simulation results, the snapshots of these two systems from the top view look very similar, i.e., each flux line looks like a point-like particle locating inside the pinning center.

Flux lines behave differently if a small driving force is applied to the system. The effect due to different defect structures can be captured by the use of the velocity-force curves, which resemble I-V curves. We investigated this and found that systems with correlated defect such as columnar or splayed defect give higher critical depinning currents. The presence of strong point defects strongly promotes wandering of the flux lines, which results in a liquid-like vortex structure. If the magnitude of the driving force is small, we observed the pinned Bose glass. This marks a significant difference between results in two- and three-dimensional systems. This feature is also captured by measuring the radius of gyration and investigating snapshots of the system. By investigating the radius of gyration for various driving forces, we observed that the driving force changed the dynamics of moving flux lines from a regime dominated by a disorder at low driving forces to a regime dominated by the vortex interaction at high driving forces. This is clearly seen in the system with point defects for various driving forces and vortex densities. This behavior is not relevant in systems with weak pinning centers. In the low driving force

regime, we did not observe the double-kinks excitations as predicted in Ref.[34]. A small number of the half-loop excitations were found in the intermediate driving force regime.

At large driving force, we observed the liquid-like structure of moving flux lines in systems with strong point or columnar defects. We cannot distinguish structures of flux lines from the snapshots nor the diffraction plots. The diffraction plots of all our results show a single peak which corresponds to a disordered structure. The difference between these two systems at high driving force is captured by an investigation of the voltage noise. In systems with strong point defects just above the critical threshold, broadband noise is observed at all vortex densities and driving forces. Unlike in systems with columnar defects, narrow band peaks along the x- and y-direction were observed at intermediate driving forces before the saturation of the I-V curves occurred. Surprisingly, the frequencies of these peaks were not the predicted washboard frequencies, which is inversely proportional to the lattice constant and proportional to the average velocity of the moving flux lines. They are independent of the vortex density and velocity. We explained that the presence of these peaks were due to the wandering of vortex line elements inside the pinning centers. Near the critical depinning threshold, some of flux lines were moving while the rest were pinned inside the columnar defects. The repulsive interactions between these moving and pinned flux lines caused the pinned vortex line elements to shift inside the pinning centers. This happened in the direction away from the moving flux lines as the moving ones got closer to the pinned ones. The pinned vortex line elements moved at a constant rate until the moving flux lines pass them. If this process kept occurring over a long time, it gave rise to the periodicity of the velocity signal, and the narrow band peaks. Hence, one can identify or distinguish types of defects in the sample by means of the voltage noise, if the pinning strength is strong.

We next studied the nonequilibrium relaxation properties in the same system without the driving force. As mentioned at the beginning, all three required properties of the aging dynamics were found in our simulations if the long range interactions between vortex line elements were present. We observed the change in the property of the material over long time by the use of the two-time density-density autocorrelation function. In the presence of this long range interaction, the breaking of the time-translation invariance was clearly observed in all systems with various combinations of pinning strengths, interaction ranges, temperatures, and defect densities. The aging phenomena tend to disappear for systems with stronger pinning strengths, shorter interaction ranges, higher temperatures, and lower defect densities. These are important factors that we need for practical applications since we do not want the properties of materials to drastically change over time.

The behavior of these systems was carefully investigated by extracting the aging scaling exponents b and λ_c/z from the plots of the autocorrelation as a function of t/s . Simple aging was observed in our results for $t/s > 1$. It was found that values of these exponents behaved in a similar manner. They increase for increasing pinning strength, smaller interaction range, lower temperature, and higher defect density. In other words, higher values of b and λ_c/z indicate the presence of slower dynamics. Our results showed a different tendency than the existing literatures. We found that the values of b increased for decreasing pinning strength in Ref.[31], while the values of λ_c/z decreased for decreasing temperature in Ref.[117].

Further investigation of these systems will enable us to get a better understanding of the property of these materials. Many studies involve a modification of fluctuation-dissipation theorem. It would be interesting if we can test this in our system. In addition, it is not yet known if these aging effects would be present in systems with other defect configurations. Moreover, further investigations of the aging phenomena in a two-dimensional system would characterize the contribution of the defect configuration or vortex structure to the aging effects. The asymptotic behavior of our results still show different values of the exponent λ_c/z for different waiting times. It would be interesting to investigate whether these values coincide at larger simulation times or not. Another possibility is to investigate aging phenomena in a system of driven flux lines by measuring the velocity or density autocorrelation function. We have tried to investigate this and found the change of these quantities over time at very short time limit, small waiting time, higher vortex density, and very small driving force. Careful investigations such as a determination of the dynamical exponent b and λ_c/z are needed to confirm this result.

Bibliography

- [1] H. Kamerlingh-Onnes, Leiden Comm. **120b**, **122b**, **124c** (1911).
- [2] J. G. Bednorz and K. A. Müller, Z. Phys. B **64**, 189 (1986).
- [3] J. Nagamatsu, N. Nakagawa, T. Muranaka, Y. Zenitani, and J. Akimitsu, Nature **410**, 63 (2001).
- [4] Y. Kamihara, T. Watanabe, M. Hirano, and H. Hosono, J. Am. Chem. Soc. **130**, 3296 (2008).
- [5] T. Matsushita, *Flux pinning in Superconductors*, (Springer-Verlag, New York, 2007), p 37.
- [6] V. L. Ginzburg and E. A. Andryushin, *Superconductivity*, (World Science Publishing, Singapore, 2004).
- [7] G. Krabbes *et al.*, *High Temperature Superconductor Bulk Materials*, (Wiley, 2006).
- [8] G. B. Lubkin, *Power Applications of High- Temperature Superconductors*, Physics Today **49**, March (1996), p 48.
- [9] B. Batlogg, *Physical Properties of High-Tc Superconductors*, Physics Today **44**, June (1991), p 44.
- [10] S. T. Ruggiero and D. A. Rudman (eds.), *Superconducting Devices*, (Academic Press, San Diego, 1990).
- [11] D. D. Stark and W.G. Bradley, *Magnetic Resonance Imaging*, (C.V. Mosby Co., St. Louis, 1988).
- [12] C. A. Bolle, F. De La Cruz, P. L. Gammel, J. V. Waszczak, and D. J. Bishop, Phys. Rev. Lett. **71**, 4039 (1993).
- [13] A. M. Chang *et al.*, Appl. Phys. Lett. **61**, 1974 (1992).
- [14] P. L. Gammel *et al.*, Phys. Rev. Lett. **72**, 278 (1994).
- [15] H. F. Hess, C. A. Murray, and J. V. Waszczak, Phys. Rev. Lett. **69**, 2138 (1992).
- [16] K. Harada *et al.*, Phys. Rev. Lett. **71**, 3371 (1993).

- [17] U. Yaron *et al.*, Phys. Rev. Lett. **73**, 2748 (1994).
- [18] W. H. Kleiner, L. M. Roth, and S. H. Autler, Phys. Rev. **133**, A1226 (1964).
- [19] T. Giamarchi and P. Le Doussal, Phys. Rev. B **52**, 1242 (1995).
- [20] P. Le Doussal and T. Giamarchi, Phys. Rev. B **55**, 6577 (1997).
- [21] T. Giamarchi and P. Le Doussal, Phys. Rev. Lett. **76**, 3408 (1996).
- [22] M. P. A. Fisher, Phys. Rev. Lett. **62**, 1415 (1989).
- [23] D. S. Fisher, M. P. A. Fisher, and D. A. Huse, Phys. Rev. B **43**, 130 (1990).
- [24] M. P. A. Fisher, P. B. Weichman, G. Grinstein, and D. S. Fisher, Phys. Rev. B **40**, 546 (1989).
- [25] P. Le Doussal and T. Giamarchi, Phys. Rev. B **57**, 11356 (1998).
- [26] L. F. Cugliandolo, *Dynamics of glassy systems*, Lecture notes in Slow Relaxation and non equilibrium dynamics in condensed matter, Les Houches Session 77 July 2002, J. L. Barrat, J. Dalibard, J. Kurchan, M. V. Feigel'man eds. cond-mat/0210312.
- [27] D. P. Landau and K. Binder, *A Guide to Monte Carlo simulations in Statistical Physics*, (Cambridge University Press, New York, 2000).
- [28] K. Binder and D. W. Heermann, *Monte Carlo Simulations in Statistical Physics*, (Springer-Verlag, New York, 1997), p 29.
- [29] R. Exartier and L. F. Cugliandolo, Phys. Rev. B **66**, 012517 (2002).
- [30] S. Bustingorry, L. F. Cugliandolo, and D. Domínguez, Phys. Rev. Lett. **96**, 027001 (2006).
- [31] S. Bustingorry, L. F. Cugliandolo, and D. Domínguez, Phys. Rev. B **75**, 024506 (2007).
- [32] F. Portier *et al.*, Phys. Rev. B **66**, 140511(R) (2002).
- [33] T. J. Bullard, J. Das, G. L. Daquila, and U. C. Täuber, Eur. Phys. J. B **65**, 469 (2008).
- [34] D. R. Nelson and V. M. Vinokur, Phys. Rev. B **48**, 13060 (1993).
- [35] M. Tinkham, *Introduction to Superconductivity*, (McGraw-Hill, New York, 1975).
- [36] A. C. Rose-Innes and E. H. Rhoderick, *Introduction to Superconductivity*, (Pergamon Press, New York, 1969).
- [37] J. Bardeen, L. N. Cooper, and J. R. Schrieffer, Phys. Rev. **108**, 1175 (1957).
- [38] V. L. Ginzburg and L. D. Landau, Zh. Eksperim. i Teor. Fiz. **20**, 1064 (1950).

- [39] A. A. Abrikosov, Zh. Eksperim. i Teor. Fiz **32**, 1442 (1957) [Sov. Phys.-JETP 5, 1174 (1957)].
- [40] U. Essmann and H. Träuble, Phys. Lett. **42A**, 526 (1967).
- [41] U. C. Täuber and D. R. Nelson, Phys. Rep. **289**, 157 (1997).
- [42] D. R. Nelson and H. S. Seung, Phys. Rev. B **39**, 9153 (1989).
- [43] G. Blatter, M. V. Feigelman, V. B. Geshkenbein, A. I. Larkin, and V. M. Vinokur, Rev. Mod. Phys. **66**, 1125 (1994).
- [44] Y. B. Kim, C. F. Hempstead, and A. R. Strnad, Phys. Rev. **131**, 2486 (1963).
- [45] Y. B. Kim, C. F. Hempstead, and A. R. Strnad, Phys. Rev. **139**, A1163-A1172 (1965).
- [46] D. R. Nelson, Phys. Rev. Lett. **60**, 1973 (1988).
- [47] L. Civale *et al.*, Phys. Rev. Lett. **67**, 648 (1991).
- [48] M. Konczykowski *et al.*, Phys. Rev. B **44**, 7167 (1991).
- [49] F. M. Sauerzopf, H. P. Wiesinger, H. W. Weber, G. W. Crabtree, and J. Z. Liu, Physica C **162-164**, 751 (1989).
- [50] W. E. Lawrence and S. Doniach, *Proc. 12th Int. Conf. Low Temp. Phys.*, ed. E. Kanda (Kyoto, 1970; Keigaku, Tokyo, 1971), p 361.
- [51] D. R. Nelson and V. M. Vinokur, Phys. Rev. Lett. **68**, 2398 (1992).
- [52] S. Tyagi and Y. Y. Goldschmidt, Phys. Rev. B **67**, 214501 (2003).
- [53] R. H. Koch, V. Foglietti, W. J. Gallagher, G. Koren, A. Gupta, and M. P. A. Fisher, Phys. Rev. Lett. **63**, 1151 (1989).
- [54] P. S. Mukherjee, A. Simon, and A. D. Damodaran, J. Mater. Sci. Lett. **8**, 981 (1989).
- [55] C. Reichhardt, C. J. Olson, and F. Nori, Phys. Rev. B **58**, 6534 (1998).
- [56] H. J. Jensen, A. Brass, and A. J. Berlinsky, Phys. Rev. Lett. **60**, 1676 (1988).
- [57] H. J. Jensen, A. Brass, Y Brechet, and A. J. Berlinsky, Phys. Rev. B **38**, 9235 (1988).
- [58] C. J. Olson, C. Reichhardt, and F. Nori, Phys. Rev. B **57**, 7937 (1997).
- [59] C. Reichhardt and G. T. Zimányi, Phys. Rev. B **61**, 14354 (1999).
- [60] C. Reichhardt, C. J. Olson, R. T. Scalettar, and G. T. Zimányi, Phys. Rev. B **64**, 144509 (2001).
- [61] R. H. Koch, V. Foglietti, W. J. Gallagher, G. Koren, A. Gupta, and M. P. A. Fisher, Phys. Rev. Lett. **63**, 1511 (1989).

- [62] R. H. Koch, V. Foglietti, and M. P. A. Fisher, Phys. Rev. Lett. **64**, 2586 (1990).
- [63] Q. H. Chen, Euro. Phys. Lett. **84**, 64001 (2008).
- [64] A. B. Pippard, Philos. Mag. **19**, 217 (1967).
- [65] A. I. Larkin and Yu. N. Ovchinnikov, J. Low Temp. Phys. **34**, 409 (1979).
- [66] W. Henderson, E. Y. Andrei, M. J. Higgins, and S. Bhattacharya, Phys. Rev. Lett. **77**, 2077 (1996).
- [67] A. E. Koshelev and V. M. Vinokur, Phys. Rev. Lett. **73**, 3580 (1994).
- [68] K. Harada *et al.*, Science **274**, 1167 (1996).
- [69] C. Reichhardt, C. J. Olson, and F. Nori, Phys. Rev. Lett. **78**, 2648 (1997).
- [70] C. J. Olson, C. Reichhardt, and S. Bhattacharya, Phys. Rev. B **64**, 024518 (2001).
- [71] C. Reichhardt, C. J. Olson, J. Groth, S. Field, and F. Nori, Phys. Rev. B **53**, R8898 (1996).
- [72] R. K. P. Zia and B. Schmittmann, J. Phys. A: Math. Gen. **39**, L407L413 (2006).
- [73] M. D. Ediger, C. A. Angell, and S. R. Nagel; J. Phys. Chem. **100**, 13200 (1996).
- [74] A. J. Kovacs, Fortschr. Hochpolym. Forsch. **3**, 394 (1964).
- [75] E. Jenckel, Z. Elektrochem. **45**, 202 (1939).
- [76] L. C. E. Struik, Rheol. Acta **5**, 303 (1966).
- [77] L. C. E. Struik, *Physical Aging in Amorphous Polymers and Other Materials* (Elsevier, Amsterdam, 1978).
- [78] A. J. Bray, Adv. Phys. **43**, 357 (1994).
- [79] M. Henkel, M. Pleimling, and R. Sanctuary, *Introduction*, Lect. Notes Phys. **716**, p 1 (2007).
- [80] L. Berthier, P. C. W. Holdsworth, and M. Sellitto, J. Phys. A **34**, 1805 (2001).
- [81] M. Henkel and M. Pleimling, Europhys. Lett. **69**, 524 (2005).
- [82] D. S. Fisher and D. A. Huse, Phys. Rev. B **38**, 373 (1988).
- [83] A. Picone and M. Henkel, J. Phys. A **35**, 5575 (2002).
- [84] X. Du, G. Li, E. Y. Andrei, M. Greenblatt, and P. Shuk, Nature Physics **3**, 111 (2007).
- [85] A. Vestergren, M. Wallin, Phys. Rev. B **69**, 144522 (2004).

- [86] A. T. Fiory, Phys. Rev. Lett. **27**, 501 (1971).
- [87] J. M. Harris, N. P. Ong, R. Gagnon, and L. Taillefer, Phys. Rev. Lett. **74**, 3684 (1995).
- [88] A. M. Troyanovski, J. Aarts, and P. H. Kes, Nature (London) **399**, 665 (1999).
- [89] Y. Togawa, R. Abiru, K. Iwaya, H. Kitano, and A. Maeda, Phys. Rev. Lett. **85**, 3716 (2000).
- [90] C. J. Olson, C. Reichhardt, and F. Nori, Phys. Rev. Lett. **81**, 3757 (1998).
- [91] A. B. Kolton, D. Dominguez, and N. Gronbech-Jensen, Phys. Rev. B **65**, 184508 (2002).
- [92] H. Fangohr, S. J. Cox, and P. A. J. de Groot, Phys. Rev. B **64**, 064505 (2001).
- [93] Q. Chen and X. Hu, Phys. Rev. Lett. **90**, 117005 (2003).
- [94] A. C. Marley *et al.*, Phys. Rev. Lett. **74**, 3029 (1995).
- [95] A. Pautrat, J. Scola, Phys. Rev. B **79**, 024507 (2009).
- [96] T. J. Bullard, J. Das, and U. C. Täuber, Trends in Superconductivity Research, p. 63-72 (2004).
- [97] M. C. Hellerqvist, D. Ephron, W. R. White, M. R. Beasley, and A. Kapitulnik, Phys. Rev. Lett. **76**, 4022 (1996).
- [98] P. L. Gammel, L. F. Schneemeyer, and D. J. Bishop, Phys. Rev. Lett. **66**, 953 (1991).
- [99] S. Bhattacharya and M. J. Higgins, Phys. Rev. Lett. **70**, 2620 (1993); Phys. Rev. B **49**, 10005 (1994).
- [100] P. W. Anderson, Phys. Rev. Lett. **9**, 309 (1962).
- [101] Y. Ando, N. Motohira, K. Kitazawa, J. I. Takeya, and S. Akita, Phys. Rev. Lett. **67**, 2737 (1991).
- [102] Q. Li, H. J. Wiesmann, M. Suenaga, L. Motowidlow, and P. Haldar, Phys. Rev. B **50**, 4256 (1994).
- [103] T. J. Bullard, Ph. D. Thesis, Virginia Polytechnic Institute and State University (2005).
- [104] T. Hwa, D. R. Nelson, and V. M. Vinokur, Phys. Rev. B **48**, 1167 (1993).
- [105] U. C. Täuber, H. Dai, D. R. Nelson, and C. M. Lieber, Phys. Rev. Lett. **74**, 5132 (1995).
- [106] C. T. Rogers, K. E. Myers, J. N. Eckstein, and I. Bozovic, Phys. Rev. Lett. **69**, 160 (1992).

- [107] Ö. Festin, P. Svedlindh, B. J. Kim, P. Minnhagen, R. Chakalov, and Z. Ivanov, Phys. Rev. Lett. **83**, 5567 (1999).
- [108] D. Ertas and M. Kardar, Phys. Rev. Lett. **73**, 1703 (1994).
- [109] J. Das, T. J. Bullard, and U. C. Täuber, Physica A **318**, 48 (2003).
- [110] E. Vincent, in [79], and references therein.
- [111] C. Godrèche and J.-M. Luck, J. Phys.: Condens. Matter **14**, 1589 (2002).
- [112] J. L. Barrat and W. Kob, Europhys. Lett. **46**, 637 (1999).
- [113] A. M. Puertas, M. Fuchs, and M. E. Cates, Phys. Rev. E **75**, 031401 (2007).
- [114] B. Bakó, I. Groma, G. Györgyi, and G.T. Zimányi, Phys. Rev. Lett. **98**, 075701 (2007).
- [115] M. Henkel, M. Pleimling, cond-mat/0703466.
- [116] F. Romá and D. Domínguez, Phys. Rev. B **78**, 184431 (2008).
- [117] M. Henkel and M. Pleimling, Europhys. Lett. **76**, 561 (2006).
- [118] J. M. Lynch, G. C. Cianci, and E. R. Weeks, Phys. Rev. E **78**, 031410 (2008).